Ph.D Thesis

Topological phases of 3D superlattices and 2D materials : theoretical modelling

By

RAJIBUL ISLAM

International Centre for Interfacing Magnetism and Superconductivity with Topological Matter-(MagTop)
in
Division ON-6 of Institute of Physics, Polish Academy of Sciences (IF PAN)

JANUARY 13, 2023

ABSTRACT IN ENGLISH

The exotic physics of topological phases like topological insulators (TIs), topological crystalline insulators (TCIs), quantum spin Hall insulators (QSHIs), Dirac semimetals (DMs), Weyl semimetals (WSMs), and nodal-line semimetals (NDLSMs) have been the subject of extensive theoretical and experimental work over the past few decades. In most cases, symmetries play an important role in protecting the topological phases. One of the simplest and most fundamental of these is the time-reversal symmetry (TRS). The TRS symmetry is broken by inducing magnetism through magnetic doping and creating magnetic heterostructure. Topological materials lacking TRS may exhibit magnetic topological phases such as antiferromagnetic topological insulators, magnetic Weyl, Dirac, and nodal-line semimetals, and quantum anomalous Hall phases. However, it is challenging to find realistic materials that can support exotic topological states. The advancement of nanoscience and nanotechnology, as well as the commercialization of applications like quantum spintronics and quantum communication, demands the discovery of new candidate materials exhibiting exotic behaviors.

In search of new materials as candidates for exotic quantum phenomena, this thesis primarily focus on two different classes of materials-

(i) The topological phases in HgTe-based 3D superlattices: We use ab initio simulations to study the evolution of topological phases as a function of hydrostatic pressure and uniaxial strain in two types of superlattices: HgTe/CdTe and HgTe/HgSe, in our search for materials with three-dimensional flat band dispersions. Isoenergetic nodal lines have been discovered in short-period HgTe/CdTe superlattices, which could host strain-induced three-dimensional flat bands at the Fermi level without doping. There are a wide variety of topological phases in the phase diagram of short-period HgTe/HgSe superlattices. An perfect Weyl semimetal phase is realized in an unstrained HgTe/HgSe superlattice. The superlattice transforms into a small-gap topological insulator with many band inversions when subjected to compressive uniaxial strain.

(ii) The quantum phase of MSi_2Z_4, a new synthetic 2D material (M = Mo, W, and Z = N, P, As): Ultra-thin films of the 2D synthetic material MSi_2Z_4 (M = Mo or W and Z = N, P, and As) are studied for their spin-dependent electronic properties and topological exotic phases for quantum device applications using first-principles modeling. In the 2H phase, while MSi_2Z_4 (M= Mo,W and Z= N or As) monolayers are stacked to form bilayers or bulk, the electronic properties of the resulting material vary depending on its thickness. As a result of spin-orbit coupling (SOC), we observe that the monolayers are semiconductor having a 100 % spin polarization, with the spins locked in opposite directions along an out-of-plane direction at K and K′, leading to spin-valley coupling. The spin polarization in the bilayer is zero due to the presence of the inversion symmetry. We show that, like in MoS2 and WS2 bilayers, an out-of-plane electric field can flip the bilayers' spin polarization. Moreover, we predict a family of 1T′ structure MSi_2Z_4 (M = Mo or W and Z = P or As) materials with a switchable large bandgap QSH insulator. A band inversion between the metal (Mo/W) d and p states of P/As is introduced by a distortion in the 2H phase, leading to the

i

creation of spinless Dirac cone states absent of spin-orbit interaction. By including the spin-orbit coupling, a 204 meV hybridization gap opens up at band crossing points, yielding spin-polarized conducting edge states with spin Hall conductivity. Through the application of a vertical electric field, we demonstrate that the inverted band gap can be manipulated, resulting in a topological phase transition from QSH to a trivial insulator with Rashba-like edge states. For the creation of various transistors, the electric field dependent features of 2H and 1T$'$ structures could turn out to be extremely useful.

This thesis is a collection of publications related to the topological phase of HgTe-based 3D superlattices and 2D materials MSi_2Z_4 (M= Mo,W and Z= N,P,As).

Egzotyczna fizyka faz topologicznych, takich jak izolatory topologiczne (TI), topologiczne izolatory krystaliczne (TCI), kwantowe spinowe izolatory Halla (QSHI), semimetale Diraca (DM) , semimetale Weyla (WSM) i semimetale typu „nodal line" (NDLSM) stała się ostatnimi czasy przedmiotem szeroko zakrojonych badań teoretycznych i eksperymentalnych. W większości przypadków symetrie odgrywają ważną rolę w ochronie faz topologicznych, a jedną z najprostszych i najbardziej fundamentalnych z nich jest symetria względem odwrócenia czasu (TRS). Symetria TRS jest łamana przez indukowanie magnetyzmu poprzez domieszkowanie magnetyczne i tworzenie heterostruktury magnetycznej. Materiały topologiczne pozbawione TRS mogą wykazywać magnetyczne fazy topologiczne, takie jak antyferromagnetyczne izolatory topologiczne, magnetyczne semimetale Weyla, Diraca i "nodal line" oraz kwantowe anomalne fazy Halla. Trudno jest jednak znaleźć rzeczywiste materiały, w których mogą realizować się egzotyczne stany topologiczne. Postęp nanonauki i nanotechnologii, a także komercjalizacja zastosowań, takich jak spintronika kwantowa i komunikacja kwantowa, wymaga prac nad odkryciem nowych materiałów wykazujących egzotyczne zachowania.

W poszukiwaniu nowych kandydatów, w których mogą zachodzić egzotyczne zjawiska kwantowe, niniejsza praca koncentruje się przede wszystkim na dwóch różnych klasach materiałów:

(i) Fazy topologiczne w supersieciach 3D opartych na HgTe : Używamy symulacji ab initio do badania ewolucji faz topologicznych w zależności od ciśnienia hydrostatycznego i odkształcenia jednoosiowego w dwóch typach supersieci : HgTe / CdTe i HgTe / HgSe, poszukując materiałów z trójwymiarową płaską dyspersją pasmową. W krótkookresowych HgTe / CdTe odkryto izoenergetyczne linie węzłowe supersieci , które mogą zawierać trójwymiarowe płaskie pasma wywołane odkształceniem na poziomie Fermiego bez domieszkowania. Na diagramie fazowym krótkookresowych HgTe / HgSe występuje wiele różnych faz topologicznych. Idealna faza semimetalu Weyla jest realizowana w nienaprężonej supersieci HgTe / HgSe, która przekształca się w izolator topologiczny z wąską szczeliną i wieloma inwersjami pasm, gdy jest poddawana ściskającemu odkształceniu jednoosiowemu .

(ii) Faza kwantowa MSi2Z4, nowego syntetycznego materiału 2D (M = Mo, W i Z = N , P , As) : Ultracienkie warstwy syntetycznego materiału 2D MSi_2Z_4 (M = Mo albo W, Z = N, P albo As) są badane przy użyciu modelowania z pierwszych zasad pod kątem zastosowań w urządzeniach kwantowych ich egzotycznych faz topologicznych z właściwościami elektronowymi zależnymi od spinu. Gdy monowarstwy MSi_2Z_4 (M= Mo , W i Z = N albo As) są układane w stosy tworzą dwuwarstwy lub układ objętościowy, i w związku z tym właściwości elektronowe otrzymanego materiału zależą od jego grubości. W wyniku sprzężenia spin-orbita (SOC) obserwujemy, że monowarstwy są półprzewodnikami o 100% polaryzacji spinowej, ze spinami zablokowanymi w przeciwnych kierunkach wzdłuż kierunku poza płaszczyzną w K i K′ , co prowadzi do dolinowo-spinowego sprzęgnięcia. Polaryzacja spinowa w dwuwarstwie wynosi zero ze względu na obecność symetrii inwersji. Pokazujemy, że podobnie jak w przypadku dwuwarstw MoS_2 i WS_2 pole elek-

tryczne poza płaszczyzną może odwrócić polaryzację spinowa dwuwarstw. Ponadto przewidujemy istnienie rodziny struktur 1T' MSi_2Z_4 (M = Mo lub W i Z = P albo As) z przełączalnym izolatorem QSH o dużej przerwie wzbronionej. Inwersja pasma między metalicznymi (Mo/W) stanami d i p P/As jest wprowadzana przez zniekształcenie fazy 2H, co prowadzi do powstania bezwirowych stanów stożka Diraca bez interakcji spin-orbita. Uwzględniając sprzężenie spin-orbita, w punktach przecięcia pasm otwiera się przerwa hybrydyzacyjna 204 meV, dając spolaryzowane spinowo przewodzące stany krawędziowe ze spinowym przewodnictwem Halla. Poprzez zastosowanie pionowego pola elektrycznego wykazaliśmy, że odwróconym pasmem wzbronionym można manipulować, co skutkuje topologicznym przejściem fazowym z QSH do trywialnego izolatora ze stanami krawędzi podobnymi do Rashby. Własności 2H i struktur 1T' zależne od pola elektrycznego mogą okazać się niezwykle przydatne Do tworzenia różnych tranzystorów,.

Niniejsza praca jest zbiorem publikacji związanych z fazą topologiczną supersieci 3D opartych na HgTe i materiałach 2D MSi2 Z4 (M = Mo, W i Z = N, P, As).

I certify that the work presented in this dissertation is my individual research and has not been submitted for consideration in any other academic awards. It has been completed in accordance with the requirements of the Institute of Physics, Polish Academy of Science (IFPAN), as well as the Code of Practice for Research Degree Programs. It is the candidate's own work, unless a particular reference in the text indicates otherwise. Collaborative efforts are properly credited as such. The work was done under the guidance of Dr. hab. Carmine Autieri, at MagTop, IFPAN Warsaw, Poland.

SIGNED: .... DATE: ....

This thesis is based on the three papers mentioned below where I do contribute as 1st author which is highlighted by bold text.

1. **Rajibul Islam**, Barun Ghosh, Giuseppe Cuono, Alexander Lau, Wojciech Brzez-icki, Arun Bansil, Amit Agarwal, Bahadur Singh, Tomasz Dietl, Carmine Autieri *"Topological states in superlattices of HgTe-class materials for engineering three-dimensional flat bands"* Phys.Rev. Research 4, 023114 (2022)

2. **Rajibul Islam**, Barun Ghosh, Carmine Autieri, Sugata Chowdhury, Arun Bansil, Amit Agarwal, Bahadur Singh *"Tunable spin polarization and electronic structure of bottom-up synthesized $MoSi_2N_4$ materials"* Phys. Rev. B 104, L201112 (2021)

3. **Rajibul Islam**, Rahul Verma, Barun Ghosh, Arun Bansil, Carmine Autieri,and Bahadur Singh *"Switchable large-gap quantum spin Hall state in two-dimensional MSi_2Z_4 class of materials"* Physical Review B 106 (24), 245149

Although the papers mention bellow are not included in this comprehensive summary of the thesis.

1. **Rajibul Islam**, Sougata Mardanya, Alexander Lau, Giuseppe Cuono, Tay-Rong Chang, Carlo M. Canali, Bahadur Singh, Tomasz Dietl and Carmine Autieri *"Axion insulating phase in superlattices without inversion symmetry"* (arXiv:2211.05152)

2. **Rajibul Islam**, Ghulam Hussain, Rahul Verma, Mohammad Sadegh Talezadehlari, Zahir Muhammad, Bahadur Singh, Carmine Autieri *"Fast electrically switchable large gap quantum spin Hall states in MGe_2Z_4"* (arXiv:2211.06443)

3. Carmine Autieri, Cezary Sliwa, **Rajibul Islam**, and Tomasz Dietl, *"Momentum-resolved spin splitting in Mn-doped trivial CdTe and topological HgTe semiconductors"*. Phys. Rev. B 103, 115209 (2021)

4. N. Pournaghavi, M. F. Islam, **Rajibul Islam**, Carmine Autieri , Tomasz Dietl , and C. M. Canali, *"Realization of the Chern insulator and Axion insulator phases in antiferromagnetic MnTe-Bi2(Se, Te)3-MnTe heterostructures"*. Phys. Rev.B 103, 195308 (2021)

5. Sukanta Kumar Jena, **Rajibul Islam**, Ewelina Milińska, Marcin Jakubowski, Roman Minikayev, Sabina Lewińska, Artem Lynnyk, Aleksiej Pietruczik, Paweł Aleszkiewicz, *"Interfacial Dzyaloshinskii-Moriya interaction in epitaxial $W/Co/Pt$ structures"*. Nanoscale, 13, 7685-7693 (2021)

6. Giuseppe Cuono, Filomena Forte, Mario Cuoco, **Rajibul Islam**, Jianlin Luo, Canio Noce, Carmine Autieri. *"Multiple band-crossings and Fermi surface topology: role of double nonsymmorphic symmetries in MnP-type crystal structures"*. Phys. Rev. Materials 3, 095004 (2019)

7. Zahir Muhammad, **Rajibul Islam**, Yan Wang, Carmine Autieri, Ziyu Lv, Bahadur Singh, Pierre Vallobra, Yue Zhang, Ling Zhu, Weisheng Zhao *"Laser Irradiation Effect on the p-GaSe/n-HfS$_2$ PN-Heterojunction for High-Performance Phototransistors"*. ACS Applied Materials Interfaces 14 (31), 35927-35939

8. Nguyen Minh Nguyen, Giuseppe Cuono, **Rajibul Islam**, Carmine Autieri, Timo Hyart, Wojciech Brzezicki *"Unprotected edge modes in quantum spin Hall insulator candidate materials"*. (arXiv:2209.06912)

9. Md Shahin Alam, Amar Fakhredine, Mujeeb Ahmed, PK Tanwar, Hung-Yu Yang, Fazel Tafti, Giuseppe Cuono, **Rajibul Islam**, Bahadur Singh, Artem Lyn-

nyk, Carmine Autieri, Marcin Matusiak *"Sign change of the anomalous Hall effect and the anomalous Nernst effect in Weyl semimetal CeAlSi"*. (arXiv:2210.09764)

10. Ghulam Hussain, Giuseppe Cuono, **Rajibul Islam**, Artur Trajnerowicz, Jarosław Jureńczyk, Carmine Autieri, Tomasz Dietl *"Electronic and optical properties of $InAs/InAs_{0.625}Sb_{0.375}$ superlattices and their application for far-infrared detectors"*. Journal of Physics D: Applied Physics 55 (49), 495301

11. Zahir Muhammad, Jan Szpakowski, Ghulam Abbas, Lin Zu,**Rajibul Islam**, Yan Wang, Faiz Wali, Arka Karmakar, Maciej R. Molas, Yue Zhang, Ling Zhu,Weisheng Zhao, Han Zhang *"Anisotropic phonon and magnon vibration and gate-tunable optoelectronic properties of nickel thiophosphite"*. Accepted in 2D Materials

12. **R Islam**, G Cuono, NM Nguyen, C Noce, C Autieri *"Topological Transition in $Pb_{1x}Sn_xSe$ using Meta-GGA Exchange-Correlation Functional"*. Acta Physica Polonica A 139 (2), 169-169

1

INTRODUCTION

The Landau theory of phase transitions in condensed matter physics describes the transition from one symmetric phase at high temperature to a less symmetric or symmetry broken phase at low temperature in terms of a change in the local order parameters of the system[1–3]. Most intriguingly, the free energy can expand in the order parameter close to the phase transition, the order of the transition depends on whether or not the expansion coefficient vanishes at the second, third, or higher order. The symmetries of the different phases determine the exact form of the order parameter and the various terms in the free energy. Despite the fact that the absolute value of the order parameter is not always known, Landau theory is the most successful in explaining phase transition in a broad class of systems. Nonetheless, experimental observation can be explained by this theory even without the knowledge of macroscopic details. This formalism allows for the description of two very different systems using the same physical language. However, this theory has its own shortcomings, it cannot account for experimental observations involving non-local order parameters, such as those involving the quantum Hall effect (QHE)[4].

In the last decade, several experimental observations have been changed the comprehension of phases and phase transition of the materials. In the 1980, the observation of the quantum Hall effect in the two dimensional (2D) materials under an applied electric field is the paradigm of such experimental observations[5]. The Hall conductivity is quantized to an integer multiple of $\frac{e^2}{h}$, and the of this integer depends on the strength of applied magnetic field for a given density of state. The states with different quantized value don't breaks any symmetry, so the landau theory can't distinguish the phase. It has been shown the QHE phase poses non local order parameter, which can describe the phases associated with quantization of the conductivity with magnetic filed. The various quantum phases (or states) can be described with a non-local order-parameter known as topological invariant which is different in different quantum states. In 1982 the first

insight toward topological invariant is given by Thouless, Kohmoto, Nightingale and Nijs, they shows different quantum states (or phases) can be distinguish with the TKNN invariant[6]. This invariant can be comprehended in terms of the Berry phase associated with the Bloch wave functions (uk), it could be express as-

$$C = \frac{1}{2\pi} \int_{BZ} \left[\nabla \times \vec{A}(k_x, k_y) \right] \tag{1.1}$$

where,

$$\vec{A} = -i \langle u(k) | \nabla u(k) \rangle \tag{1.2}$$

The quantum Hall conductivity in the transverse direction can be expressed as-

$$\sigma_{xy} = C \frac{e^2}{h} \tag{1.3}$$

The QHE is the first insight of the topological effect in condensed matter physics. In 1988, Haldane shows QHE phase of the materials could be achieved by the lattice geometry effect in absence of magnetic field. This phenomenon is described in the seminal paper without the Landau picture, by adding complex 2nd nearest neighbor hooping [7]. It also shown, the QHE phase can be evolve in the absence of spin-orbit coupling (SOC) and magnetic field, the complex hopping parameter can break the time reversal symmetry. These discoveries are the milestone for field of topological phase materials.

In the real materials graphene, Haldane model is generalized in the presence of SOC by Kane and Male, in 2005 [8]. This paper describes how time reversal symmetric system the spin up and spin down behaves like a opposite magnetic field. In this scenario, there is a non zero transverse current at the edge although there is no net charge current. This non zero current at the edge know as spin current, the phenomena called Quantum spin Hall (QSH) effect. The new phase is characterised by the topological invariant called Z_2 index [9]. Latter on on 2007, the QSH phase of the materials experimentally observed in 2D quantum well of HgTe[10, 11] . This idea was also generalized in 3D materials, it is called topological insulator which has topologically protected surface states [12].

Last decade, the field of topological material is well studied, in the early days, the time-reversal symmetry protected gaped topological material i.e topological insulator (TI) predicted theoretically and endorse experimentally [13, 14]. Extend the field with new discoveries, the crystalline symmetry protected gaped topological material called topological crystalline insulator (TCI) [15]. Furthermore, the idea of topological field theory extended with the new discoveries of gapless topological phase such as Weyl semimetal (WSM), Dirac semimetal (DSM) and Nodal line semimetal(NDLSM) etc [16, 17]. In the broken time reversal system (introduce magnetism), the interplay between magnetism and topology of gaped and gapless topological materials, the different exotic phase evolve i.e quantum anomalous Hall (QAH), Insulator or Axion Insulator (AI), magntic Weyl and nodal line semimetal (MWSM , MNDLSM)[18–23]. From the begging of the topological phases, the DFT based first principle calculation play an important role in
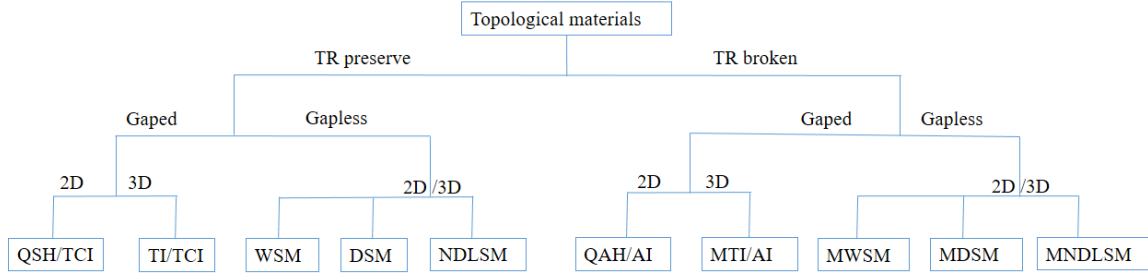
Figure 1.1: Schematic of different topological phases in TR preserved and TR broken materials.

predicting new topological phase, and latter on verified experimentally. In the field of condensed matter physics, identifying and exploring new phase of materials is a fascinating research area [24, 25]. The new phase of the materials comes with novel properties and physical phenomena , which holds immense possibilities of application from spintronics to quantum communication device[26].

The main aspect of this thesis is to explore new phases of materials in TRS preserved and TRS broken system. We have studied nonmagnetic and magnetic heterostructure of HgTe based materials and a new 2D material $MoSi_2Z_4$. Before going into the detailed discussion in the next sections, we will start the details of different topological phases [see schematic of Fig. 1.1] and there non local order parameters (topological invariant).

1.1 TR preserve topological phase

In this section, we will briefly describe different topological phases and topological invariant in the presence of time reversal system. The most important signature of topological phase is band inversion i.e the relative order of the band are inverted with respect to the atomic limit , at a certain momentum point(s) at the Brillouin zone (BZ). Both gaped and gapless topological materials shows band inversion, Based on the nature and location of the band inversion in the momentum space, various topological phase can be identified. The DFT based ab-initio calculation can easily identify the band inversion picture. Fig. 1.2 demonstrates the band inversion in a Topological materials HgTe in contrast of normal insulator CdTe, it shows specific momentum point Γ, the relative bands Γ_6 and Γ_8 are inverted.

1.1.1 Gaped 2D and 3D topological phases

As we discuss previously, the 2D and 3D gaped topological materials in TR symmetric system is classified depending on symmetries, mainly two types, (i) QSH insulator (in 2D) and TI (in 3D) shows topologically protected Dirac cone at the time reversal invariant momentum (TRIM) points protected by Time reversal symmetry, it is identified with $\mathbb{Z}_2$ invariant $(v_0, v_1 v_2 v_3)$, ,where v_0 and
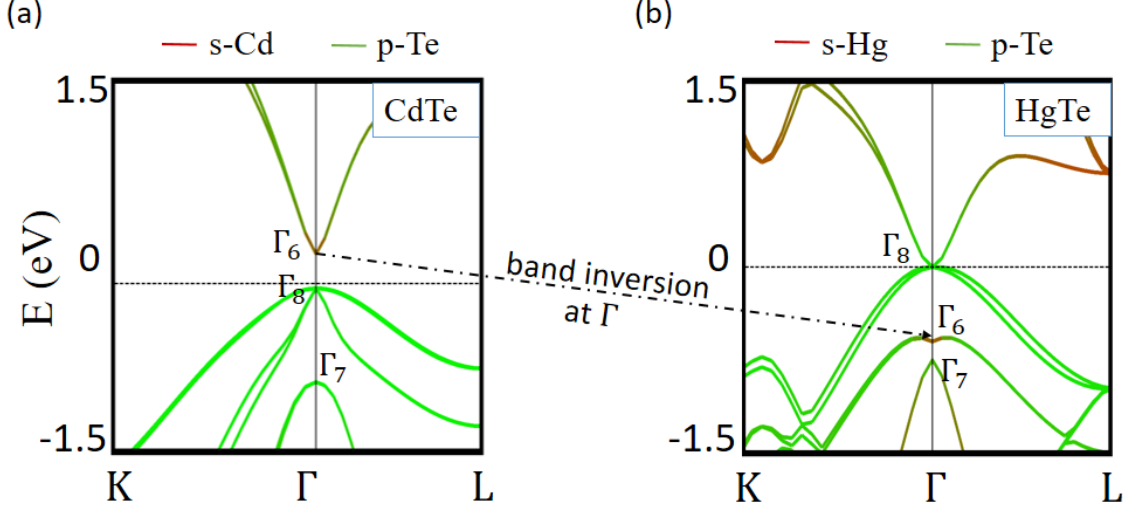
Figure 1.2: The band inversion of topological material HgTe in comparison to the normal insulator CdTe.

v_1, v_2, v_3 are strong and weak topological indices [24, 25]. (ii) TCI in 2D and 3D, the topological Dirac is protected by crystalline symmetries,band inversion can be noticed either either at non-TRIM points or even number of TRIM points in the BZ, resulting vanishing strong indices v_0 of $\mathbb{Z}_2$ invariant, So the Chern number or mirror Chern number can be used as topological invariant [15, 27]. Next, we will discuss different theoretical approaches to calculate topological invariants. $\mathbb{Z}_2$ **invariant:** There are many ways to calculate $\mathbb{Z}_2$ invariant[9], mostly used formalism is developed by Fu-Kane-Mele[12]. The $\mathbb{Z}_2$ invariant (v_0) is defined within this framework in a 2D system as : -

$$(-1)^{v_0} = \prod_{a=1}^{4} \delta_i \qquad (1.4)$$

where, δ_i is defined as δ_i= Pf $[\omega(k)/\sqrt{\omega(k)}]$ at the TRIM point. Here Pf is the Pfaffian of the unitary matrix $\omega(k)$ at specific TRIM points, the matrix $\omega(k)$ represents with its element $\omega_{mn} = U_m(k)\Theta U_n(-k)$, where U_n(k) is the Bloch function for the n$'$th band at k point. The calculation δ_i is simple for an inversion symmetric system, each bands has a definite parity eigenvalues at a TRIM points [12], as the TRIM points are remain invariant under inversion symmetry operation, δ_i can be expressed as-

$$\delta_i = \prod_{m=1}^{N_{occ}} \zeta_{2m}(k) \qquad (1.5)$$

where $\zeta_{2m}(k) = \pm 1$,is the parity of the $2m^{th}$ band at the ith TRIM point, and N$_{occ}$ is the number of occupied bands. In case of 2D system, any time reversal symmetric insulator can be represented with only strong indices of $\mathbb{Z}_2$ invariant, the odd value of v_0 indicates system is trivial and even value of v_0 corresponds to the non trivial phase of the materials.

4

In case of 3D system, the number of TRIM point is eight, the $\mathbb{Z}_2$ invariant could have both strong and weak indies($v_0; v_1 v_2 v_3$) [9, 12]. The strong indies can be represent as -

$$(-1)^{v_0} = \prod_{a=1}^{8} \delta_i \tag{1.6}$$

While, the other weak indies can be defined as the following way-

$$(-1)^{v_{j=1,2,3}} = \prod_{n_j=1; n_{k \neq j=0,1}} \delta_i \tag{1.7}$$

where n is the coefficient related to reciprocal lattice vector and can take value 0 or 1. For strong topological insulator $v_0 = 1$ and other three indies (v, v_2, v_3) could be zero or nonzero, while weak topological materials has only non zero weak indies (v, v_2, v_3) and zero strong indies v_0. These four indies are zero, in the case of trivial insulators. The $\mathbb{Z}_2$ invariant can be calculated for both centrosymmetric (presence of inversion symmetry) and non-centrosymmetric (absence of inversion symmetry) using the Wannier charge centre evaluation [28].

Chern number (C) and mirror Chern number (M_C) : Chern number is a topological invariant, it is calculated by the integration of Berry curvature over the first BZ. It can be defined as-

$$C^{\pm i} = \frac{1}{2\pi} \sum_n \int_M \Omega^{\pm i}.ds \tag{1.8}$$

where, Ω denotes the Berry curvature sum over occupied bands. The non zero Chern number distinguishes the trivial and nontrivial phase.

In the case of mirror symmetric system the Hamiltonian H(k_m) commutes with the mirror operator (M) i.e $[H(k_m), M] = 0$ in the mirror symmetric momentum plane. The bands corresponds to the plane can be assigned with definite mirror eigenvalues of the values $\pm i$ as $M^2 = -1$ in the presence of SOC. So, the Hamiltonian can be split into two sub-spaces as-

$$H = H^{+i} \oplus H^{-i} \tag{1.9}$$

Finally, we can define Chern number for each sub-spaces, and the mirror Chern number (C_M) can be expressed in terms of subspace Chern number as-

$$C_M = \frac{C^{+i} - C^{-i}}{2} \tag{1.10}$$

In case of time reversal symmetric system, the mirror Chern number C_M is a $\mathbb{Z}_2$ invariant. When time reversal symmetry is broken in the system, the C^{+i} and C^{-i} are not related, so the mirror Chern number become $\mathbb{Z}_2 \times \mathbb{Z}_2$ invariant [27].

One of the most important signature of topological materials is (d-1) dimensional topological state of s d-dimensional materials, which connect conduction and valence band. In case of 3D system, it has topological surface state which generally appear with a massless Dirac cone, the states are protected by time reversal symmetry. As we discuss before, at the TRIM points, the odd number

of surface Dirac cone appear in case of strong TI, whereas the even number of surface Dirac cone appear in case of weak TI. The Dirac cone in weak TI is less robust in contrast of strong TI . Unlike topological insulator (TI), which hosts surface states protected by time-reversal symmetry, the surface state in topological crystalline insulator (TCI) is protected by the crystalline symmetries (i.e rotational symmetry (c_n), mirror symmetry (M), glide plane etc) [29, 30]. The surface Dirac cone appear only particular plane which respect corresponding symmetry operations, whereas TI host surface states in every surface. For example,in case of a mirror symmetric system, the surface Dirac cone appear perpendicular to the mirror plane. In case of two fold rotational symmetry (c_2) protected TCI has surface Dirac cone in the plane of rotational axis[31]. Another unique and important properties of a time-reversal symmetric topological insulator is spin-momentum locking (i.e spin is locked at right angle of the momentum). As a result, the opposite spins propagate in in opposite direction and a perfect spin polarization of the surface current, which provide a highly efficient spin-torque generation. All these properties of TI make it a promising materials candidate for a spintronics and quantum device application.

Here, we describe an example of a strong topological insulator (i.e Bi_2Se_3) and a topological crystalline insulator (i.e SnTe). In case of Bi_2Se_3, the topological nature is characterized by the $\mathbb{Z}_2$ invariant (1,000) [32, 33]. The band inversion in Bi_2Se_3 yield is a strong topological insulator. Fig. 1.3 (a) show the surface band structure projected on (001) surface, the single surface Dirac cone is located at the TRIM point in the BZ. For a mirror protected TCI phase in SnTe, the band inversion happened at the L points of the face centred cubic BZ (fcc BZ) . The fcc BZ has four L points, as consequence the strong topological indies (ν_0) is zero. However, topological nature can
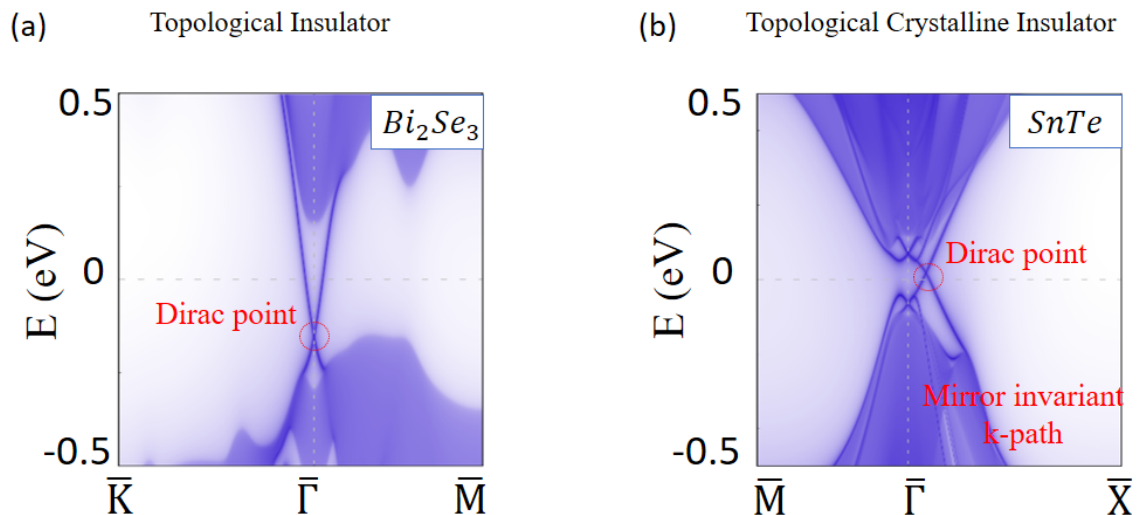
Figure 1.3: The comparison of surface state of (a) Topological insulator (Bi_2Se_3) and (b) topological crystalline insulator (SnTe).

be identified by mirror Chern number, the SnTe has mirror Chern number mod $C_M = 2$ as L points located at the M_{110} mirror invariant momentum plane [15], as consequence the mirror protected Dirac cone along the projected mirror line of the (001) surface of the BZ as shown in Fig. 1.3 (b).

1.1.2 Gapless 2D and 3D topological phases

The inverted band order is not only limited to the gaped system. So, the idea of topological protection can be extended to various gapless system. The presence of a gap closing point in the BZ is restrict to assigned a global topological invariant like TI and TCI, although locally topological invariant can be assigned for a particular momentum points, where the valence band and conduction band are separated in the BZ [16, 34]. For example, if C = 0 at $k_z = 0$ and C = 1 at $k_z = 0.5$, this indicated there is a gapless point in the k_z plane. In contrast of topological materials, mainly three different type of gapless topological semimetal phase reported till date such a Dirac semimetal(DSM), Weyl semimetal(WSM) and Nodal line semimetal. Now, we will discuss briefly these topological semimetallic phases.

1.1.2.1 Dirac Semimetal:

A four fold degenerate linear band crossing (gapless point) at the certain point of the momentum path, which is generally prone to the gap opening. These gapless points are stable under certain condition. In the low energy excitation, these gapless points respect the massless Dirac equation of the particle physics [16]. The Dirac Hamiltonian can be written as-

$$H = \begin{bmatrix} m & v\vec{k}.\vec{\sigma} \\ v\vec{k}.\vec{\sigma} & -m \end{bmatrix} \tag{1.11}$$
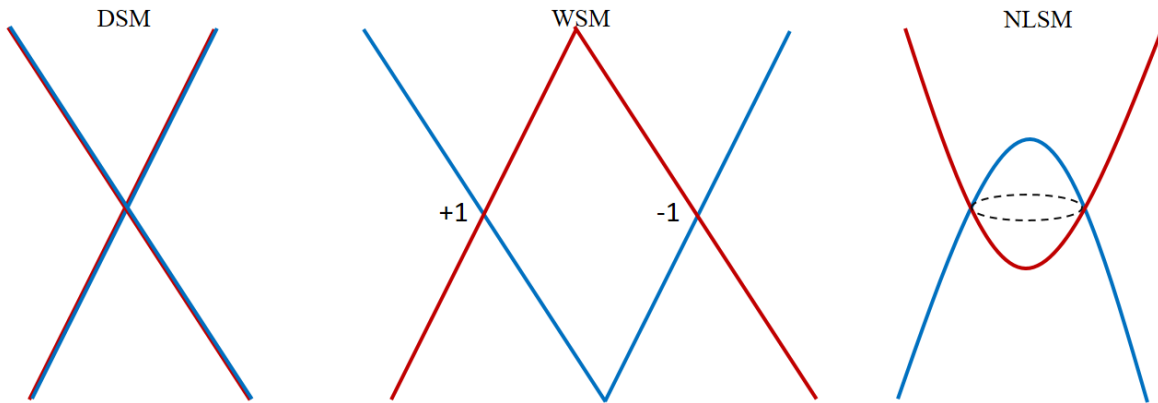
Figure 1.4: The schematic diagram of different topological materials.

where, the m and v are the mass term and velocity respectively. The $\sigma = (\sigma_x, \sigma_y, \sigma_z)$ is the Pauli matrix. When phase transition occur from trivial to topological state, the m change sign " $+$ " to " $-$ " and at the critical point achieved when m vanishes which correspond to massless Dirac fermion. At the critical point, the original Hamiltonian decouple into a Hamiltonian as-

$$H = \begin{bmatrix} 0 & v\vec{k}.\vec{\sigma} \\ v\vec{k}.\vec{\sigma} & 0 \end{bmatrix} \tag{1.12}$$

The material which poses massless Dirac fermion is known as Dirac semimetal.
The Dirac semimetal can be classified depending on the origin of the protection of the gapless point. depending of protection of the gapless point, it is could be (i) accidental band crossing (ABC) host DSM and (ii) the symmetry enforced band crossing (SBC) host DSM [35].
ABC host DSM : When the time reversal symmetry (T) and inversion symmetry(P) coexist in a materials the spins are double degenerate at each k point. In such a system, if two bands cross each other, it leads to a DSM. Due to the coexistence of P and T symmetry, the Berry curvature vanishes over the whole BZ, so the DSM has a net topological charge that is zero. So it is less robust against perturbation. However, the presence of crystalline symmetries help to stabilize the four fold degenerate band crossing and protected from the gap opening. Although, the Dirac point crossing created due to ABC can be protected by the crystalline symmetries, but the ABC is not enforced by the symmetries. Most well known such Dirac semimetal ar like Na_3Bi and Cd_3As_2 [36–40].
SBC host DSM : The symmetry-enforced DSM only exist at the high symmetry points of the boundary of the BZ. This type of DSM required specific symmetries, it is characterized by the four dimensional irreducible representation (FDIR) using the wave function around the crossing points. It is robust, therefore gapless points can't be gaped without breaking the particular symmetry. Generally, it is difficult to find a symmetry-enforced DSM due to the constrain of the FDIR, requirement of the linear dispersion in all directions and the position of the Dirac point near the Fermi level. The β- BiO_2 is a well known material candidate for such Dirac semimetal[41, 42].
Although the chiral charge of the DSM vanishes, it is possible to identify DSM with its topology. For example, the DSM material has non zero topological invariant ($\mathbb{Z}_2$) on a specific momentum plane, and band crossing on a mirror plane is classified with mirror Chern number. The DSM also shows topological surface state around the Dirac point. Fermi surface of the DSM also shows Fermi arc like state which connects the projected Dirac point, the chirality +1 and -1 coincide at the same point[16].

1.1.2.2   Weyl Semimetal

One should go back to the Dirac Hamiltonian in Eq. 1.11 to understand basics of the Weyl semimetal. It reveals, the Dirac Hamiltonian decoupled into two separate equations given by

$\pm v\vec{k}.\vec{\sigma}$. These each equations correspond to the two component of chiral Weyl fermion with chirality ± 1. This argument holds when the Kramers degeneracy is not preserved for every momentum point k, which means either time reversal($\mathscr{T}$) or particle-hole($\mathscr{P}$) symmetry should not present, at least one symmetry must be broken [16]. In a such condition, a linear two fold degenerate band crossing of non-degenerate band can occur in any generic momentum points k in the three-dimensional BZ. In the presence of crystalline symmetry can restrict the band crossing at a particular momentum point. The Hamiltonian around the Weyl point can be expanded as-

$$H(\delta k) = \epsilon_0(k_0) + v_0.\delta k + \sum_{i,j=x,y,z} v_{ij}\delta k_i \sigma_j \qquad (1.13)$$

where, $\sigma_{x,y,z}$ are the Pauli matrices and $v_0, v_{x,y,z}$ characterize the band dispersion near band crossing point. The 3rd term of the eq^n is encode the topological character of the Weyl point, it act as a monopole of momentum space Berry curvature. The Berry curvature ($\mathscr{F}_n^{ab}(k)$) and Berry connection ($A_n^a(k)$) of a particular energy band are defined as-

$$\mathscr{F}_n^{ab}(k) = \nabla^a \mathscr{A}_n^b(k) - \nabla^b \mathscr{A}_n^a(k), \qquad \mathscr{A}_n^a(k) = -i\psi_n(k)\nabla^a\psi_n(k) \qquad (1.14)$$

where $\nabla^a \equiv \delta/\delta k_a$ and a,b=x,y,z. The two important fact of Weyl physics are- (i) As Nielsen-Ninomiya theorem state that "the total monopole charge integrated " over the BZ mush banishes, sum over all chiral fermion must be zero" [43]. This indicate Weyl fermion always exist as a pair of opposite monopole charge .(ii) The Beery curvature vanishes if both $\mathscr{T}$ and $\mathscr{P}$ symmetry preserve, as $\mathscr{T}$ symmetry implies $\mathscr{F}_n^{ab}(k) = -\mathscr{F}_n^{ab}(-k)$ and $\mathscr{P}$ symmetry implies $\mathscr{F}_n^{ab}(k) = \mathscr{F}_n^{ab}(-k)$. Hence, the Berry curvature of a monopole charge of a Weyl point demonstrating that the existence of Weyl point requires at least one of these symmetries to be broken.

As a consequence, the Weyl semimetal shows important signature in Fermi surface and Berry curvature. In the Fermi surface, it hosts the Fermi arcs which connect the chiral partner of a Weyl point. Similarly, the Weyl points of chirality +1 and -1 act as a source and sink of the Berry
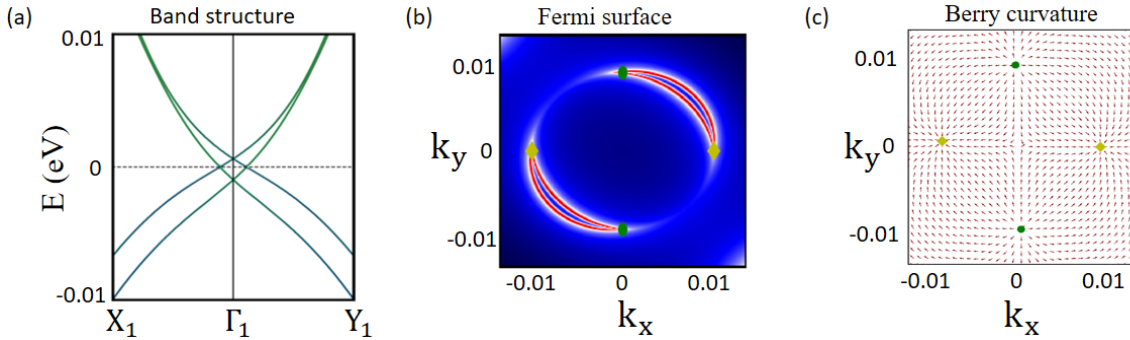

Figure 1.5: (a) The DFT band structure around Weyl points. (b) the Fermi surface projected on (001) surface and (c) associate berry curvature at fixed k_z plane of the HgTe/HgSe 3D superlattice.

9

curvature, respectively. As an example we will discuss a $\mathscr{P}$ broken system i.e HgTe/HgSe 3D superlattice. Fig. 1.5 (a) shows two fold degenerate band crossing leads to a Weyl semimetal phase, the Fermi surface projected on 001 surface shows Fermi arcs which connect opposite chirality [see Fig. 1.5 (b)]. The Berry curvature of this material in Fig. 1.5(c) shows chirality +1 (green circle) and chirality -1 (yellow diamond) act as a source and sink of the Berry flux.

In the past decade, several Weyl semimetals have been explored, the materials like TaAs, NbAs, WTe2, LaAlGe etc illustrate the inversion breaking Weyl semimetal where as $Co_2Sn_2S_2$ and Co_2MnGa are the time reversal symmetry broken magnetic Weyl semimetals[44–48]. Due to its distinct Berry curvature properties, the WSM shows interesting physical properties such as chiral anomaly, anomalous Hall effect, axion electrodynamics etc.. [16, 49].

1.1.2.3 Nodal line Semimetal

The another type of gapless topological semimetal is the nodal line semimetal(NDLSM). it features a gapless points along an one dimensional nodal lines of a linear band crossing of the conduction and valence band, unlike a zero dimensional band touching points in DSM and WSM. The band crossing of the nodal lines can be four fold degenerate (Dirac nodal line semimetal) and two fold degenerate (Weyl nodal line semimetal), it is protected by the crystalline symmetries of the materials. Generally, such band crossing occur when bands with different crystal symmetry eigen value cross along a rotational axis or on a mirror or on the glide-invariant plane in the BZ [50]. A nodal line semimetal can be classified with the topological invariant, Fermi surface geometry and linking structure of the multiple nodal line. Now, we can discuss different nodal lines -

$\mathbb{Z}_2$ **Berry phase nodal line semimetals:** In the presence of vanishing spin-orbit coupling in a $\mathscr{T}$ and $\mathscr{P}$ symmetric system, the four fold degenerate (kramers degeneracy) band crossing along one dimensional nodal line is belongs to Berry phase nodal line semimetal class. The presence of the $\mathscr{P}$ symmetry indicate one could analyzed $\mathbb{Z}_2$ using the parity of the Bloch state at the TRIM points. Similarly, the Berry curvature around the TRIM point give rise to $\mathbb{Z}_2$ invariant like 3D TI. Once strong spin-orbit coupling introduce in the system, the gap become open and the $\mathbb{Z}_2$ phase Dirac semimetal turned into a 3D TI, it doesn't change the band inversion but change the parity eigenvalues of the occupied Bloch state. The band inversion can be tuned with impurity of strain, it also influences the size of the nodal line which is a interesting platform to study correlated materials and flat band physics. Examples of the $\mathbb{Z}_2$ Berry phase nodal line semimetals are the ZrSiS[51–53] family TiB$_2$ [54, 55] family and Mg$_3$Bi$_2$ [56] etc.

$\mathbb{Z}_2$ **monopole charge nodal line semimetals :** unlike $\mathbb{Z}_2$ Berry phase nodal line semimetal, a nodal line semimetal can have quantized monopole charge when the $\mathscr{T}$ and $\mathscr{P}$ are preserve and the spin orbit coupling is vanishingly small. The $\mathbb{Z}_2$-quantized monopole charge nodal line is more stable as the can only be remove by pairwise annihilation, a isolated charge monopole nodal line cannot be removed [57, 58]. This phenomena is quite similar to Weyl physics. The non trivial
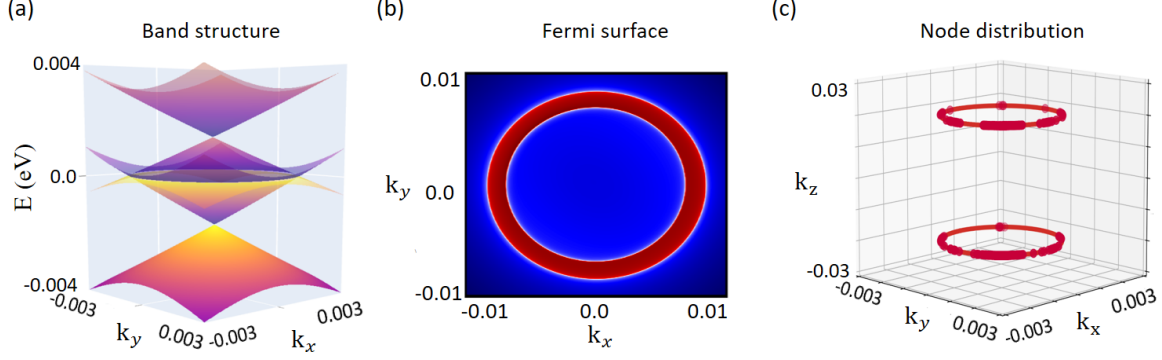
Figure 1.6: (a)The 2D band structure at a fixed k_z plane (b) the Fermi surface projected on (001) surface around the nodes and (c) associate node distribution in a 3D BZ of the HgTe/HgSe 3D superlattice.

phase of the $\mathbb{Z}_2$ monopole charge nodal line semimetal is characterized by Wilson loop evaluation. Example of such nodal line is ABC stucking of the graphdiyne[59, 60].

Mirror symmetry and glide mirror symmetry protected nodal line semimetal : In the presence of mirror symmetry ($\mathscr{M}$) or glide-mirror symmetry ($\mathscr{G}$), the materials can host a nodal line in the mirror (glide) symmetry-invariant plane. The bands can cross each other without hybridization if bands comes from different mirror (glide) symmetry. In the absence of the SOC, let us consider a mirror operator in a k_z plane $\mathscr{M}_z$. In the momentum space-

$$\mathscr{M}_z : (k_x, k_y, k_z) \rightarrow (k_x, k_y, -k_z) \tag{1.15}$$

and the Hamiltonian must satisfy-

$$\mathscr{M}_z^{-1} H(k_x, k_y, k_z) \mathscr{M}_z = H(k_x, k_y, -k_z) \tag{1.16}$$

In order to obtain the band crossing associated with the mirror operator $\mathscr{M}_z$ can be observed at a fixed k_z plane and the eigenvalue of conduction E_{CB} (k_x,k_y) should be equal to the eigenvalue of valence band E_{VB} (k_x,k_y). The mirror operator $\mathscr{M}_z$ creates a constraint of the k_z plane, it makes a band crossing points of a one dimensional line in the k_x-k_y plane. Since the mirror operator is invariant on a fixed plane, the nodal line is locked to that plane. This kind of nodal line can be from with accidental band crossing and doesn't required partner like $\mathbb{Z}_z$ monopole charge nodal line. Once the strong spin-orbit coupling is present in the system the mirror symmetry protected nodal line can be either annihilated or split into two fold degenerate Weyl nodes, this depends on the presence of other symmetries. The example of mirror protected nodal line semimetals are CaAgP [61, 62] and PbTaSe$_2$[63] families.

The non trivial nature of a nodal line semimetal give rise to topological surface state known as drumphead surface state. As a example here we demonstrate the band structure of a fixed
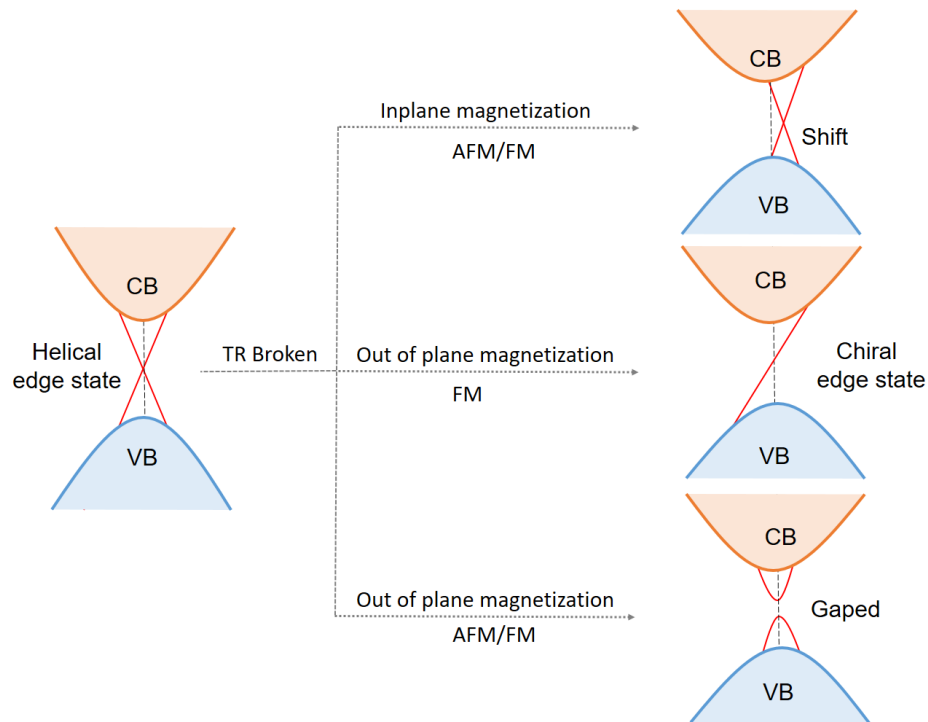
Figure 1.7: Schematic of the changes in topological states due to the presence of magnetism, depicted in a simplified form, and showing the effects of magnetism with varying magnetic orientations.

k_z plane which creates one-dimensional node distribution in Fig. 1.6(a), associate topological surface state are shown in the Fermi surface projected on (001) is shown in Fig. 1.6(b), and the distribution of the one-dimensional line nodes in a 3D BZ shows that the nodes are locked to a fixed k_z plane [see Fig. 1.6(c)].

1.1.3 TR broken gaped and gapless topological phases

The realization of the quantum Hall insulator in the presence of external magnetic field is the first ever predicted magnetic topological insulator. Latter on Haldane shows, the magnetic topological phase can be achieved without external magnetic field, in the presence of magnetic impurity or intrinsic magnetic order can host quantized Hall conductivity. Depending on the magneto-electric coupling response in the presence of intrinsic magnetization, the behaviour of anomalous Hall conductivity, it also influence the topological surface state as shown in Fig. 1.7, which leads to different magnetic insulator phases [64]. We will discuss those phases in details-

Anomalous quantum Hall insulator: In the presence of ferromagnetism in the topological insulator, the Hall conductivity become quantized to $\pm e^2/h$ and known as quantum anomalous Hall insulator. As the ferromagnetism induced exchange splitting pushed the one set of spin-polarized band to the topologically trivial or bulk bands, it host only one spin channel which

connect the valence and conduction bands and remain topologically connected. In case of 2D materials, this topologically protected spin channel is called as chiral edge state. However in 3D materials, a gap will be open at the surface perpendicular to the magnetization direction or cloud host chiral surface state. For example, the magnetically doped Bi_2Te_3 family and HgTe materials are theoretically predicted as a QAHI[65], latter on experimentally validated in Bi_2Te_3 [18] compound successfully however HgTe need external magnetic field [66].

Axion insulator: In the topological insulators , the gaped surface state resulting from local breaking $\mathcal{T}$ is enforced a half quantized anomalous Hall conductivity (AHC) of $e^2/2h$. This connected to the axion phase angle θ which is characterized by the formula of Chern Simons magnetoresistance coupling. Its represents as-

$$S = \frac{\theta e^2}{4\pi^2 h} \int d^3 x dt E.B \qquad (1.17)$$

where θ has the values 0 or π, E and B are the electric and magnetic respectively. The term $\theta = \pi$ for the strong TI case and $\theta = 0$ for the topologically trivial vacuum phase, this corresponding to the "axion $\mathbb{Z}_2$" classification. The important signature of the axion insulator are (i) the half quantized surface AHC , (ii) gaped topological surface state, (iii) the Chern number is zero as net AHC is zero [22, 67]. The half quantized surface AHC of the top and bottom surface are cancel out which lead to the C = 0 in case of AI, where as in AQHI it is added to make C=1. The AI phase is predicted in 2D materials such as $MnBi_2Te_4$ family and in 3D ferromagnetic materials axion insulator state is noticed which shows part of chiral hinge state similar to the higher order topology [68]. the experimental observation of the AI is not successfully done in $MnBi_2Te_4$ material class [19].

Antiferromagnetic topological insulator: Consider an antiferromagnet that breaks a crystal's primitive lattice translation symmetry ($t_{\frac{1}{2}}$) and time reversal tau while maintaining the combinations $S = \tau t_{\frac{1}{2}}$. The S symmetry results in a Z2 topological classification of insulators that distinguishes between the "antiferromagnetic topological insulator" (AFTI) phase and the regular insulator phase. Its features, including a quantized magnetoelectric effect, are similar to those of the "strong" topological insulator with time-reversal symmetry. It also has been observed in the 2D materials in the presence of nonsymmorphic symmetry, the topological state are projected by the rotation symmetries. The interplay between AFM, symmetry, and topology, several AFM topological states with novel physical properties have been proposed [69, 70].

Several magnetic gapless topological phases are predicted theoretically and later observed experimentally, and they have quite similar signature like nonmagnetic topological gapless phases. Example of such materials are magnetic Weylsemimetals $Co_2Sn_2S_2$ and Co_2MnGa [44–48].

1.2 The main theme and content of the thesis

METHODOLOGY

We have used extensively ab-initio method in this thesis as a theoretical tools. The three step process [see Fig- 2.1] has been adopted for calculating topological properties, these steps are-(i) Density functional theory (DFT) based calculation using VASP code[71] to extract Bloch function, (ii) Wannier function based tight-binding (TB) parameters and Hamiltonian from DFT using wannier90 code [72, 73], (iii) TB modelling for electronic properties using wanniertools code [74]. The DFT based technique along with wannier function based TB approach widely used as an powerful theoretical tools to explore new exotic topological phase of materials [75, 76]. As the name ab-initio suggests, DFT method don't rely on empirical parameters and is capable in predicting topological properties from crystal structure of the materials (i.e electronic density of the structure). Last decades, theoretically predicted new topological materials using ab-initio method were verified experimentally. In predicting new topological materials, this method indeed a very powerful technique.

This chapter describes the overview of DFT and Wannier based tight-binding methods. In sec. 2.1, we discuss about many body problem to one electron problem. In sec. 2.2, we review different concept and aspect of DFT methods, this include Kohn-sham theorem, plane wave basis set, pseudo potentials and different exchange correlation functional formalism. In sec 2.3, we will discuss about the constructing of the Wannier tight-binding Hamiltonian from DFT. Finally, we have illustrate the methods to obtain topological invariant (i.e. Z_2, Chern number etc..), surface states, anomalous Hall conductivity using Wannier based tight binding formalism incorporated in wanniertools.

Step1: Density functional theory (DFT) using VASP

$$\left[-\frac{\hbar^2}{2m}\nabla_i^2 + V_s(\vec{r})\right]\varphi_i(\vec{r}) = \epsilon_i\varphi_i \text{ where } V_s(\vec{r}) = V(\vec{r}) + \int \frac{e^2 n_s(\vec{r}')}{|\vec{r}-\vec{r}'|}d^3r' + V_{xc}[n_s(\vec{r})]$$

Step2: tight-binding Hamiltonian using wannier90 interface with VASP

$$\omega_{nR}(r) \quad = \quad \frac{V}{(2\pi)^3}\int_{BZ}\left[\sum_{m=1}^{N} U_{mn}^{(k)}|\varphi_{mk}>\right]e^{-ik.R}dk$$

$$hopping\ parameters\ from\ first-principles$$

Step3: tight-binding model using waniertools

$$H_{mn}(k) = \sum_{R} e^{ik.(R+\tau_m-\tau_n)}H_{mn}(r)$$

Figure 2.1: Schematic diagram of the methods used for predicting new topological materials

2.1 Many body electron system

The accurate properties of a material can be estimated with considering all possible interaction (i.e electron-electron, electron-nucleus,and nucleus-nucleus interaction) of the system. The Hamiltonian of a materials with many-body interaction is described as follows-

$$\hat{H} = \hat{T}_n + \hat{T}_e + \hat{V}_{n-n} + \hat{V}_{e-e} + \hat{V}_{n-e} \tag{2.1}$$

In Eq. 2.1 $\hat{T}_n$ and $\hat{T}_e$ represents the kinetic energy of the nuclei and electron of the system

$$\hat{T}_n = \sum_{\alpha=1}^{K} \frac{(-i\hbar\nabla_{R_\alpha})^2}{2M_\alpha}$$

$$\hat{T}_e = \sum_{i=1}^{N} \frac{(-i\hbar\nabla_i)^2}{2m}$$

where, the R_α denotes Cartesian coordinate of α nucleus with mass M_α and m is mass of the electron in N electron system.

In Eq. 2.1, the interaction potentials between particles are represented as: the repulsive potentials of nucleus-nucleus and electron-electron are V_{n-n} and V_{e-e} respectively, the attractive potentials between nuclei-electron is V_{n-e} [77].

$$\hat{V}_{n-n} = \sum_{\alpha,\beta=1;\alpha<\beta}^{K} \frac{Z_\alpha Z_\beta e^2}{\left|\vec{R}_\alpha - \vec{R}_\beta\right|}$$

$$\hat{V}_{e-e} = \sum_{i,j=1;i<j}^{N} \frac{e^2}{\left|\vec{r}_i - \vec{r}_j\right|}$$

$$\hat{V}_{n-e} = -\sum_{\alpha=1}^{K} \sum_{i=1}^{N} \frac{Z_\alpha e^2}{\left|\vec{R}_\alpha - \vec{r}_i\right|}$$

where r_i and r_j denoting the position of ith and j^{th} electron. The Hamiltonian of a many electron system can be written as -

$$\hat{H} = \sum_{\alpha=1}^{K} \frac{(-i\hbar\nabla_{R_\alpha})^2}{2M_\alpha} + \sum_{i=1}^{N} \frac{(-i\hbar\nabla_i)^2}{2m} + \sum_{\alpha,\beta=1;\alpha<\beta}^{K} \frac{Z_\alpha Z_\beta e^2}{\left|\vec{R}_\alpha - \vec{R}_\beta\right|} + \sum_{i,j=1;i<j}^{N} \frac{e^2}{\left|\vec{r}_i - \vec{r}_j\right|} - \sum_{\alpha=1}^{K} \sum_{i=1}^{N} \frac{Z_\alpha e^2}{\left|\vec{R}_\alpha - \vec{r}_i\right|} \quad (2.2)$$

By considering all term of the Hamiltonian in Eq. 2.4, one can solve the time-independent Schrödinger equation to get the electronic properties of a many-electron system.

$$\hat{H}\ \Psi = E\ \Psi \quad (2.3)$$

Here, E and Ψ are the eigenvalues and many-body electronic system. The real systems poses very high number $\sim 10^{23}$ of ions and electrons, it make difficult to get exact solution of the equation with available resource in recent world. In order to solve this equation, approximations are required.

The first and important approximation in Eq.2.5 is Born Oppenheimer approximation [78]: since the ions in a typical solid move much slowly compared to the electrons, one can decouple the motion of electrons and ions. According to this approximation, the kinetic energy of ions is neglected and potential energy is merely constant. Thus, Hamiltonian reduces to -

$$\hat{H} = \sum_{i=1}^{N} \frac{(-i\hbar\nabla_i)^2}{2m} + \sum_{i,j=1;i<j}^{N} \frac{e^2}{\left|\vec{r}_i - \vec{r}_j\right|} - \sum_{\alpha=1}^{K} \sum_{i=1}^{N} \frac{Z_\alpha e^2}{\left|\vec{R}_\alpha - \vec{r}_i\right|} \quad (2.4)$$

Due to this approximation, we can decouple wave function that can be written as as a product of electronic and ionic wave functions i.e-

$$\Psi = \psi_{ik}^{n}(\vec{R}_\alpha)\ \psi_k^{e}(\vec{r}_i, \vec{R}_\alpha) \quad (2.5)$$

The Schrödinger equation with Born-Oppenheimer approximation can written as-

$$[\hat{T}_e + \hat{V}_{e-e} + \hat{V}_{n-e}]\ \psi_k^{e}(\vec{r}_i, \vec{R}_\alpha) = E_k(R-\alpha)\ \psi_k^{e}(\vec{r}_i, \vec{R}_\alpha) \quad (2.6)$$

The Eqn.2.6 represents a stationary eigenvalue problem for any sets of frozen ions located at R_α. The ground state configuration by solving Eqn.2.6 is a formidable task due to (i) large number and quantum nature of the electrons (ii) complicated geometry of many electron system (iii) a number of meta-stable state arrangement of the nuclei. So more efficient approximation is needed to handle this problem even the motion of ions is ignored. The next simplest and effective Hartree-Fock (HF) or (self consistent field approximation) [79], in which the ground state wave

function ψ_0^e of a many electron system represent in terms of a product of individual single particle states or so-called Slater determinant.

$$\psi_0^e(\vec{r}_1\sigma_1,.....\vec{r}_N\sigma_N) \approx \phi_{1...N}(\vec{r}_1\sigma_1,.....\vec{r}_N\sigma_N) \tag{2.7}$$

where,ϕ_i and σ_i are the single electron wave function and spin of a N-particle system and ground state wave of function $\phi_{1...N}$ are determined variationally. The HF equation looks similar to the ordinary Schrödinger equation, the effective potential is non local in nature with two terms the (i) Hartree (direct Coulomb) potential $V_H(r)$ and (ii) the exchange potential V_x^{HF}.

$$\left[\frac{(-i\hbar\nabla_i)^2}{2m} + V_H(r) + V_x^{HF} \right] \phi_i(\vec{r},\sigma) = E_i\phi_i(\vec{r},\sigma) \tag{2.8}$$

where, $V_H(r)$ and $V_x^{HF}(\vec{r}\sigma,\vec{r}'\sigma')$ cab be express as-

$$V_H(r) = \int \frac{d^3r'}{|\vec{r}-\vec{r}'|} \sum_{\sigma'=\uparrow,\downarrow} \sum_{j\neq i} |\phi_j(\vec{r}'\sigma')|^2$$

$$V_x^{HF}(\vec{r}\sigma,\vec{r}'\sigma') = -\frac{e^2}{|\vec{r}-\vec{r}'|} \sum_{j=1}^N \phi_j(\vec{r}\sigma)\phi_j^*(\vec{r}'\sigma')$$

The potentials estimated self consistently : start with the initial guess of the total potential, the states ϕ_i and the potentials which improves step by step. This iterative process is stopped once a suitable accuracy is achieved. The electrons in HF approach the average field of the complete electron cloud and ignored Couloumb repulsion between electrons. In order to incorporate Coulomb repulsion, one has to include unoccupied states (finite or infinite) along with occupied states in the HF ground state. The improved correlated wave function can be expressed as-

$$\psi_k(\vec{r}_1\sigma_1,.....\vec{r}_N\sigma_N) = \sum_{i_1....i_N} c_{i_1...i_N}^k \phi_{i_1...i_N}(\vec{r}_1\sigma_1,.....\vec{r}_N\sigma_N) \tag{2.9}$$

The expansion coefficient can be determined using various methods. For efficient numerical implementations, the single-particle orbitals from which $\phi_{i_1....i_N}$ are constructed can must be expanded in terms of some finite set of basis functions -

$$\phi_i(\vec{r}\sigma) = \sum_{k=1}^M b_{i,k\sigma}\eta_k(\vec{r}) \tag{2.10}$$

Using the matrix elements $\langle\eta_k|\eta_l\rangle$, Eq. 2.8 can be turned into a eigenvalue problem, where $b_{i,k\sigma}$ and determine either sequentially or simultaneously. According to to the HF scheme, the effective single particle scheme is wind up with

$$\sum_{l=1}^M \sum_{\sigma'} \left[\left\langle \eta_k \left| -\frac{(\hbar\nabla_i)^2}{2m}\delta_{\sigma,\sigma'} + \hat{v_{eff},}\sigma,\sigma' \right| n_l \right\rangle - \epsilon_i \langle\eta_k|\eta_l\rangle \right] b_{i.l\sigma'} = 0 \tag{2.11}$$

Where, $\hat{v_{eff}.}\sigma,\sigma'$ is the total potential experience by electrons. In the correlated ab-initio method, the computational demands is increased by a factor of the order of the electron number

N: M scale linearly with it. To improve correlation calculation, the method like Møller and plesset (the second and fourth perturbation theory, MP2 or MP4), configuration interaction (CI), multi-configuration self-consistent field (MCSCF) , couple cluster approach (CC), are quite accurate, but very expensive in terms of computational cost. Next question arise, are there any effective method which can map a fully interactive many-body problem onto an effective single particle problem in a more complete fashion which includes correlation in some way. The answer is yes, the density functional theory (DFT) is the alternative and remarkable theory that replace wave function approach by simpler electron density (ρ).

2.2 Density functional theory (DFT)

The central idea in Density functional theory is to use the electronic density instead of wave function of a many-body system which reduces the number of scaling factor in numerical algorithm, the ground state electronic density can be represented as-

$$
\begin{aligned}
\rho(\vec{r}) &= \langle \Psi_0 \left| \hat{\rho}(\vec{r}) \right| \Psi_0 \rangle \\
&= N \sum_{\sigma_1....\sigma_N} \int d^3 r_2....d^3 r_N \left| (\vec{r}_1 \sigma_1, \vec{r}_2 \sigma_2...\vec{r}_N \sigma_N) \right| \Psi_0 \rangle |^2
\end{aligned}
\tag{2.12}
$$

This idea was formulated in a proper framework by Hohenberg and Kohn in 1964 [80] in term of two theorems :

$\diamondsuit$ The extend potential V_{ext}(r) of an interacting many-electron system can be expressed as a unique functional ground state energy of this system is also a unique function of ρ(r) i.e E=E[ρ].

$\diamondsuit$ The total energy functional, E[$\rho(r)$] has a minimum equal to ground state energy corresponding to ground state density $\rho(r)$.

2.2.1 Kohn-Sham equation

Unfortunately, the explicit form of E[$\rho(\vec{r})$] is not described in Hohenberg-Kohn (HK) theorem. This problem can be simplified by an exact mapping of the interacting N-particle problem onto a suitable effective non-interacting system. It is possible within Kohn-Sham (KS) scheme[81]. In the KS-scheme, the single particle orbitals are considered as KS orbital ($\Psi_i^{KS}(\vec{r})$) which reproduces the density of the actual system-

$$
\rho(\vec{r}) = \sum_{i=1}^{N} \left| \Psi_i^{KS}(\vec{r}) \right|^2
\tag{2.13}
$$

Here, the $\Psi_i^{KS}(\vec{r})$ follow the KS equation-

$$
\left[-\frac{(\hbar \nabla_i)^2}{2m} + V_{eff}^{[\rho]}(\vec{r}) \right] \Psi_i^{KS}(\vec{r}) = E_i \Psi_i^{KS}(\vec{r})
\tag{2.14}
$$

where, E_i are the KS eigenvalues, $V_{eff}^{[\rho]}(\vec{r})$ is the effective functional which is a function of the electron density ρ. The $V_{eff}^{[\rho]}(\vec{r})$ can be rewrite as-

$$V_{eff}^{[\rho]}(\vec{r}) = V_{ext}^{[\rho]}(\vec{r}) + V_{H}^{[\rho]}(\vec{r}) + V_{XC}^{[\rho]}(\vec{r}) \qquad (2.15)$$

$V_{ext}^{[\rho]}(\vec{r})$ is characterise the coupling between the particles and the external potential

$$V_{ext}^{[\rho]}(\vec{r}) = \int d^3r v_{ext}\rho(\vec{r}) \qquad (2.16)$$

$V_{H}^{[\rho]}(\vec{r})$ in the classical(Hartree) interaction energy between the N particles with density ρ

$$V_{H}^{[\rho]}(\vec{r}) = \frac{1}{2} \int d^3r \int d^3r' \frac{\rho(\vec{r})\rho(\vec{r}')}{|\vec{r} - \vec{r}'|} \qquad (2.17)$$

$V_{XC}^{[\rho]}(\vec{r})$ is the exchange-correlation functional which includes all complicated many-body effect

$$V_{XC}^{[\rho]}(\vec{r}) = \frac{\delta E_{XC}[\rho]}{\delta \rho(\vec{r})} \qquad (2.18)$$

Here E_{XC} is the exchange-correlation part of the total energy which considers all possible many-body effect assuming the validity of Eqn. 2.13. The exact from of the E_{XC} is unknown, it could be estimated self consistently as it is a function of electron density.

The Kohn-Sham equation can estimate exact ground state energy if the exact $V_{eff}^{[\rho]}(r)$ is estimated. The exact form of the exchange-correlation term of a many electron system is tricky to know and computationally expensive. The various approximation method incorporated in DFT to calculated the $E_{XC}[\rho]$).

2.2.2 Exchange correlation functional

The exchange correlation functional E_{XC} consist of two part the Exchange $E_C[\rho]$ and correlation $E_X[\rho]$ functional in conventional many-body theory. It is calculated with various approximation, the two most popular approximations are the local density approximation (LDA)[82, 83] and the general gradient approximation (GGA)[84–86].

2.2.2.1 LDA approximation

The basis of all approximation exchange correlation approximation is the local density approximation(LDA)[82]. It is assumed that the whole electron gas has a slowly varying density profile $\rho(r)$. Therefore, the exchange correlation energy at a small elemental volume d^3r should remain locally homogeneous. Therefore, the E_{XC} within LDA approximation for the whole system is given by-

$$E_{XC}[\rho] = \int \rho(\vec{r})\epsilon_{xc}[\rho(\vec{r})]d^3r \qquad (2.19)$$

where $\epsilon_{xc}(\rho)$ is the exchange relation energy per particle uniform electron gas of the density $\rho(r)$. The form of ϵ_{xc} can be obtained from high level many-body calculations for a uniform electron gas.For example, the forms developed by Gunnarsson and Lundqvist or Ceperly and Adler are used in many of the current implementations of LDA.

2.2.2.2 GGA approximation

This approximation works pretty well for systems with uniform electron density. and therefore yields good results for the metals. Unfortunately, it underestimates the band gap of semiconductors up to 50%. Unlike LDA, the GGA approximation includes first order correction of the density. Therefore, it also includes the effect of local inhomogeneity of the electron density. The total exchange correlation energy can be expressed as-

$$E_{XC}[\rho(\vec{r})] = \int \rho(\vec{r})\epsilon_{xc}[\rho(\vec{r}), \nabla\rho(\vec{r})]d^3r \qquad (2.20)$$

The most famous implementation of GGA method is developed in 1963 by Perdrew, Burke and Ernzehof (PBE)[84]. The other implementations are by Predrew and Wang (PW91)[85] and various version of PBE version for solid PBE-sol [86] etc. In certain materials, the GGA works better than LDA. Similar to LDA, the GGA also underestimates the bandgap [87].

2.2.2.3 Beyond GGA

To improve the band gap problem and electronic structure of the materials, various methods are used in DFT, for example LDA+U,GGA+U scheme, van der waals correction (vdW) strategy, meta-GGA functional scheme, various hybrid functional like HSE and many body approach like GW etc [88–90]. In this thesis we have extensively used GGA,GGA+U,vdW, MBJGGA and HSE functional for the calculation of 2D vdW materials to 3D narrow gap semiconductors.
In the next section, we describe most popular method to solve the Kohn-Sham equation with the pseudopotential using a plane-wave basis set.

2.2.3 Plane wave basis set

According to the Bloch theorem, the crystal wave function for each band i and crystal momentum k can be written as-

$$\Psi_{ik}(\vec{r}) = e^{\vec{k}.\vec{r}}u_{ik}(\vec{r}), \qquad u_{ik}(\vec{r}+\vec{R}) = u_{ik}(\vec{r}) \qquad (2.21)$$

where $u_{ik}(\vec{r})$ is the cell periodic part with the lattice vector R, it is required to be expand in the some basis sets to perform numerical calculations. The choice of the basis set for solids is plane wave basis set. The Bloch wave function $\Psi_{ik}(\vec{r})$ can be expand in a plane wave basis set with periodic condition as -

$$\Psi_{ik}(\vec{r}) = \sum_G C_{i,k}^{\vec{G}} e^{i(\vec{k}+\vec{G})} \qquad (2.22)$$

Here, G is the reciprocal lattice vector, and $C_{i,k}^{\vec{G}}$ is the expansion coefficient. Ideally, the sum contains an infinite number of plane waves but it should be restricted to an optimal number of

plane wave to improve computational efficiency. In practice, only consider the all G vector within a sphere with a radius $\left|\vec{G}_{max}\right|$, keeping origin at the center[91]. The $\left|\vec{G}_{max}\right|$ is estimated from the kinetic energy cut off (E_{cut}) using the following equation-

$$E_{cut} = \frac{\hbar^2 \left|\vec{k} + \vec{G}_{max}\right|^2}{2m} \tag{2.23}$$

2.2.4 Pseudopotential

The wave function of the valence electron must satisfy the orthogonality condition with the core electron wave functions. As a results, the energy scale spanned by the core electrons energy scale spanned by the core electrons are vastly different from those of valence electron, the rapid oscillation of the wavefunction closer to the core of atoms. Therefore large number of plane waves are needed in Eq 2.22 to properly describe the valence electron wave function. But, the core electrons plan insignificant role in the properties of the solid. Therefore, an efficient approach named pseudopotential [91] approach can be used instead of the real potential, where the strong Coulomb potential of the nucleus and the effect of tightly bound core electron is replaced and an effective ionic potential acting on the valence electron.

Let us consider that the actual wave function of the system satisfies the Kohn-Sham[81] equation:

$$\left[-\frac{(\hbar\nabla_i)^2}{2m} + V_{eff}^{[\rho]}(\vec{r}) \right] \Psi_i^{KS}(\vec{r}) = E_i \Psi_i^{KS}(\vec{r}) \tag{2.24}$$

A pseudo wave function can constructed as-

$$\Psi_i^{KS}(\vec{r}) = (1 - \hat{P})\phi_i(\vec{r}) \tag{2.25}$$

where the projection operation P is given by,

$$\hat{P} = \sum_j \left|k_j\right\rangle\left\langle k_j\right| \tag{2.26}$$

Here, the P projects any function to the core states ($\left|k_j\right\rangle$). It can be shown that ψ_i(r) satisfies a similar equation as Ψ_i^{KS}(r) :

$$\left[-\frac{(\hbar\nabla_i)^2}{2m} + V_{ps}(\hat{r}) \right] \phi_i(\hat{r}) = E_i \phi_i(\hat{r}) \tag{2.27}$$

where, V_{ps}(r) is the pseudopotential and it can be expressed as -

$$V_{ps}(r) = V_{eff}^{[\rho]}(\vec{r}) - \left[-\frac{(\hbar\nabla_i)^2}{2m} + V_{eff}^{[\rho]}(\vec{r}) \right] \hat{P} + E_i \hat{P} \tag{2.28}$$

Note that, Eq. 2.27 yields the same eigenvalues as the actual equation. It is generally a smooth wave function and can be reproduced using a smaller set of plane waves. The pseudo wave functional generally mimics the true wave function beyond a cut off radius. Two methods are used

to calculate pseudo potentials a) norm-conserving approach developed by Kleinmab and Bylander, (b) the ultrasoft pseudopotential method developed by Vanderbilt. In case of norm conversing potential, the norm of an actual wave function must be reproduce using the norm of pseudo wavefunction within the cutoff radius. However, it is not maintained in ultrasoft pseudopotential. Usually ultrasoft pseudopotential is used less number of basis sets and less cut off energy. These type of pseudopotential is used in code like Quantum espresso[92].

Apart from the pseudopotential, there is projector augmented wave(PAW) method, it is lies in between all-electron and the pseudopotential. In this method, the wave function is decide into two part, 1st part is a partial wave expansion within a atom centered sphere, and 2nd part is pseudopotential outside augmented region. Therefore, PAW PAW method are better because they consider both core electrons, at the same time, used pseudopotential method to deal with valence electrons. The PAW potential is generally used in codes like VASP, GPAW etc... In this thesis, we have performed our calculation using PAW method in-build in VASP code.

2.3 Wannier based tight-binding model

In this sub section, we describe the tight-binding approach within the framework of the maximally localized Wannier functions (WF) [77, 93]. The Bloch wave function is generally expressed as a linear combination of localized orbitals. It is an efficient approach to explore accurate description of the electronic structure with less computational power. In case of topological materials [76, 94], the WF base tight binding approach appears to be a powerful tools in past decades. Specially, the denser k-point grid is essential for many topological electronic properties finding which is hard in DFT based coarse-grained sampling of the Brillouin zone (BZ). For example, the finding of Weyl point or nodal points which can be located in the any point of the BZ, or the calculation of the Berry phase/Berry curvature needs much dense k-grid. The main idea of Wannier based tight binding model is to extract the real space hopping parameter for the relevant bands near the Fermi energy [94]. This reduce the size of the matrix. The k-space Hamiltonian can be constructed using the real space hopping parameters.

The Wannier functions is considered as the Fourier transform of the Bloch functions [73, 77, 95], it is associated with the nth Bloch band Ψ_{nk} can be represented as-

$$W_{n,\vec{R}} = \frac{V_{cell}}{(2\pi)^3} \int_{BZ} e^{-i\vec{k}.\vec{R}} \Psi_{nk} d^3k \tag{2.29}$$

Here, R is the unit cell index, and V$_{cell}$ is the unit cell volume. Note that, since $\Psi_{nk}(r)$ has a gauge freedom, it can be smooth over the Brillouin zone by choosing a suitable gauge. The W$_{nk}$ decay rapidly with $|\vec{r} - \vec{R}|$. Therefore, Wannier functions are generally well localized and are orthogonal to each other in the real space, i.e.

$$\langle W_{mk} | W_{nk} \rangle = \delta_{mn} \delta_{RR'} \tag{2.30}$$

23

and they span the same Hilbert space as the Bloch functions. The matrix elements for the Hamiltonian in the Wannier basis can be written as

$$H_{mn}(R) = \langle W_{mk} | H | W_{nk} \rangle \tag{2.31}$$

Once the real space hopping elements are known, The k-space Hamiltonian can be obtained as follows-

$$H_{mn}(K) = \sum_R e^{ik.R} H_{mn}(R), \tag{2.32}$$

or,

$$H_{mn}(K) = \sum_R e^{ik.(\vec{R}+\vec{\tau}_m-\vec{\tau}_n)} H_{mn}(\vec{R}) \tag{2.33}$$

where τ_n represents the location of the nth Wannier orbital in the unit cell. The eigenvalues of the different approach in Eq. 2.32 and 2.33 are same but their eigenvectors are different. The Eq. 2.32 consist only Bloch wave function Ψ_{nk}, while 2.33 also includes the periodic part of the Bloch wavefunction $u_{nk}(\vec{r}) =_{nk} (e^{-ik.\vec{r}})$ [77]. The formalism in Eq. 2.33 is more accurate in the context of topological materials due its relation with Berry phase and Berry curvature.

This Wannier base method is very useful to calculate various properties. For example, the Berry phase of the system can be calculated using the matrix element of the position operator in the following way-

$$\bar{\mathbf{r}}_n = \langle \omega_{n0} | \vec{r} | \omega_n \rangle = \frac{V_{cell}}{(2\pi)^3} \int_{BZ} \langle u_{nk} | i \nabla_k u_{nk} \rangle d^3\vec{k} \tag{2.34}$$

In one dimension, we have

$$\bar{x}_n = \frac{a}{2\pi} \int_0^{2\pi} \langle u_{nk} | i \delta_k u_{nk} \rangle d\vec{k}, \tag{2.35}$$

or,

$$\bar{x}_n = a \frac{\phi_n}{2\pi} \tag{2.36}$$

Here, ϕ_n is the Berry phase and a denotes the cell parameter of the one-dimensional lattice. Therefore, the information about the Berry phase can be easily obtained by tracking the Wannier charge centers. Other important aspects of the Wannier function based Hamiltonian are the calculations of topological invariant, topological protected edge or surface states and calculation of different conductivity such as Anomalous Hall conductivity (AHC) and Spin Hall conductivity (SHC) using the wannier90 code.

ARTICLES COMPOSING THE THESIS WITH SUMMARIES

3.1   A brief overview of the main results

During my last four year of my Ph.D. journey, I have been exploring different materials and their exotic quantum phases which could be useful for quantum technologies and quantum communication.

In our group Alexander Lau e.t al shows (in Physical Review X 11 (3), 031017) [96], the 3D flat band could be achieve by applying strain on 3D materials n a iso-energetic nodal line semimetal. Taking consideration of experimental perspective of Magtop and real material candidate for 3D flat band, I have constructed a 3D superlatice of HgTe-based chalcogenides. I have constructed the 3D supper lattice of (i) HgTe/CdTe(topological insulator/normal insulator) (ii) HgTe/HgSe (topological insulator/topological insulator). I have observe a isoenergic nodal line semimetal in HgTe/CdTe 3D superlattice, it is a good material platform for the 3D flat band superconductivity. Beyond the 3D flat band super conductivity, I have observe the Weyl semi metal phase when we have construct a 3D superlattice of two topological HgTe/MnTe. The correlation of the materials change crystal field, which give rise to plethora of exotic topological phase in thge 3D superlattice of HgTe-based chalcogenides.

Along with the 3D superlatice of HgTe-based materials, I have demonstrate a new quantum phases in new 2D materials which grown in 2019 as a monolayer without knowing the counter part of bulk. I have observe in quantum phenomena such as spin-valley effect in the 2H phase of monolayer of MSi_2Z_4 (M= Mo,W and Z= N,P, As) that means the opposite valley K and K$'$ has opposite spin locking due to symmetries. The spin polarization vanishes at K and K$'$ in the bilayer of the MSi_2Z_4 materials. We also discuss the tunability of these states by applying electric field which is a crucial aspect of a valleytronic transistor. I also predicted a new phase 1T$'$ of

MSi_2Z_4 (M= Mo,W and Z= N,P, As) are thermodynamically stable. The few of the 1T'- MSi_2Z_4 Materials are a large gap quantum spin Hall insulator. It shows topological to normal insulator transition under the influence of external electric field. This materials could be a good candidate for quantum spin Hall transistor like $1T'MoS_2$ as proposed by Liang Fu et.al[97].

3.2 PAPER I :Topological states in superlattices of HgTe-class materials

New topological phases have been engineered using the superlattices. A superlattice composed of magnetically doped transition metal dichalcogenides (TIs) and normal insulators is one of the first generic examples of a material that can induce a WSM phase. The Zinc-blende superlattices comprising of HgTe, HgSe, and CdTe provide a suitable material platform for the search for topological phases in other superlattices. Unlike the trivial insulator CdTe, the bulk semiconductors HgTe and HgSe have a band inversion that may be adjusted by varying thickness, strain, and temperature [98–100]. In systems made of these materials, topological phases like the topological insulator (TI) phase, the Weyl semimetal (WSM) phase, and the quantum spin Hall phase may appear.

In this work, we use ab initio calculations to show that (001) HgTe/CdTe and HgTe/HgSe superlattices show a wide range of topological phases, including phases with isoenergetic nodal lines at the Fermi energy of the unstrained structures. We have constructed (3ML)HgTe/(3ML)CdTe 3D SLs along (001) direction. The band structure of CdTe/HgTe shows few meV gap along high symmetry directions with camel-back like feature along $\Gamma \rightarrow Z$ direction. I have observed a band multiple band crossing points far from the high-symmetry direction. By constructing a Tight-binding model, I have found multiple nodal points at the Fermi level create nodal ring. Finally, the presence of topological surface state that connects nodes identified as a isoenergic nodal line semimetal. The strain and hydrostatic pressure leads to a normal insulating phase in (001) HgTe/CdTe 3D SLs. Moreover, I have studied (3ML)HgTe/(3ML)HgSe 3D SLs along (001). It is discovered to be an ideal Weyl semimetal. It depicts eight Weyl's points, four of which are on the $k_z=+k_z$ plane and other four Weyl points are on the $k_z=-k_z$ plane. The Fermi-arc of the material confirms the claim by connecting the opposite chirality; the Berry of the material is consistent with the Fermi-arc results; the chirality +ve acts as a source, and the chirality -ve acts as a shrink. This weyl phase in HgTe/HgSe 3d SLs is robust against hydrostatic pressure, but it starts coming closer to each other with hydrostatic pressure, and at a critical pressure it merges and form a Dirac semimetal phase and becomes a Weyls semimetal with a topological Lifshitz transition. The weyl phase, on the other hand, is influenced by uniaxial compression or strain, and the interaction between the crystal field effect and spin-orbit coupling results in a phase transition from the nodal line to a topological insulator phase.

Topological states in superlattices of HgTe class of materials for engineering three-dimensional flat bands

Rajibul Islam [1,*] Barun Ghosh,[2,3] Giuseppe Cuono [1] Alexander Lau [1] Wojciech Brzezicki [4,1] Arun Bansil,[2]
Amit Agarwal,[3] Bahadur Singh [5,†] Tomasz Dietl [1,6] and Carmine Autieri [1,7,‡]

[1]*International Research Centre MagTop, Institute of Physics, Polish Academy of Sciences, Aleja Lotników 32/46, PL-02668 Warsaw, Poland*
[2]*Department of Physics, Northeastern University, Boston, Massachusetts 02115, USA*
[3]*Department of Physics, Indian Institute of Technology, Kanpur 208016, India*
[4]*Institute of Theoretical Physics, Jagiellonian University, ulica S. Łojasiewicza 11, PL-30348 Kraków, Poland*
[5]*Department of Condensed Matter Physics and Materials Science, Tata Institute of Fundamental Research, Colaba, Mumbai 400005, India*
[6]*WPI-Advanced Institute for Materials Research, Tohoku University, Sendai 980-8577, Japan*
[7]*Consiglio Nazionale delle Ricerche CNR-SPIN, UOS Salerno, IT-84084 Fisciano (Salerno), Italy*

In search of materials with three-dimensional flat band dispersions, using *ab initio* computations we investigate how topological phases evolve as a function of hydrostatic pressure and uniaxial strain in two types of superlattices: HgTe/CdTe and HgTe/HgSe. In short-period HgTe/CdTe superlattices, our analysis unveils the presence of isoenergetic nodal lines, which could host strain-induced three-dimensional flat bands at the Fermi level without requiring doping, when fabricated, for instance, as core-shell nanowires. In contrast, HgTe/HgSe short-period superlattices are found to harbor a rich phase diagram with a plethora of topological phases. Notably, the unstrained superlattice realizes an ideal Weyl semimetal with Weyl points situated at the Fermi level. A small-gap topological insulator with multiple band inversions can be obtained by tuning the volume: under compressive uniaxial strain, the material transitions sequentially into a Dirac semimetal to a nodal-line semimetal, and finally into a topological insulator with a single band inversion.

I. INTRODUCTION

In the past decades, tremendous effort has been made both theoretically and experimentally to search, predict, and understand the characteristics of a wide variety of topological phases, such as topological insulators (TIs) [1–7], topological crystalline insulators (TCIs) [8–11], Dirac semimetals (DSMs) [12–15], Weyl semimetals (WSMs) [16–19], and nodal-line semimetals (NLSMs) [20–24]. TIs and TCIs are bulk insulators whose nontrivial band topology, enabled by band inversions, gives rise to conducting surface states and quantized physical observables. WSMs and DSMs are three-dimensional (3D) semimetals with linear band-crossing points near the Fermi level, the so-called Weyl and Dirac points, respectively. Weyl points are inherently stable due to a quantized topological charge or chirality, which requires the breaking of inversion or time-reversal symmetry, whereas the Dirac points can only be stabilized by enforcing additional spatial symmetries in time-reversal and inversion symmetric environments. One of their hallmarks is the presence of conducting surface states that form open Fermi arcs connecting the bulk nodal points on the surface of the material. In NLSMs, the nodal points form closed loops in the bulk Brillouin zone (BZ) giving rise to characteristic drumhead states on their surfaces. Typically, topological semimetals, such as WSMs and NLSMs, appear as intermediate phases between two topologically distinct insulating phases. The breaking of the time-reversal symmetry by introducing magnetism leads to a new variety of topological phases like the quantum anomalous Hall (QAH) phase [25–27] and the axion-insulator phase [28–31].

Another appealing research direction concerns designing materials with carriers residing in flat bands which can support new correlation-driven collective phases. A comprehensive catalog of compounds with flat bands near the Fermi energy has recently been completed [32]. In the case of metals, the familiar Mott-Hubbard physics is expected. In nonmetallic compounds, a key challenge is how to introduce carriers avoiding the Anderson-Mott metal-to-insulator transition, as the role of localization increases when the kinetic energy of the carriers is reduced. In 2D systems, modulation doping or gating introduces carriers without enhancing disorder, the case of flat bands in twisted 2D flakes [33]. Some of the present authors have recently demonstrated theoretically that 3D flat bands are expected in systems exhibiting isoenergetic nodal lines under the presence of inhomogeneous strain [34]. The

---

latter plays the role of a gauge potential quantizing the carrier spectrum into Landau-like levels in the absence of an external magnetic field. Rhombohedral graphite and the CaAgP-class of compounds have been pushed forward as candidate materials. However, in view of the experimental realization and study of 3D flat bands, it is paramount to find more material systems with suitable properties, especially with the presence of nodal lines.

Superlattices have been used to engineer new topological phases. One of the first general examples is a superlattice made of alternating layers of magnetically doped TIs and normal insulators to trigger the appearance of a WSM phase [35]. Looking for topological phases in other types of superlattices, a promising material platform constitutes zinc-blende heterostructures of HgTe, HgSe, and CdTe. While CdTe is a trivial insulator, bulk HgTe and HgSe are symmetry-enforced zero-bandgap semiconductors with a band inversion, which can be tuned by changing thickness, strain, and temperature [3,36–39]. The systems made up of these materials may give rise to several different topological phases, such as a TI phase [40,41], a WSM phase [42], or a quantum spin Hall phase in insulating 2D HgTe/CdTe quantum wells [2,3,43]. In the case of magnetic Mn doping, the k dependence of the sp-d hybridization has to be taken into account to describe accurately the exchange-induced splitting of magneto-optical spectra corresponding to electron-hole excitations in various points of the BZ [44]. Despite the inverted band structure, coupling between Mn spins is dominated by superexchange [45] rather than by interband spin polarization [26]. It has theoretically been predicted [25] that the breaking of time-reversal symmetry by magnetic doping would lead to a QAH phase. However, this has not yet been observed experimentally in HgTe-based TIs.

In this paper, we demonstrate by *ab initio* computations that (001) HgTe/CdTe and HgTe/HgSe superlattices show a rich tapestry of topological phases including phases with isoenergetic nodal lines residing at the Fermi energy of the unstrained structures. The two cases investigated here are representative of the combination of trivial/topological and topological/topological superlattices.

The paper is structured as follows. In Sec. II, we discuss the band structure and symmetry properties of bulk HgTe, of bulk CdTe, of bulk HgSe, and their superlattices. The computational details and the numerical values of the band structure parameters are described in Appendixes A and B. Section III, discusses the nodal-line semimetal phase obtained in unstrained HgTe/CdTe superlattices. In Sec. IV, we continue by presenting an ideal Weyl semimetal phase in the related HgTe/HgSe short-period superlattices, before studying the effect of hydrostatic pressure and uniaxial strain on this heterostructure in Sec. V. Notably, the latter reveals another nodal-line semimetal phase. Finally, Sec. VI summarizes our results and provides a brief outlook on possible research directions.

II. SYMMETRIES AND STRUCTURAL PROPERTIES

A. Bulk

CdTe, HgTe, and HgSe belong to the space group $F\bar{4}3m$, No. 216. They have T_d symmetry with mirror planes along the
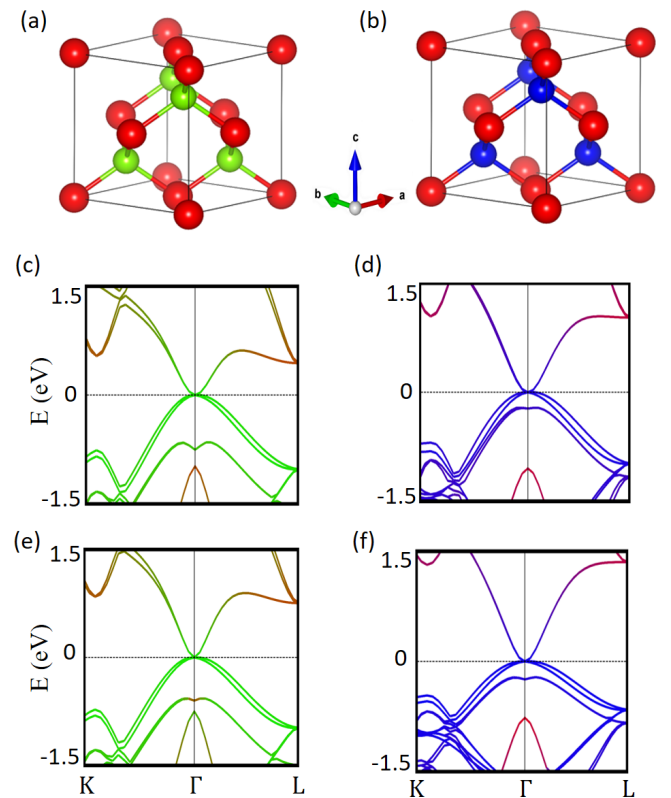

FIG. 1. [(a) and (b)] Crystal structure of bulk HgTe and HgSe in the conventional unit cell. Hg, Te and Se atoms are highlighted in red, green and blue, respectively. [(c) and (d)] Band structure within GGA and [(e) and (f)] within the MBJGGA approach of bulk HgTe and HgSe, respectively. Red, green, and blue lines represent the Hg, Te, and Se band characters, respectively.

(110), (101), and (011) directions. The conventional unit cell contains eight atoms: four cations and four anions as shown in Figs. 1(a) and 1(b). The Rashba-Dresselhaus effect is present in the zinc-blende structure because of the lack of inversion symmetry [46].

The band structure of bulk HgTe and HgSe [Figs. 1(c)–1(f)] exhibits an inverted band ordering, dictating that HgTe and HgSe materials exhibit a nontrivial topological character [2,47,48]. The band inversion takes place between cation-s and anion-p bands at the Fermi level driven by two relativistic effects: on the one hand, the mass-velocity term that lowers significantly the energy of the s orbitals in heavy cations and, on the other hand, spin-orbit coupling (SOC) shifting up the anion p orbitals with total angular momentum $j = 3/2$ [49].

The spin-orbit interaction of the anions (Se, Te) plays an important role in the band topology. The SOC splits the bands near the Fermi level into fourfold-degenerate $j = 3/2$ and twofold-degenerate $j = 1/2$ bands at the Γ point. According to the symmetry of the wave function, the anion p bands are labeled as Γ_8 ($j = 3/2$) and Γ_7 ($j = 1/2$), while the cation s bands are labeled as Γ_6 at the Γ point. Figures 1(c) and 1(d) shows the band structure using the generalized gradient approximation (GGA) [50]. To reproduce the correct experimental band ordering for both HgTe and HgSe, we have further obtained band structure using the

modified Becke-Johnson exchange potential together with the correlation potential scheme (MBJGGA) (see Appendix A for details). The results are shown in Figs. 1(e) and 1(f). This yields the order of energy levels at Γ in qualitative agreement with experiments. Notably, while the band ordering between Γ_6 and Γ_7 in GGA differs from experiments, the higher-lying p bands close to the Fermi level, which are relevant for the topology, are correctly obtained by both functionals. We thus resort to the GGA exchange-correlation functional to describe the topological properties of the systems in this paper.

Both HgTe and HgSe are symmetry-enforced zero-band-gap semiconductors due to the interplay between the spin-orbit splitting in the p-orbital manifold, their bulk cubic symmetry and the mass-velocity term of Hg [49]. Indeed, at the Γ point, the p orbitals split under the spin-orbit interaction into Γ_8 (fourfold degenerate) and Γ_7 (doubly degenerate) states. The remaining degeneracies are protected as long as the cubic symmetry is present. The Fermi level lies at the Γ_8 energy level producing a zero-band-gap semiconductor. The cubic symmetry is preserved in the presence of hydrostatic pressure but it is broken in case of anisotropic strain and interface heterostructures. Once the cubic symmetry is broken, the fourfold degenerate state splits thereby removing the zero-gap semiconductor state but keeping the band inversion so that other topological phases can evolve. Additionally, the breaking of the crystal symmetry produces also the characteristic camel-back feature of the band structure. Defining the magnitude of the band inversion as $E_g = E_p - E_s$, we have found that the band inversion strongly depends on the volume through the crystal field effect: by compressing the volume, E_s increases more than E_p because the s-orbital of the Hg atoms is isotropic and is, therefore, strongly affected by the crystal field of the four Te (Se) atoms. As a consequence, a compression of the volume reduces E_g thereby pushing the system towards the trivial insulating phase.

B. Superlattice

The interface between two materials couples different degrees of freedom giving rise to emergent phases such as 2D electron gases, superconductivity, proximity effects [51–53], exotic exchange bias [54,55], anisotropic metal-insulator transitions [56], or a sign-tunable anomalous Hall effect [57]. In particular, the interfaces between zinc-blende compounds and their superlattices have been intensively studied to generate new electronic and topological phases [58,59].

We study short-period HgTe/CdTe and HgTe/HgSe superlattices and reveal the emergence of various topological phases. For the sake of brevity, we only discuss the structure and symmetry properties of HgTe/HgSe, but the same statements are valid also for HgTe/CdTe. The 3D superlattice of HgTe/HgSe represents a heterostructure composed of alternating phases of two dissimilar topological semimetals. We consider the case with the same number n of layers for both phases. (The short-period superlattices with a small value of n are considered because long-period superlattices are expected to recover the properties and phases of bulk HgTe.) We further have to distinguish between even and odd values of n in the $(\text{HgTe})_n/(\text{HgSe})_n$ heterostructures. For n even, the directions (110) and $(\bar{1}10)$ are equivalent. On the contrary, for an odd
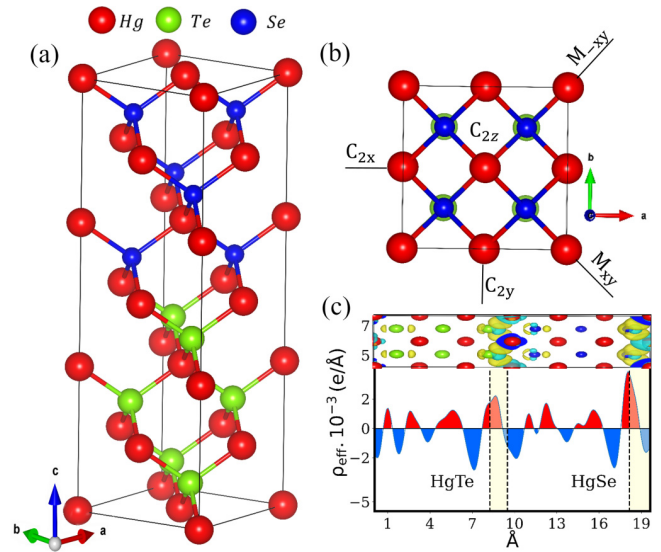

FIG. 2. (a) 3D HgTe/HgSe superlattice constructed along the (001) direction. (b) Top view of the crystal structure with symmetries present in the heterostructure indicated. (c) Isosurface of the charge difference in real space (top) and linear charge difference $\rho(z)$ (bottom). We have labeled the HgTe and HgSe regions, the dashed vertical lines represent the interface layers between HgTe and HgSe.

number of layers the (110) and $(\bar{1}10)$ directions become equivalent.

We expect that the interplay between the breaking of the crystal symmetries and the full spin-orbit coupling favors a rich topological phase diagram. To break the crystal symmetries, we have constructed the superlattice by alternating three layers of HgTe and of HgSe, i.e., $(\text{HgTe})_3/(\text{HgSe})_3$, along the (001) direction. The heterostructure comprises three conventional zinc-blende unit cells along the c axis and, therefore, we assume for the out-of-plane lattice constant of the supercell $c_{\text{SL}} = 3a_{\text{SL}}$, where a_{SL} is the in-plane lattice constant. As in the bulk, each anion (cation) is tetrahedrally coordinated by four nearest-neighbor cations (anions). When cutting through the structure along the z direction, one finds subsequent layers of one atomic thickness consisting of only anions and only cations, respectively [see Fig. 2(a)]. The six cationic layers are composed of Hg atoms, while there are three anionic layers containing Te and three anionic layers containing Se in each superlattice period. Both compounds have the same zinc-blende space group, but in the heterostructure with an odd number of layers the directions (110) and $(\bar{1}10)$ are now inequivalent. This results in a lower symmetry which could favor the possibility of Weyl and nodal-line phases [60]. Moreover, the interface between zinc-blende materials can be used to manipulate the band gap and, therefore, the topological properties of the whole heterostructure. We will show that these 3D superlattices have electronic properties similar to the HgTe class of materials under strain [42], since they preserve the C_2 symmetry. However, the different periodicity along the z axis lends the superlattices a tetragonal symmetry.

Our heterostructure belongs to the space group $P\bar{4}m2$ (D_{2d}), No. 115, which is a body-centered tetragonal crystal structure with lattice parameters a_{SL} and c_{SL}. By design, the

point-group symmetry of the heterostructure is reduced from T_d to D_{2d} with respect to the bulk compounds. Bulk HgTe and bulk HgSe have lattice constants $a_{\text{HgTe}} = 6.46$ Å and $a_{\text{HgSe}} = 6.09$ Å, respectively. The in-plane lattice constant of the supercell depends on the lattice constants of the constituent compounds following Vegard's law. Without strain, we assume the in-plane lattice constant of the supercell to be $a_{\text{SL}} = 6.27$ Å, which is the rounded average between the experimental HgTe and HgSe lattice constants and therefore expected to be close to the experimental value for this superlattice.

The heterostructure has three twofold rotational symmetries along the x, y and z directions (C_{2x}, C_{2y}, and C_{2z}), and two mirror symmetries (M_{xy} and $M_{x\bar{y}}$), as shown in Fig. 2(b). Similar to bulk HgTe, the $(\text{HgTe})_3/(\text{HgSe})_3$ heterostructure lacks inversion symmetry. Nevertheless, it preserves time-reversal symmetry. Notably, the symmetry properties of the heterostructure are similar to strained HgTe [42] and some chalcopyrites [61,62]. The presence of time-reversal symmetry together with the mirror symmetries and the C_{2z} symmetry give rise to doubly degenerate bands along the Γ-Z direction, so-called Kramers nodal lines [63], while the band structure has nondegenerate bands along all other directions as discussed below. This implies a constraint on the topology of the Fermi surfaces similar to the effect of nonsymmorphic symmetries [64].

Interfaces between two materials generally give rise to a charge transfer between the layers. To assess this effect, we define the linear charge density $\rho(z)$ as the number of electrons summed over the xy plane per unit length such that $\int \rho(z)dz$ is equal to the number of electrons. We have performed density functional theory calculations for the entire heterostructure and for separate slabs containing only HgTe and only HgSe with the same geometry as the heterostructure. Subsequently, we have considered the difference between the respective linear charge densities:

$$\Delta\rho(z) = \rho_{\text{HgTe/HgSe}}(z) - \rho_{\text{HgTe}}(z) - \rho_{\text{HgSe}}(z). \quad (1)$$

The integral of this quantity is zero by construction. We find that a negligible amount of charge on the order of 10^{-3} electrons is accumulated near the interfaces as shown in Fig. 2(c). These results infer that there is no significant charge transfer between HgTe and HgSe in the 3D superlattice. This confirms our expectations as the two compounds have similar electronegativities. In the HgTe/HgSe heterostructure there is one kind of interface, namely Te/Hg/Se. However, the heterostructure can be cut in two regions in different ways. We cut the heterostructure in two different ways at Te/Hg and Hg/Se. For this reason, we note that there is a slight asymmetry between the two interfaces as seen in Fig. 2(c). These results clearly demonstrate that there is no considerable charge transfer at the interface.

In the following sections, we show the appearance of a nodal-line semimetal phase in short-period superlattices of HgTe/CdTe and of an ideal Weyl semimetal phase in HgTe/HgSe superlattices. Moreover, we will investigate the latter under hydrostatic and uniaxial pressure.
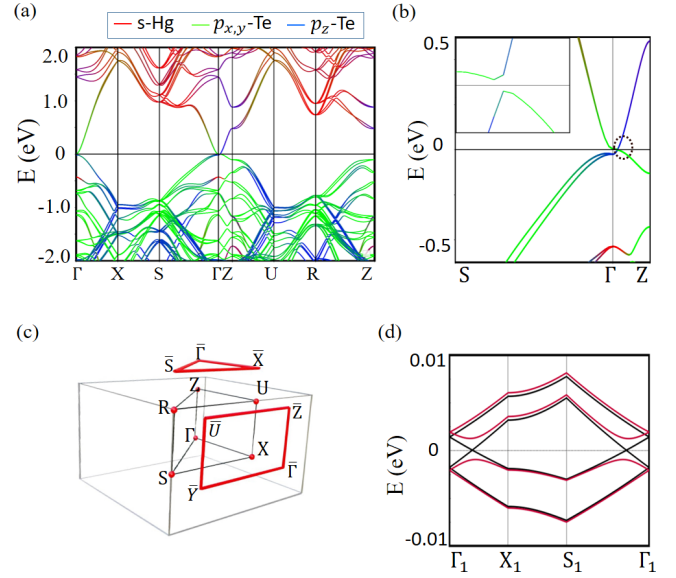

FIG. 3. (a) Orbital-resolved band structure of $(\text{HgTe})_3/(\text{CdTe})_3$ superlattice in the full Brillouin zone (BZ) and (b) enlarged view along the S-Γ-Z high-symmetry path. The inset shows that the system is gapped along the Γ-Z direction. (c) Schematic diagram of the full BZ (black solid lines) with (100) and (001) BZ surface projections (red solid lines). (d) Band structure with nodal points at $k_z = 0.020$ Å^{-1}(black) and gapped at $k_z = 0.021$ Å^{-1}(red). These four bands are a set of bands isolated from the rest of the band structure.

III. NODAL-LINE SEMIMETAL IN HgTe/CdTe SUPERLATTICES

We now discuss the band structure and the Fermi surface of the unstrained $(\text{HgTe})_3/(\text{CdTe})_3$ superlattice. This superlattice is feasible experimentally due to the presence of only one type of chalcogen atoms as assessed in the earlier quantum well experiments. Figure 3(a) shows the band structure along high-symmetry lines of the full BZ. At the Γ point, the s band of Hg is at -0.5 eV with respect to the Fermi level, which is similar to bulk HgTe. The bands close to the Fermi level are dominated by the p orbitals of the Te atoms. An enlarged view of the band structure along the S-Γ-Z high-symmetry path in Fig. 3(b) reveals a band inversion between the $|j, j_z\rangle = |3/2, \pm1/2\rangle$ bands and the $|j, j_z\rangle = |3/2, \pm3/2\rangle$ bands of the Te atoms. Looking at the orbital weight of these bands, we find that $|3/2, \pm3/2\rangle$ are made up only of p_x and p_y orbitals, while $|3/2, \pm1/2\rangle$ contain one third of in-plane orbitals and two thirds of p_z. We make similar observations for the other type of superlattice considered in this article (see below). While the band structure is gapped along the Γ-Z direction, we find that the system features two isoenergetic, circular nodal lines with the same radius in planes parallel to the k_x-k_y plane at $k_z^* = \pm0.02$ Å^{-1}. Figure 3(d) shows the corresponding bands along two paths of the form $\Gamma_1 = (0, 0, k_z) \rightarrow X_1 = (0.005\frac{\pi}{a}, 0, k_z) \rightarrow S_1 = (0.005\frac{\pi}{a}, 0.005\frac{\pi}{b}, k_z) \rightarrow \Gamma_1$, one with $k_z = k_z^*$ crossing one of the nodal lines and one with $k_z = 1.05\,k_z^*$. Remarkably, the nodal lines are isoenergetic with lack of energy dispersion and lie at the Fermi level.
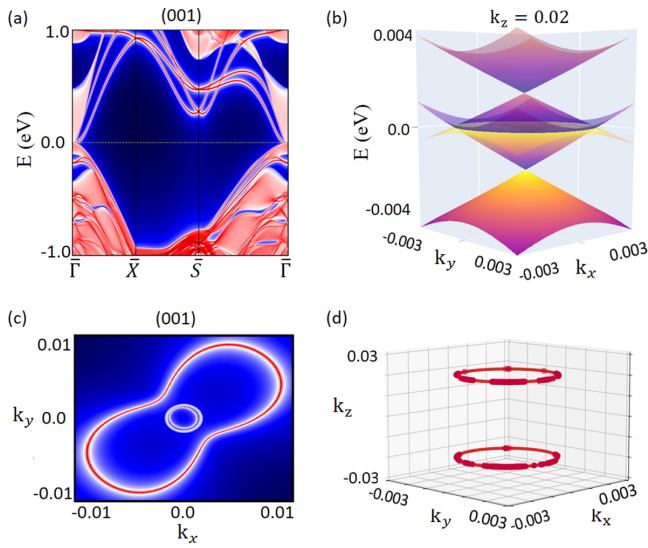
FIG. 4. (a) Surface band structure and (c) associated Fermi band contours of (001) Te-terminated surface of $(HgTe)_3/(CdTe)_3$ super-lattice. (b) Band structure of the infinite superlattice in the $E - k_x - k_y$ space at a fixed $k_z = 0.02$ Å^{-1}. (d) Nodal lines of the infinite superlattice resolved at the $k_z = \pm 0.02$ Å^{-1} planes. The units are in Å^{-1} in this and in the next figures regarding the **k**-space.

Figure 4(a) shows the surface band structure with Te-terminated (001) surface. The associated Fermi contours has two circular features close to $\bar{\Gamma}$, as shown in Fig. 4(c), one of which corresponds to the projection of the bulk nodal lines into the surface BZ. The other circular feature together with a larger bow-tie shaped Fermi line are made up of surface states. In Fig. 4(b), we present the superlattice band structure at fixed $k_z = k_z^* = 0.02$ Å^{-1}, where the circular nodal line is visible at the Fermi level. The Fermi surface of the superlattice is shown in Fig. 4(d) consisting of two circular lines located on the $k_z = \pm k_z^* = \pm 0.02$ Å^{-1} planes. The superlattice of HgTe/CdTe thus realizes a nodal-line semimetal phase.

The presence of these nodal lines can be understood from looking at bulk HgTe. Away from the Fermi level, bulk HgTe features a network of bow-tie shaped nodal lines protected by six symmetry-related mirror planes [65]. The application of uniaxial strain along the c-axis breaks all mirror symmetries except M_{xy} and $M_{x\bar{y}}$. Consequently, all nodal lines except the ones in the two remaining mirror planes are gapped out. However, the latter gradually shrink to points and gap out already for small strain. Finally, the only remaining features are eight C_2T symmetry-protected point nodes in the x-z and y-z planes, which are located along their intersections with the broken mirror planes. In particular, they lie on some of the previous but no longer protected nodal lines. In our heterostructure, the role of the external strain is played by the interface between the two dissimilar materials leading to a similar picture. Remarkably, the band structure parameters of the short-range superlattice with trivial CdTe lead to a situation where the nodal lines containing the C_2T protected point nodes survive and move to the Fermi level. Notably, while these nodal lines are not symmetry protected, the gap opened at the crossings points are negligible and beyond our computational resolution. This situation is comparable to
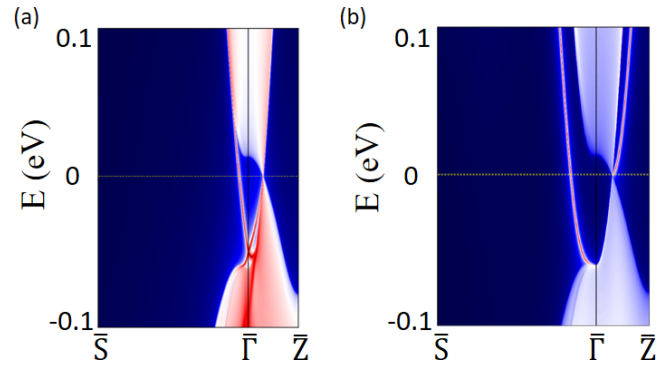

FIG. 5. Band structure of the slab with (100) orientation for the (a) Hg-terminated and (b) Te-terminated surfaces.

many 3D Dirac semimetal materials. These states lie close to the Fermi level, forming almost dispersionless flat bands as seen in Fig. 4(d).

We note that we find a pair of nodal lines also in the $(HgTe)_4/(CdTe)_4$ superlattice (see Appendix C) despite the different symmetries. However, the nodal lines tend to shrink as we increase the of the superlattice. We also note that in 2D quantum wells there is a critical thickness for the topological phase of HgTe. However, in the case of the superlattice we expect this critical thickness to be shorter due to the repetition of HgTe. Finally, we find that the considered HgTe/CdTe superlattice becomes a trivial insulator when applying compressive hydrostatic pressure.

IV. IDEAL WEYL SEMIMETAL IN HgTe/HgSe SUPERLATTICES

We now consider the unstrained HgTe/HgSe superlattice. We find that the details of the surface states depend on the type of surface termination. Figures 5(a) and 5(b) show the surface band structure of the Hg- and Te-terminated surfaces, respectively. We observe surface states connecting the valence and the conduction bands indicating the topological nature of the system. For the Hg-termination, the surface Dirac point is at 0.06 eV below the Fermi level. On the contrary, the Dirac point is buried in the bulk bands for the Te-termination of the slab with (100) orientation. For the sake of brevity, we consider chalcogen atomic terminations to present our following results.

Figure 6(a) displays the band structure of the infinite superlattice along the high-symmetry lines S-Γ-Z close to the Fermi level. It constitutes an inverted band gap of 13.1 meV on the Γ-Z line. A careful exploration of states near the band anticrossing points reveals linear band crossing typical of Weyl semimetals along the path X_1-Γ_1-Y_1, as shown in Fig. 6(b). We define $\Gamma_1 = (0, 0, k_z^*)$, $X_1 = (0.1\pi/a, 0, k_z^*)$ and $Y_1 = (0, 0.1\pi/a, k_z^*)$, with $k_z^* = 0.0506$ Å^{-1}. We find a total of eight symmetry related Weyl points constrained by the presence of $C_{2x}T$ and $C_{2y}T$ symmetries with respect to the planes at $k_x = 0$ and $k_y = 0$ [60]. Their positions in the BZ are $(0, \pm k_\parallel^*, \pm k_z^*)$ for the four Weyl points with chirality $+1$ and $(\pm k_\parallel^*, 0, \pm k_z^*)$ for the other four with chirality -1, where we have defined $k_\parallel^* = 0.0077$ Å^{-1}. Interestingly, these Weyl
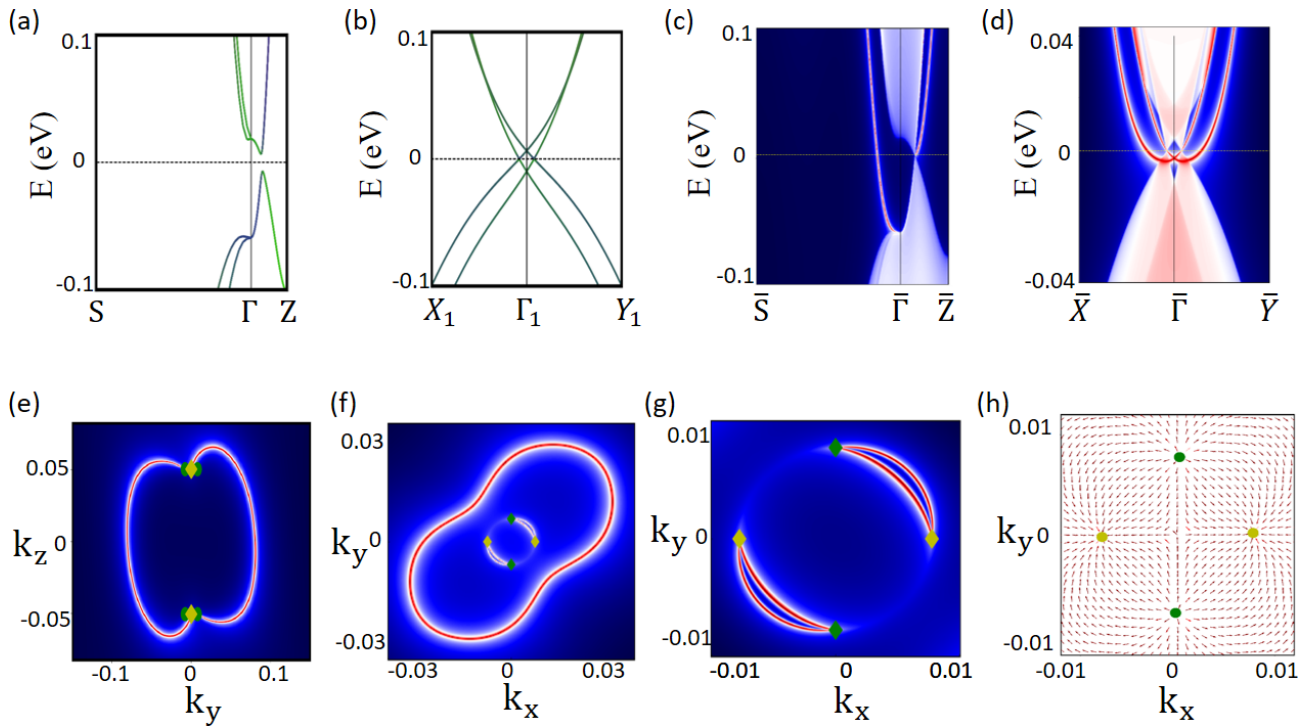
FIG. 6. Band structure of the unstrained HgTe/HgSe infinite superlattice (a) along the high-symmetry lines S-Γ-Z. (b) Band structure in the plane of the Weyl points at $k_z = k_z^* = 0.0506$ Å^{-1}. Band structure of slabs with (c) (100) surfaces and (d) (001) surfaces. Fermi surfaces of the slabs with (e) (100) surfaces and (f) (001) surfaces. (g) Magnification of panel (f) close to $\bar{\Gamma}$. (h) In-plane component of the Berry flux at the $k_z = k_z^*$ plane containing four Weyl points. The Weyl points at $(\pm k_\parallel^*, 0, \pm k_z^*)$ have chirality -1 (yellow circle marker) while the Weyl points at $(0, \pm k_\parallel^*, \pm k_z^*)$ have chirality $+1$ (green circle marker). Diamond markers indicate chirality -2 (yellow) and $+2$ (green).

nodes appear at the Fermi level, showing that the superlattice structure realizes ideal Weyl semimetal phase in their pristine state in contrast to HgTe [42].

The orbital-resolved band structure further reveals that the p-bands of Se and Te dominate near the Fermi level. In addition to the band inversion present in bulk HgTe and HgSe, also in this superlattice we find a new band inversion between $|3/2, \pm 3/2\rangle$-Se and $|3/2, \pm 1/2\rangle$-Te orbitals at the Γ point, which is essential for the creation of the Weyl phase. The system thus has multiple band inversions at the Γ point. The symmetry is reduced to D$_{2d}$ due to the interface. In general, the symmetry reduction creates a camel-back-shaped band in the valence bands and an inverse camel-back structure in the conduction bands along the Γ-Z high-symmetry line. The same camel-back feature has been found for bulk HgTe in the presence of doping or strain, which also breaks the bulk symmetry.

A material with inversion and time-reversal symmetry would have doubly degenerate bands due to Kramers's degeneracies. The splitting between the spin-orbit split bands gives a measure of the bulk inversion asymmetry (BIA) [60]. To create Weyl points in HgTe materials class, both BIA and symmetry reduction to D$_{2d}$ are needed. The parameter α governing the first-order term in **k** of the BIA has been estimated to be small in HgTe ($\alpha = 0.208$ Å eV) [60]. Due to the small value of $k_\parallel^*$, the third-order term in **k** can be neglected. For the considered superlattice, the spin-orbit split bands reported in

Fig. 6(b) cross each other in the conduction band. Curiously, at this crossing point, the BIA is accidentally zero. Later, this observation will serve useful in understanding the progression of topological phases under applied external strain.

One of the hallmarks of WSMs is the presence of topologically protected Fermi arcs on the surface of the material. To confirm the topological nature of the 3D superlattices, we have calculated the surface electronic states and Fermi arcs for the (100) and (001) surface orientations, using the surface notation of the conventional unit cell as shown in Fig. 2(a). The (010) surface is equivalent to the (100) surface.

The band structure of the slab for the (100) surface orientation along high-symmetry lines is shown in Fig. 6(c). We find surface states connecting the valence and the conduction bands confirming the topological nature of the system. Moreover, we observe a gapless point at the coordinates $(0, k_z^*)$ corresponding to Weyl points projected into the 2D BZ of the slab. The Fermi surface for the slab with surface orientation (100) is shown in Fig. 6(e). It has six gapless points, four points with projected coordinates $(\pm k_\parallel^*, \pm k_z^*)$ and monopole charge $+1$ and two points with coordinates $(0, \pm k_z^*)$ and monopole charge -2. The latter is the result of two Weyl points of charge -1 being projected onto the same point in the surface BZ. We observe two large Fermi arcs connecting each one of the -2 monopole charges with one of the -1 monopole charges. The other two short Fermi arcs, which are expected to be present between the monopole charges with

-2 and the remaining two monopole charges with -1, are not clearly resolved due to the small distances between the Weyl points for this surface orientation.

The band structure for the slab with (001) surface orientation along high-symmetry lines is shown in Fig. 6(d) featuring two gapless points. We also present the corresponding Fermi surface and its magnification around the Weyl-point projections in Figs. 6(f) and 6(g), respectively. The Weyl points with monopole charge $+1$ are pairwise projected to the points $(0, \pm k_\parallel{}^*)$, while the Weyl points with monopole charge of -1 are pairwise projected to $(\pm k_\parallel{}^*, 0)$. The resulting four nodal points have an effective monopole charge of ± 2 giving rise to two Fermi lines emanating from each of them. In this way, they form four open Fermi arcs between them giving rise to two separate intraconnected pairs of Weyl nodes. We also observe one large closed Fermi line encompassing the surface projections of the Weyl points around $\bar{\Gamma}$. Notably, this Fermi line is disconnected from the Weyl points and originates from the vicinity to a topological insulator phase that would form after pairwise annihilation of the Weyl points. The remnant surface Dirac cone can be viewed as coming from the bulk band inversion, while the band-inversion generated by the p orbitals produces the Weyl points. The resulting coexistence of Dirac cone and Weyl points has been described in the literature [66]. Furthermore, we have calculated the Berry flux in the $k_z = k_z^*$ planes containing the Weyl points. The projections of the Berry flux into the x-y plane are visualized in Fig. 6(h). We see how the Weyl points with chirality $+1$ act as sources of Berry flux while the Weyl points with chirality -1 act as sinks. The Weyl points of opposite chirality are well separated by an in-plane distance of 1.5% of the reciprocal lattice constant. Since there are no trivial states at the Weyl nodes' energy, the Weyl phase in this 3D multilayer superlattice could be unambiguously detected experimentally.

V. HYDROSTATIC PRESSURE AND UNIAXIAL STRAIN IN HgTe/HgSe SUPERLATTICES

A. Topological properties as a function of hydrostatic pressure

We present the computational results on the evolution of topological phases in the HgTe/HgSe superlattices with applied hydrostatic pressure. In particular, we have performed calculations for different volumes, labeled V_i, $i = 1, 2, 3$, and 4 as shown in Fig. 7, where volume V_3 with $a_{SL} = 6.27$ Å corresponds to the unstrained superlattice discussed in the previous section. For volumes V_1 and V_2, we have used the lattice constants $a_{SL} = 5.60$ and 5.82 Å, respectively, whereas volume V_4 has a lattice constant of $a_{SL} = 6.60$ Å.

For volume V_4, we obtain a Weyl phase similar to the one reported for volume V_3 above (see Appendix C). We denote the Weyl phase found for volumes V_3 and V_4 as WSM1. Comparing V_3 and V_4, we find that with increasing pressure $k_\parallel^*$ is reduced while k_z^* remains almost constant. The Weyl points move closer to the points $(0,0,\pm k_z^*)$ where they eventually annihilate each other as we show in the next subsection. We highlight that the considered heterostructures allow to obtain the Weyl phase even in absence of strain, which is an advantage over the bulk phases of HgTe and HgSe.
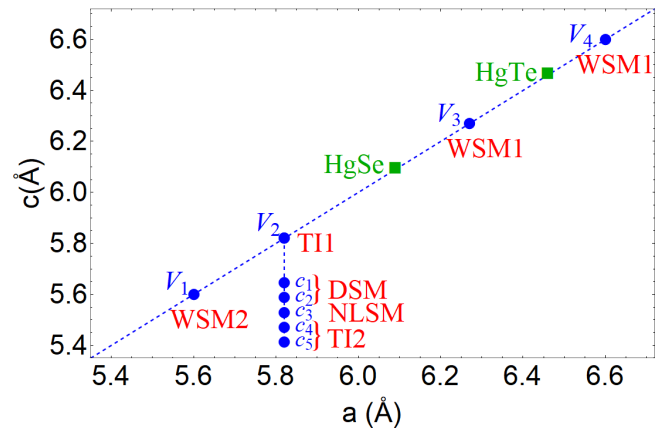

FIG. 7. Overview of topological phases in the HgTe/HgSe superlattices as a function of the lattice constants a and c: blue dots show the considered configurations of lattice constants. We denote different volumes resulting from hydrostatic pressure as V_i, where V_3 corresponds to the unstrained superlattice. In the case of uniaxial strain, we denote the compressed c-axis values with fixed in-plane lattice constant as c_i. The experimental values of bulk HgTe and HgSe are indicated by green squares. We have further indicated the associated topological phases for each point.

For the volume V_1, we observe a different WSM phase which we denote WSM2. The WSM phases WSM1 and WSM2 are separated by a small-gap topological insulator, which we denote TI1. In the following, we discuss the phases TI1 and WSM2 in more detail.

1. Small-gap topological insulator phase at volume V_2

Figure 8 shows the electronic properties for the compressed superlattice with volume V_2. Along the high-symmetry lines S-Γ-Z, the infinite superlattice band structure has a minimum band gap of 3 meV at $(0, 0, 0.0360\ \text{Å}^{-1})$ as shown in Fig. 8(a). The existence of a finite energy gap is further confirmed in the a very denser grid using our Wannier model. We have performed calculations along the path X_1-Γ_1-Y_1 with k_z components shifted to $k_z = k_z^* = 0.0360\ \text{Å}^{-1}$, which is presented in Fig. 8(b). Moreover, the points where the BIA splitting between the bands accidentally vanishes have now moved to the Fermi level and are now closer to the Γ point coinciding with the position of the minima of the bulk energy gap. This means that the BIA is tunable by the hydrostatic pressure and vanishes approximately at the Fermi level for the volume V_2. Coming from the Weyl phase, the Weyl points merge and gap out at the two points $(0, 0, \pm k_z^*)$ leading to a small-gap topological insulator that we denote TI1. This small-gap TI phase can also be viewed as an approximate Dirac semimetal with Dirac points at $(0, 0, \pm k_z^*)$ since it is in proximity of a DSM phase. This DSM phase is not topologically protected. Due to the presence of multiple band inversions, the gapped phase emerging here is a topological insulator phase. The recombination of Weyl points at $k = (0, 0, \pm k_z^*)$ due to the accidental vanishing of the BIA is unique to the superlattices considered here. In strained HgTe, on the contrary, the merging of Weyl points happens at the Γ point.
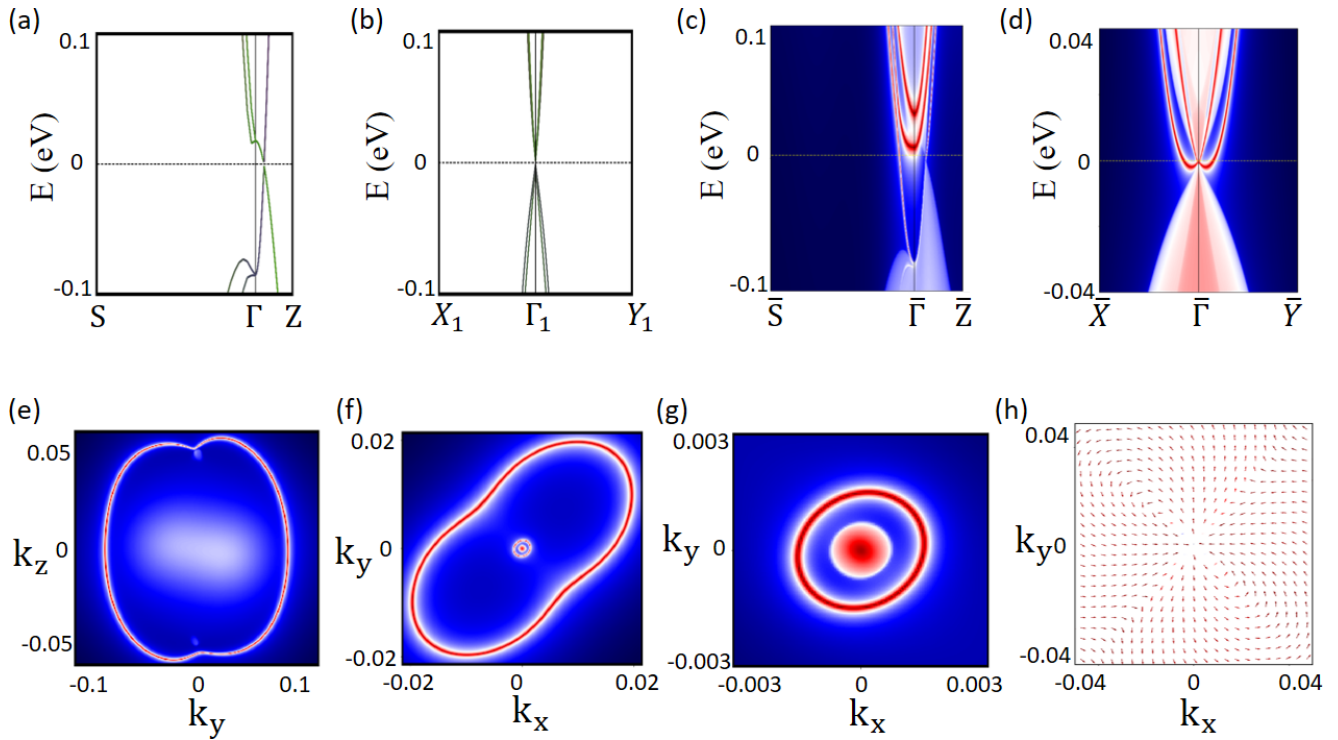
FIG. 8. Band structure of the HgTe/HgSe superlattice at the volume V_2 (a) along the high-symmetry lines S-Γ-Z. (b) Band structure in the k_x-k_y plane at $k_z = k_z^* = 0.0360$ Å^{-1}. Band structure of slabs with (c) (100) and (d) (001) surfaces. Fermi surfaces of the slabs with (e) (100) surfaces and (f) (001) surfaces. (g) Magnification of panel (f). (h) In-plane component of the Berry flux at the $k_z = 0$ plane.

We have further studied the electronic surface states of slabs of the compressed superlattice to confirm the nontrivial topological nature of the system. The band structures for the surface orientations (100) and (001) are presented in Figs. 8(c) and 8(d), respectively. These look similar to the corresponding band structures for the unstrained superlattice (compare to Fig. 6), except that the pair of linear band crossings in the bulk continuum has now merged to a single point in Fig. 8(d). This is in agreement with the recombination of Weyl points to a single Dirac point. Furthermore, we still observe topological surface states connecting the conduction and valence bands indicative of the topological nature of the compressed superlattice. A deeper insight into the structure of the surface states is gained from the corresponding Fermi surfaces for the (100) and (001) surface orientations of the slabs, as presented in Figs. 8(e)–8(g) Again comparing to Fig. 6 for the (100) termination in Fig. 8(e) we see that the previously open Fermi arcs now form a closed Fermi line of surface states pinned to the surface projections of the infinite superlattice Dirac points at $(0, \pm k_z^*)$. This Fermi line belongs to a single surface Dirac cone characteristic of a topological insulator. For the (001) termination in Figs. 8(f) and 8(g), we find a large closed Fermi line and two small Fermi circles centered at the $\bar{\Gamma}$. The inner Fermi circles originate from the fusion of the Weyl points.

2. Weyl semimetal at volume V_1

Reducing the volume further to the value V_1, we find another WSM phase that we denote as WSM1. The corresponding Weyl points re-emerge from the critical Dirac points

found for the volume V_2. This is due to the BIA increasing again, which accidentally vanished close to V_2. From the point of view of a model Hamiltonian, this can be understood considering that changes in the volume modify the ratio between the hopping parameters and the on-site energies, and therefore the BIA. Figure 9(a) shows the infinite superlattice band structure at the volume V_1 along the high-symmetry lines S-Γ-Z. Along these high-symmetry lines the minimum band gap is 12.3 meV. We have also calculated the band structure along the shifted path X_1-Γ_1-Y_1 with k_z components $k_z = k_z^* = 0.0353$ Å^{-1}, as shown in Fig. 9(b). Along this path, we find linear dispersions with gap closing points. There are a total of eight Weyl points. Their chiralities and relative arrangement in the BZ are similar to WSM2: The positions are $(0, \pm k_\parallel^*, \pm k_z^*)$ for the four Weyl points with chirality $+1$ and $(\pm k_\parallel^*, 0, \pm k_z^*)$ for the other four with chirality -1, where we have $k_z^* = 0.0353$ Å^{-1} and $k_\parallel^* = 0.0038$ Å^{-1}. Differently from the Weyl semimetal phase WSM2 for the volumes V_3 and V_4, the spin-orbit split bands cross now also in the valence band. As a consequence, from V_3 to V_1 we have a surface Lifshitz transition in the topological regime. Such a topological Lifshitz transition has already been observed in other Weyl semimetal compounds [67,68].

Another difference between the Weyl phases concerns the structure of surface states. The band structures of the slabs for the surface orientations (100) and (001) are reported in Figs. 9(c) and 9(d), respectively. The corresponding Fermi surfaces for the surface orientation (100) and (001) are shown in Figs. 9(e)–9(f), respectively. Figure 9(g) shows the magnification of the (001) Fermi surface close to $\bar{\Gamma}$.
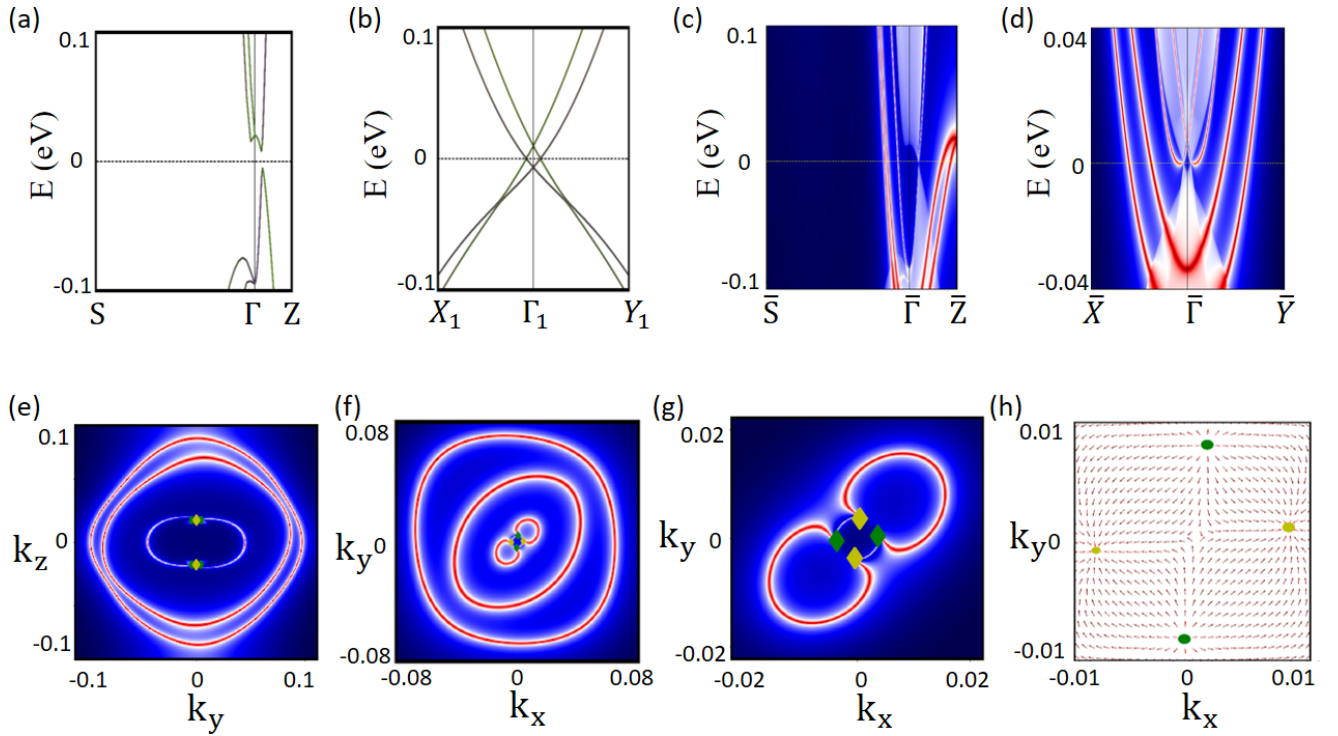
FIG. 9. Band structure of the HgTe/HgSe superlattice at the volume V_1 (a) along the high-symmetry lines S-Γ-Z. (b) Band structure in the plane containing the Weyl points at $k_z = k_z^* = 0.0353$ Å^{-1}. Band structure of slabs with (c) (100) surfaces and with (d) (001) surfaces. Fermi surfaces of the slabs with (e) (100) surfaces and with (f) (001) surfaces. (g) Magnification of panel (f) to visualize the Weyl points and their connectivity. (h) In-plane component of the Berry flux at the $k_z = k_\parallel^*$ plane including four Weyl points. The Weyl points at $(\pm k_\parallel^*, 0, \pm k_z^*)$ have chirality -1 (yellow diamond marker), while the Weyl points at $(0, \pm k_\parallel^*, \pm k_z^*)$ have chirality $+1$ (green circle marker). Diamond markers indicate chirality -2 (yellow) and $+2$ (green).

We observe that, with respect to WSM2 (compare to Fig. 6), there is a difference in the number of Fermi lines and in the connectivity of the Weyl points. For the (100) slab, we now observe two additional large circular Fermi rings encompassing the Weyl points and their Fermi arcs, whereas WSM2 showed only Fermi arcs. The (001) slab has one additional Fermi ring and the connectivity of the Weyl points has changed: instead of two separate pairs of Weyl node projections interconnected by two Fermi arcs, the Fermi arcs now connect all the Weyl-node projections in a chain-like fashion. Consequently, for both terminations the number of crossings along a given line through half of the surface BZ is the same as for WSM2 modulo 2. Hence, the infinite superlattice topology of the two WSM phases WSM1 and WSM2 is indeed the same [66]. Also the Berry flux reported in Fig. 9(h) is similar to the one for the volumes V_3 and V_4, confirming that the two WSM phases have the same topological properties.

Shrinking the volume further, we observe the Γ_6 band coming closer to the Fermi level. For the volume V_1, there is still a multiple band inversion between the p-orbitals and the Γ_6 band, as well as a band inversion involving $|3/2, \pm3/2\rangle$-Se and $|3/2, \pm1/2\rangle$-Te orbitals close to the Fermi level. A further reduction of the volume to unrealistic values pushes the Γ_6 level above the Fermi level creating a trivial insulator. This transition is favored if layers of trivial insulators, such as CdTe, are inserted into the heterostructure.

B. Topological properties as a function of uniaxial strain

To illustrate the effect of the strain, we first discuss the order of the energetic levels at the Γ point for the volume V_2. While the energetic levels can be labeled by their parities in the presence of inversion symmetry [69], this is not possible here. We start from the bulk HgTe and bulk HgSe energy levels Γ_8, Γ_7, and Γ_6 as shown in the outer parts of the top panel in Fig. 10(a). HgSe is more electronegative, so the energetic levels of HgSe are lower. Assuming the electrons can rearrange along the c-axis as it happens in the case of an interface, the effect of the strain on the energy levels $|3/2, \pm3/2\rangle$ and $|3/2, \pm1/2\rangle$ coming from the change of the lattice constant a_{SL} is different for HgTe and HgSe. Finally, considering the hybridization between the two components of the superlattice, i.e., HgSe and HgTe, we obtain the final order of the energetic levels, which is shown in the center of Fig. 10(a). In terms of orbital weights, we note that the states with s-orbital character are much more delocalized than the states with p-orbital character in zinc-blende superlattices [70]. Moreover, at the Γ point, the states with s-orbital character are decoupled from the states with p-orbital character. We further note that the final superlattice states with p-orbital character are mixtures of Te and Se orbitals, while Fig. 10(a) indicates only the main character (Te or Se) of the energetic levels.

Bulk HgTe realizes a type-I WSM phase at large uniaxial tensile strain and a TI phase at large uniaxial compressive strain, where the strain is with respect to the c axis. In
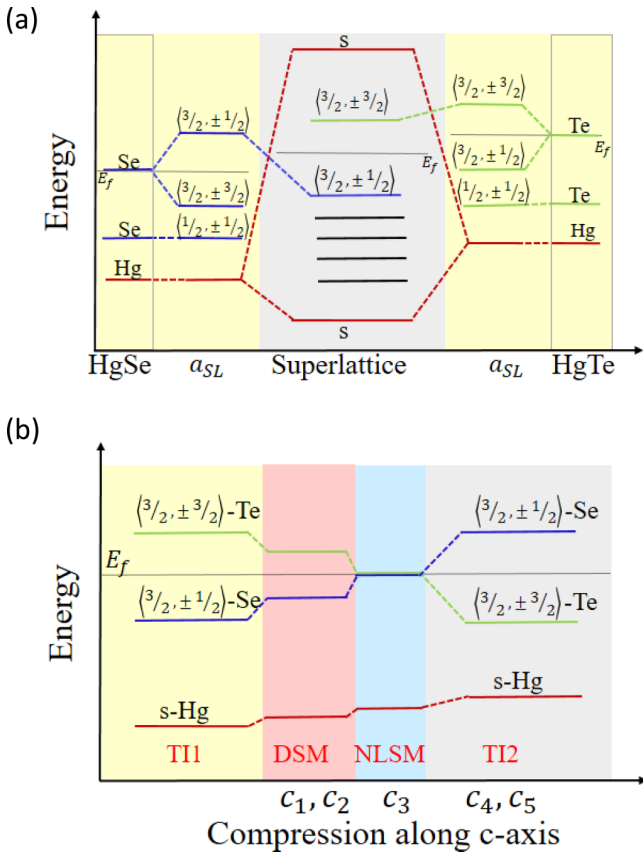
FIG. 10. (a) Schematic of energy levels in the superlattice with additional band inversion: the outer boxes show the energetic levels Γ_6, Γ_7, and Γ_8 in bulk HgTe and HgSe. Strain as an effect of changing the lattice constant of the superlattice (a_{SL}) splits the energy levels, while the interface hybridization (center) rearranges them. (b) Schematic of the energetic levels of s-Hg, $|3/2, \pm 1/2\rangle$-Te and $|3/2, \pm 3/2\rangle$-Se states as a function of the c lattice constant. The colors indicate the different topological phases DSM, NLSM, and TI. Note that the energy difference between $|3/2, \pm 1/2\rangle$ Te and $|3/2, \pm 3/2\rangle$ Se is not the crystal field, since the orbitals belong to different chalcogenide atoms. The colors red, green, and blue denote the main orbital character of the energetic levels, namely, Hg, Te, and Se, respectively.

between, the material is a type-II WSM [36,60,71]. Note that our strain notation is different from Ref. [60].

In this section, we investigate the evolution of the topological phases in the HgTe/HgSe superlattice as a function of uniaxial strain along the c axis. We start from the superlattice at the compressed volume V_2. We note, however, that we obtain the same progression of topological phases starting from the unstrained volume V_3. At the volume V_2, the heterostructure realizes a small-gap TI, which can be viewed as an approximate Dirac semimetal. We have performed calculations for compressed c axes corresponding to strain up to 7%. For small strain, we find that the energy gap closes at the Dirac points and the system remains a Dirac semimetal for an extended range of strain values. Subsequently, the superlattice realizes a nodal-line semimetal phase at around 5% of compression. Increasing the compressive uniaxial strain further, the HgTe/HgSe superlattice evolves into another TI phase

with a sizable energy gap. The TI phase of the HgTe/HgSe superlattice is similar to the one observed in strained HgTe. However, the path to arrive at the topological insulator phase is different as we will show below. A schematic diagram of the different phases is shown in Fig. 10(b). In the following, we analyze the arising phases in more detail.

1. Nodal-line semimetal at 5% compression

At 5% of compression, the minimal gap along the high-symmetry lines moves from the Z-Γ direction to the Γ-S direction as shown in Fig. 11(a). The reason is that, at the Γ point, the $|3/2, \pm 3/2\rangle$-Se orbital goes below the $|3/2, \pm 1/2\rangle$-Te orbital thereby undoing the band inversion between the associated bands. As a consequence, the bands lose their camel-back shape along the Γ-Z line to obtain a large Rashba band along the Γ-S line. The upper Rashba bands of the valence bands intersect the lower Rashba bands of the conduction band producing the features of the NLSM phase. Indeed, we find four nodal loops with a linear dispersion rendering this phase a NLSM. A path cutting through the nodal loops is shown in Fig. 11(b), where the nodal points are highlighted by red dots. The band structure in the $k_z = 0$ plane is illustrated in Fig. 11(h). The four nodal lines are located in the $k_x = \pm k_y$ planes. A visualization of the four nodal lines in the full BZ is provided in Fig. 11(g). These nodal lines are close to the Fermi level but are not isoenergetic. This is similar to the situation in bulk HgTe under tensile strain along the (111) axis [72], but the nodal lines in our heterostructure have a different structure. Furthermore, the nodal lines are protected by the M_{xy} and $M_{x\bar{y}}$ mirror symmetries. The band structure for slabs with (100) and (001) surface are reported in Figs. 11(c) and 11(d), respectively. The corresponding Fermi surfaces are shown in Figs. 11(e) and 11(f).

2. Topological insulator at 7% compression

At 7% of compression, the gap along the Γ-S direction increases as shown in Fig. 12(a). The nodal lines have shrunk to points and gapped out, as can be seen in Fig. 12(b) when compared with Fig. 11(b). The superlattice now realizes a topological insulator with a sizable gap and a single band inversion, which we denote TI2. This phase has properties similar to strained bulk HgTe [60] with a direct band gap of 10 meV and strong topological invariants ($\nu_0; \nu_1\nu_2\nu_3$) = (1;000). The band structure in the $k_z = 0$ plane is shown in Fig. 12(h). The electronic surface states for the (100) and (001) surface orientations are shown in Figs. 12(c) and 12(d) and the associated Fermi surfaces are displayed in Figs. 12(e)–12(g). For the (100) termination, we observe a Fermi ring centered at $\bar{\Gamma}$ associated with a single Dirac cone. Furthermore, there are additional trivial surface states. The (001) surface shows an odd number of Fermi rings centered at $\bar{\Gamma}$. However, only the central ring is associated with a Dirac cone, whereas the others are trivial surface states, as can be seen from comparing with Fig. 12(d).

VI. CONCLUSION AND OUTLOOK

We have investigated the evolution of topological phases in short-period HgTe/CdTe and HgTe/HgSe superlattices. The HgTe/CdTe superlattice realizes a nodal-line semimetal with
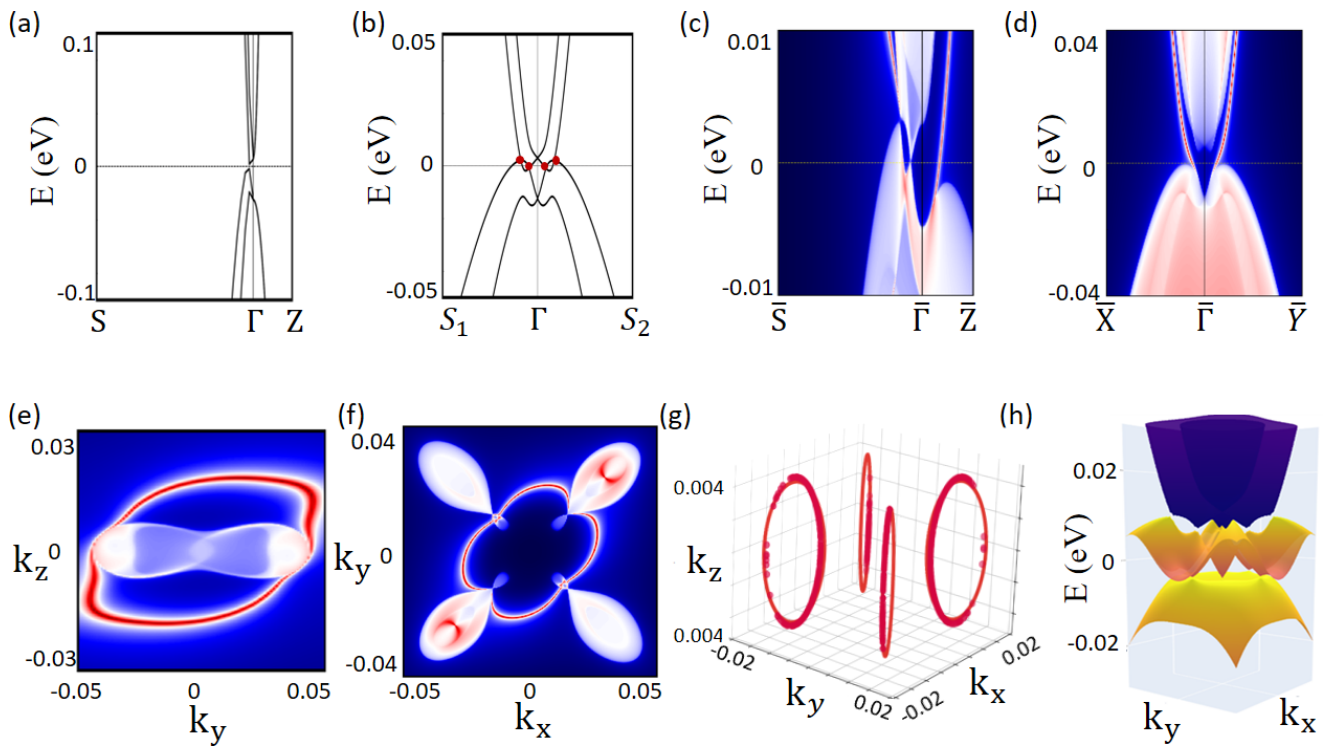
FIG. 11. Band structure of the HgTe/HgSe superlattice with 5% compressive strain (a) along the high-symmetry lines S-Γ-Z. (b) Wannier band structure in the plane at $k_z = 0$ plane where $S_1 = (0.085\frac{\pi}{a}, 0.085\frac{\pi}{b}, 0)$ and $S_2 = (-0.085\frac{\pi}{a}, -0.085\frac{\pi}{b}, 0)$. The nodal points are highlighted by red dots. Band structure of slabs with (c) (100) surfaces and (d) (001) surfaces. Fermi surfaces of the slabs with (e) (100) surfaces and with (f) (001) surfaces. (g) Nodal lines in the full BZ. (h) Band structure at the $k_z = 0$ plane.

FIG. 12. Band structure of the HgTe/HgSe superlattice with 7% compressive strain (a) along the high-symmetry lines S-Γ-Z. (b) Wannier band structure at $k_z = 0$ where $S_1 = (0.085\frac{\pi}{a}, 0.085\frac{\pi}{b}, 0)$ and $S_2 = (-0.085\frac{\pi}{a}, -0.085\frac{\pi}{b}, 0)$. Band structure of slabs with (c) (100) surface and (d) (001) surface. Fermi surfaces of the slabs with (e) (100) surfaces and with (f) (001) surfaces. (g) Magnification of (f). (h) Band structure in the $k_z = 0$ plane.
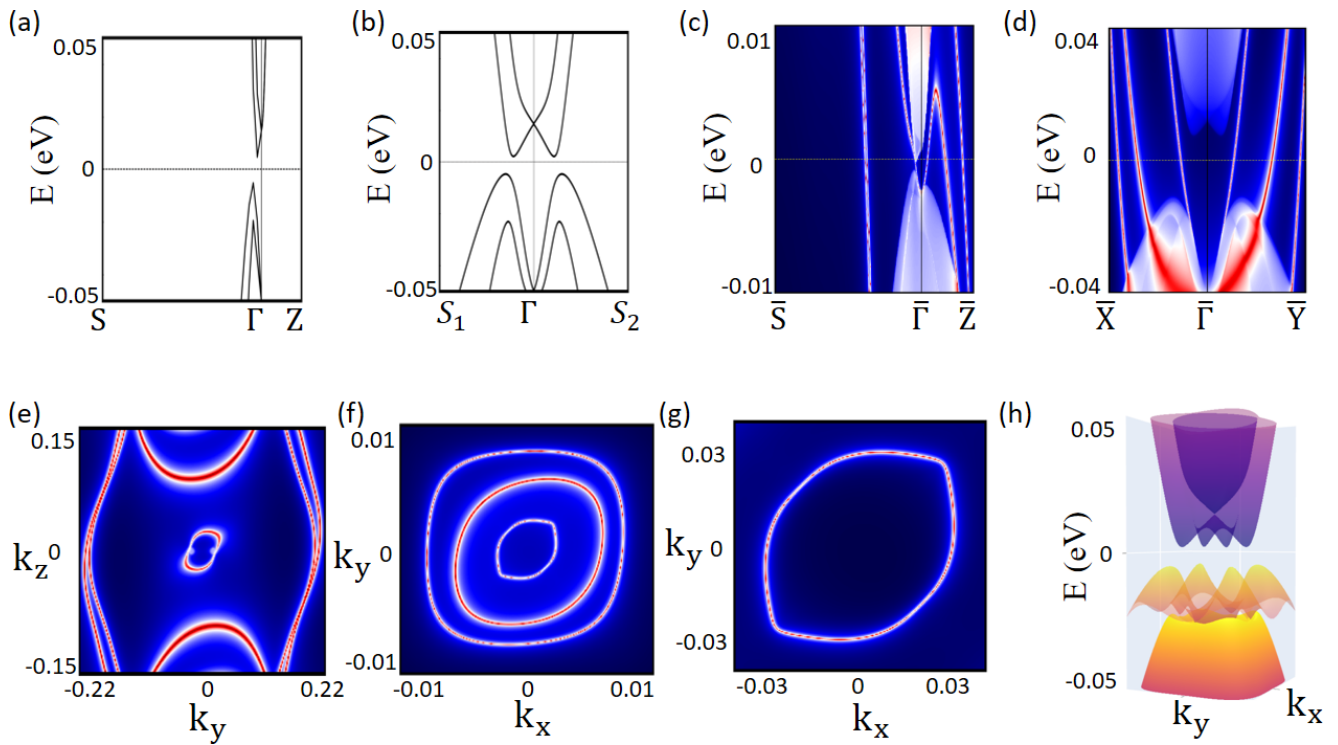
two isoenergetic, circular nodal lines at the Fermi level. Under compressive hydrostatic pressure, the superlattice becomes a trivial insulator. The HgTe/HgSe superlattice, in contrast, hosts a richer phase diagram and supports a plethora of topological phases with a Rashba-Dresselhaus spin-orbit splitting close to the Fermi level. The unstrained superlattice is an ideal Weyl semimetal with eight symmetry-related Weyl points at the Fermi level. It is a promising candidate for the realization of the 3D quantum Hall effect [73]. Under compression through hydrostatic pressure, the system becomes a small-gap topological insulator close to a Dirac phase as a consequence of an accidental reduction of the bulk inversion asymmetry. Further compression of the volume leads to another Weyl semimetal phase with the same bulk topological properties as the unstrained superlattice but with different Fermi-arc connectivities on the surface. Applying compressive uniaxial strain to the Dirac semimetal phase, the heterostructure goes through a nodal-line semimetal phase and a topological insulating phase with a single band inversion.

The nodal-line phases found in this work are relevant to the search for materials with carriers residing in flat energy bands which can support new correlation-driven collective phases [32], as recently proposed by some of the present authors [34]. The nodal-line phases in the HgTe/CdTe superlattices as well as the uniaxially strained HgTe/HgSe superlattices are promising candidates for the realization and study of three-dimensional flat bands, which could give rise to exotic, strongly correlated phases due to an enhancement of electronic interactions. Motivated by recent experimental progress in the growth of II-VI strained nanostructures by molecular beam epitaxy [74,75] and high electron mobility systems [76,77], the synthesis of core-shell nanowires of the HgTe-based superlattices is a possible way to create the required bend to obtain the flat bands. In fact, nanowires of II-IV semiconductors have recently been fabricated [78,79]. Moreover, the superconductivity induced by the flat bands in a band-inverted nanowire could be a platform to host topological superconductivity and Majorana zero modes.

As another promising research direction, 2D quantum wells of HgTe/HgSe with a thickness larger than the critical thickness and sandwiched between CdTe could generate a topological insulator with multiple band inversions and host new exotic phases beyond the quantum spin Hall effect. Experimentally, a challenge will be the fabrication of a sufficiently sharp interface between HgTe and HgSe, since the system will tend to create a digital alloy. Nonetheless, we expect a nearly ideal Weyl semimetal phase, which is topologically protected and appears at zero strain, to be achievable even in the case of a digital alloy.

The data shown in the figures are available at Ref. [80].

APPENDIX A: COMPUTATIONAL DETAILS

Electronic structure calculations were performed within the framework of the first-principles density functional theory based on a plane wave basis set and the projector augmented wave method using VASP [81] package. The calculation is fully relativistic by considering spin-orbit coupling (SOC). A plane-wave energy cutoff of 250 eV has been used. As an exchange-correlation functional, the generalised gradient approximation (GGA) of Perdrew, Burke, and Ernzerhof has been adopted [50]. We have performed the calculations using $6 \times 6 \times 4$ k points centered at Γ with 144 k points in the BZ for the superlattice with 24 atoms shown in Fig. 2(a).

The band order and band gap of the bulk have been validated with a meta-GGA approach, which is the modified Becke-Johnson exchange potential together with local density approximation for the correlation potential scheme [82]. We have performed the calculation using MBJGGA with the parameter $C_{MBJ} = 1.11$ in order to get the experimental band ordering for both HgTe and HgSe. The GGA band ordering of HgSe is Γ_8, Γ_7, and Γ_6 in agreement with the experimental band ordering. However, the GGA band ordering of the HgTe is Γ_8, Γ_7, and Γ_6 while the experimental band ordering is Γ_8, Γ_6, and Γ_7. The electronic properties of the HgTe/HgSe superlattice are not affected by the use of the GGA since the bands near the Fermi level of the superlattice are dominated by the bands associated with Γ_8 which remains unchanged in both functionals.

The electronic structure calculation of the heterostructure was performed using both GGA and meta-GGA for the volume V_3 discussed in the main text. Within GGA and meta-GGA, we obtain the same qualitative results for the volume V_3. Therefore, we considered the GGA exchange-correlation functional throughout this paper. We study the systems without structural relaxation not to add further degrees of freedom and complexity to the topological phase diagram.

We extracted the real space tight-binding Hamiltonian with atom-centred Wannier functions with s-like cation and p-like

TABLE I. Values of band inversion strength E_g, spin-orbit constant Δ_{SOC} and lattice constant a of bulk zinc blende structures for two different exchange-correlation functionals (GGA and MBJGGA).

E_{XC}	Material	E_g (meV)	Δ_{SOC} (meV)	a (Å)
GGA	HgTe	−976	743	6.46
	HgSe	−1028	219	6.08
	HgS	−429	117	5.85
	CdTe	+1119	821	6.60
MBJGGA	HgTe	−315	708	6.46
	HgSe	−235	183	6.08
	HgS	+429	290	5.85
	CdTe	+1267	801	6.60

anion orbital projections using the VASP2WANNIER90 interface [83]. The topological properties are studied using the WANNIERTOOLS package [84]. The surface states are obtained within the iterative Green's function approach [85]. We used a denser k-point grid $16 \times 16 \times 4$ to generate the model Hamiltonian with the Wannier basis. Since both the (100) and the (001) surface are polar, the anion and cation terminations differ from a quantitative point of view including small differences in the Fermi level and different number of surface states. In the main text, we present results for the terminations that show the best visualizations for our purposes.

APPENDIX B: TOPOLOGICAL BULK PROPERTIES

The bulk properties were analyzed using the experimental lattice constants of HgX (i.e., X = Te, Se, S) materials with zinc blende crystal structure. We have calculated the band gap (E_g), the band order and the spin-orbit coupling (Δ_{SOC}). The values are tabulated in Table I. The band inversion between Hg-s orbital and X-p orbital occurs at the Γ point which indicates a topological insulator (TI) phase in this class of materials. According to the symmetry of the wave function, the Hg-s or Cd-s bands are labeled as Γ_6 and the Te-p, Se-p, or S-p bands split into $\Gamma_8 (j = \frac{3}{2})$ and $\Gamma_7 (\frac{1}{2})$ bands with SOC. We define the following quantities:

$$\Delta_{SOC} = \Gamma_8 - \Gamma_7, \qquad (B1)$$

$$E_g = \Gamma_6 - \Gamma_8, \qquad (B2)$$

which we report in Table I.

In the case of a trivial insulator, the cation s type of bands lies above the anion p type of bands while the scenario is opposite for the topological insulating phase. HgTe and HgSe are topological zero-gap semimetals with positive spin-orbit gap. However, HgS has a negative spin-orbit gap and it is a trivial insulator in agreement with experimental results.

The volume can tune the effective spin-orbit gap via the hopping between d electrons of Hg and p electrons of the chalchogen atoms. The bare SOC of S is positive, but becomes negative due to the p-d hopping. However, the spin-orbit couplings of Te and Se are one order of magnitude larger than the variation that can be induced by these effects. Therefore these are not relevant effects in this case.
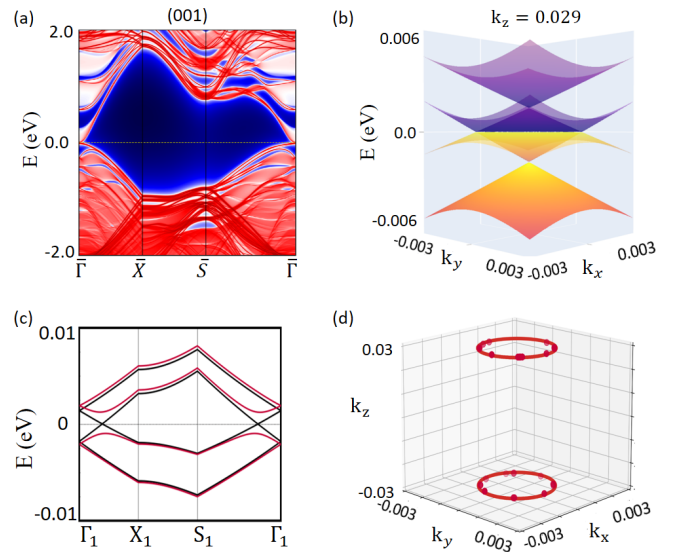

FIG. 13. (a) Surface band structure of the (001) Te-terminated surface of the (HgTe)$_4$/(CdTe)$_4$ superlattice. (b) Band structure of the infinite superlattice in the E-k_x-k_y space at fixed $k_z = 0.029$ Å^{-1}. (c) Band structure with nodal points at k_z=0.029 Å^{-1}(black) and gapped at $k_z = 0.030$ Å^{-1} (red). These four bands are a set of bands isolated from the rest of the band structure. (d) Nodal lines of the infinite superlattice at the $k_z = \pm 0.029$ Å^{-1} planes.

Another way to tune the effective spin-orbit coupling is uniaxial pressure, which changes the crystal field energy difference $\varepsilon_{x,y}$-ε_z, but also in this case, the effect is too small to change significantly the SOC of Te and Se.

APPENDIX C: NODAL LINE FOR (HgTe)$_4$/(CdTe)$_4$ SUPERCELL

Here we discuss the isoenergetic nodal line present in the (HgTe)$_4$/(CdTe)$_4$ superlattice. The results are qualitatively similar to the (HgTe)$_3$/(CdTe)$_3$ results provided in Fig. 4 of the main text. The band structure projected on the (001) surface shows topological surface states connecting valence and conduction bands as reported in Fig. 13(a). The band structure has two isoenergetic circular nodal lines with the same radius in the planes k_z^*=±0.029 Å^{-1} as shown in Fig. 13(b) at fixed k_z and in Fig. 13(c) along specific lines through the Brillouin zone. The nodal-line radius is smaller than in the case of (HgTe)3/(CdTe)3, as can be seen in Fig. 13(d). Therefore we expect it to further shrink with increasing number of layers until it disappears.

APPENDIX D: WEYL SEMIMETAL PHASE IN HgTe/HgSe AT THE VOLUME V_4

Figure 14(a) shows the band structure for the volume V_4 along the high-symmetry lines S-Γ-Z. Considering just the high-symmetry lines in the k space, the minimum band gap is 13.2 meV along the ΓZ direction. A linear dispersion with gap closing typical of Weyl points is found along the X_1-Γ_1-Y_1 direction as shown in Fig. 14(b), where Γ_1=(0,0,k_z^*), $X_1 = (0.2\pi/a, 0, k_z^*)$ and $Y_1 = (0, 0.2\pi/a, k_z^*)$. For the volume V_4, we found that $k_z^* = 0.0536$ Å^{-1}. The crossing point between
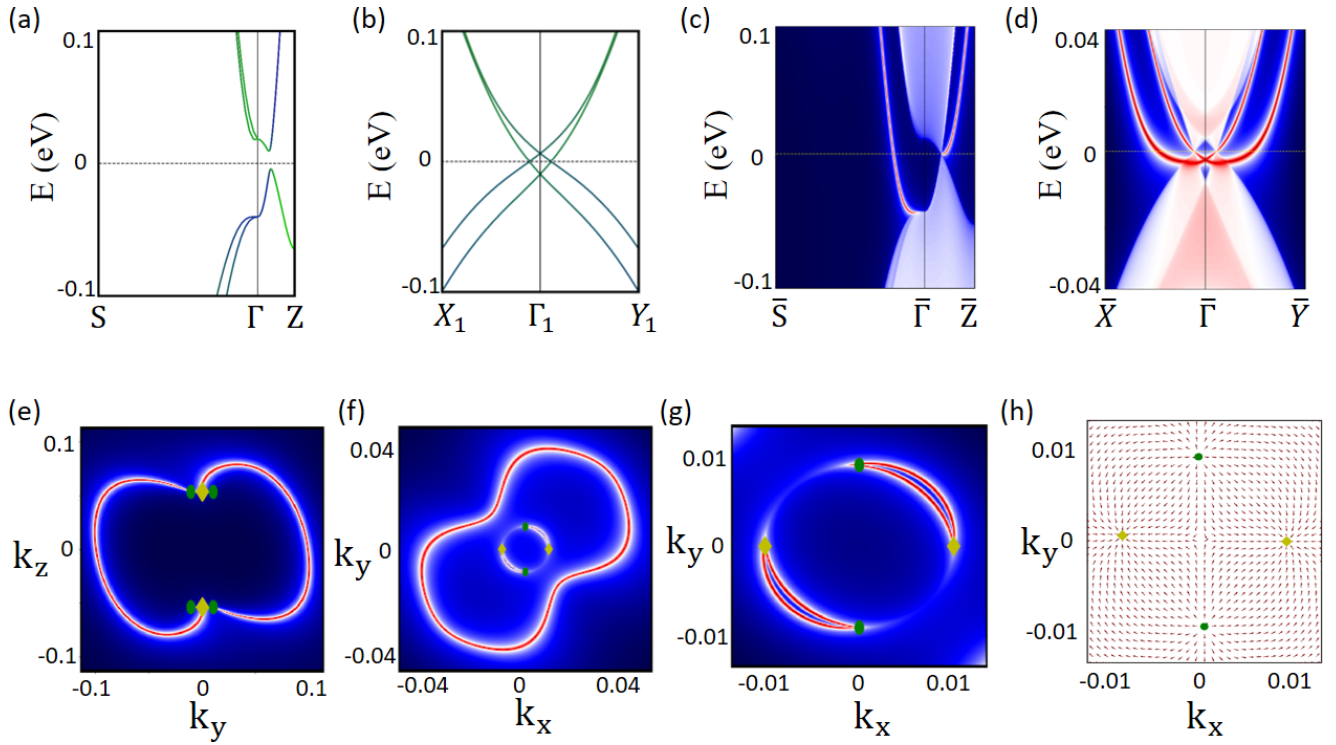
FIG. 14. Band structure of the HgTe/HgSe infinite superlattice at the volume V_4 (a) along the S-Γ-Z high-symmetry lines. (b) Band structure in the plane of the Weyl points at $k_z = k_z^* = 0.0536$ Å^{-1}. Band structure projected onto the (c) (100) surface and (d) (001) surface orientations. Fermi surface of the slab for the (e) (100) surface (f) of the (001) surface orientations. Red means presence of electronic states while blue means absence of electronic states. (g) Magnification of the previous panel where we can clearly see the Weyl points and their connectivity. (h) In-plane component of the Berry flux at the $k_z = k_z^*$ plane including four Weyl points. The Weyl points located at $(\pm k_\parallel^*, 0, \pm k_z^*)$ have chirality -1 (yellow diamond marker), while the Weyl points located at $(0, \pm k_\parallel^*, \pm k_z^*)$ have chirality $+1$ (green circle marker).

the bands at the Fermi level determines the position of the Weyl points.

The presence of a topologically protected Fermi arc is a hallmark of the Weyl semimetal phase. To confirm the topological nature of the 3D superlattice, we have calculated the surface electronic states and Fermi arcs for the (100) and (001) surface orientations considering the notation of the conventional unit cell as shown in Fig. 2(a). The (010) surface is equivalent to the (100) surface. The band structure of the slab for the surface orientation (100) with chalcogenides termination is shown in Fig. 14(c). The topological surface states connecting the valence and the conduction bands confirm the topological nature of the system, moreover we have a gapless point at the coordinates $(0, k_z^*)$ projected on the 2D BZ of the slab. The Fermi surface for the slab with surface orientation (100) is shown in Fig. 14(e). It has six gapless points, four points with projected coordinates $(\pm k_\parallel^*, \pm k_z^*)$ and monopole charge $+1$ and two points with coordinates $(0, \pm k_z^*)$ and monopole charge -2, where $k_\parallel^* = 0.0105$ Å^{-1}. Open Fermi arcs are observed. A clear connectivity between the monopole charge -2 and one of the monopole charges $+1$ is visible. However, the other connectivity is not clearly visible due to the short distance between the Weyl points for this surface orientation.

The band structure for the slab with (001) surface orientation is shown in Fig. 14(d). Two gapless points are present

at $(k_\parallel^*, 0)$ and $(0, k_\parallel^*)$. The Fermi surface of the slab with orientation (001) is shown in Fig. 14(f) and its magnification is in Fig. 14(g). We can see one closed Fermi surface due to the bulk topology and the Weyl points around $\bar{\Gamma}$. The Weyl points with monopole charge $+2$ are projected at $(0, \pm k_\parallel^*)$, while the Weyl points with monopole charge of -2 are projected at $(\pm k_\parallel^*, 0)$ with a clear connection between them.

Furthermore, we have calculated the Berry curvature in the $k_x - k_y$ plane, at fixed $k_z^* = 0.0536$ Å^{-1} around the Weyl points shown in Fig. 14(h). Looking at the Berry curvature, the Weyl points with chirality $+1$ behave as a source, while Weyl points with chirality -1 as a sink. Due to the absence of trivial Fermi surfaces, the Weyl phase in multilayer 3D superlattice could be experimentally detected. It is also noticeable that the Weyl points are well separated by an in-plane distance between opposite chiralities of 2.2% of the reciprocal lattice constant.

APPENDIX E: DIRAC SEMIMETAL OF HgTe/HgSe AT 3% COMPRESSION

Applying compressive strain along the c axis starting from superlattice volume V_2, the phase is gapless at 3% of strain. We find a Dirac-like dispersion with a fourfold degeneracy as we can see in Fig. 15(a). The linear dispersion is clearly visible along the path X_1-Γ_1-Y_1 as shown in Fig. 15(b), where
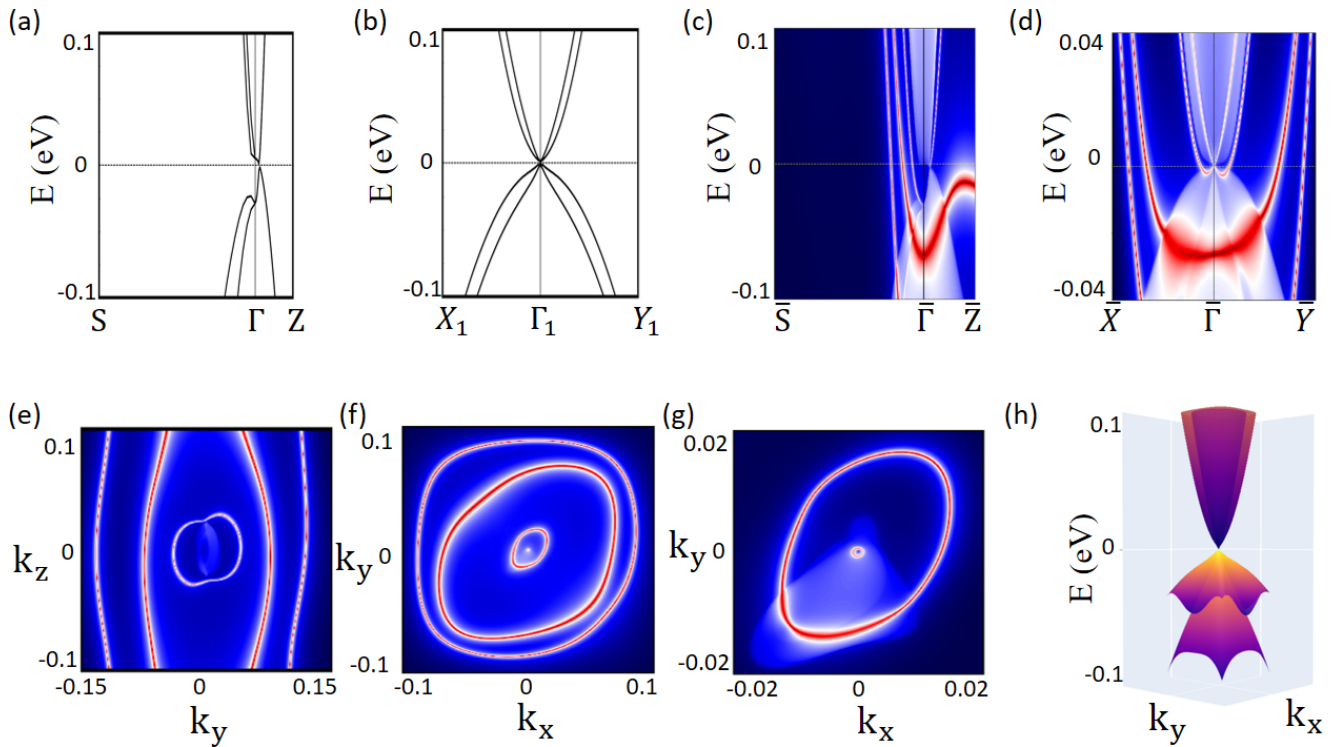
FIG. 15. Band structure of the HgTe/HgSe superlattice with 3% compressive strain (a) along the high-symmetry lines S-Γ-Z and (b) in the plane of the Dirac points at $k_z = k_z^* = 0.021$ Å^{-1}. Band structure for slabs with (c) (100) and (d) (001) surfaces. Fermi surfaces of the slabs with (e) (100) and (f) (001) surfaces. (g) Magnification of (f). (h) Band structure in the k_z^*=0.021 Å^{-1} plane.

we have defined $\Gamma_1 = (0, 0, k_z^*)$, $X_1 = (0.1\pi/a, 0, k_z^*)$ and $Y_1 = (0, 0.1\pi/a, k_z^*)$ with $k_z^* = 0.021$ Å^{-1}. The two Dirac points are located at $(0, 0, \pm k_z^*)$.

The electronic states of the slab with (100) surface orientation are shown in Fig. 15(c), while the results for the (001) surface orientation are presented in Fig. 15(d). The respective Fermi surfaces are shown in Figs. 15(e) and 15(f). For the (100) termination, as compared to the volume V_2 (see Fig. 8), we observe that the Fermi circle associated with the surface Dirac cone is now interrupted by the surface projections of the infinite superlattice Dirac points at $(0, \pm k_z^*)$. This leads to closed Fermi-arc features characteristic of Dirac semimetals. For the (001) termination, we find three Fermi rings around $\bar{\Gamma}$, which is similar to what we see for the volume V_2. Notably, the innermost Fermi ring now has a larger radius revealing the projections of the Dirac points at $\bar{\Gamma}$. In Fig. 15(g), the band structure at $k_z = k_z^*$ shows the Dirac point.

APPENDIX F: SEMIMETAL WITH PARABOLIC DISPERSION OF HgTe/HgSe AT 4% COMPRESSION

At 4% compressive strain, the gap along Γ-Z direction vanishes and our system becomes metallic as we can see in Fig. 16(a). The band structure with parabolic behavior along X_1-Γ-Y_1 in Fig. 16(b) confirms the metallicity. Figures 16(c) and 16(d) show the band structure projected in the (100) and (001) surface orientations, respectively. The associated Fermi

surface are represented in Figs. 16(e) and 16(f). Figure 16(g) represents a magnification of the (001) Fermi surface around the Γ point. The 3D band structure with parabolic dispersion is shown in Fig. 16(h) for $k_z = k_z^* = 0.010$ Å^{-1}.

The system shows a coexistence of topological surface states and metallic states. At this lattice constant, the system is turning from the DSM phase to a NLSM phase.

APPENDIX G: TOPOLOGICAL INSULATOR PHASE OF HgTe/HgSe AT 6% COMPRESSION

At 6% of compression, the band inversion between $|3/2, \pm 3/2\rangle$ Se and $|3/2, \pm 1/2\rangle$ Te has disappeared as well as the nodal line. We can still observe a strong Rashba effect in the valence band which is now at the Fermi level, the Rashba in the valence band is unusual but was observed in the literature [86]. Therefore we are left with an insulator with a single band inversion between the s orbital and the p orbital as in bulk HgTe with a band gap of 3 meV. As a consequence, the band crossing is lifted along ΓS as shown in Figs. 17(a) and 17(b): the superlattice becomes a TI. This TI phase is equivalent to the TI phase discussed in the context of strained HgTe [60]. The surface states of the (100) and (001) terminations are shown in Figs. 17(c) and 17(d), and the associated Fermi surfaces are shown in Figs. 17(e) and 17(f). The 3D band structure is shown in Fig. 17(g).

FIG. 16. Band structure of HgTe/HgSe superlattice with 4% compressive strain (a) along the high-symmetry lines S-Γ-Z. (b) and in the plane of the Dirac points at $k_z = k_z^* = 0.010$ Å^{-1}. Projected surface bands onto the (c) (100) surface and (d) (001) surface orientations. Fermi surface of the slab for the (e) (100) surface (f) of the (001) surface orientation. (g) Band structure at the $k_z = k_z^* = 0.010$ Å^{-1} plane.
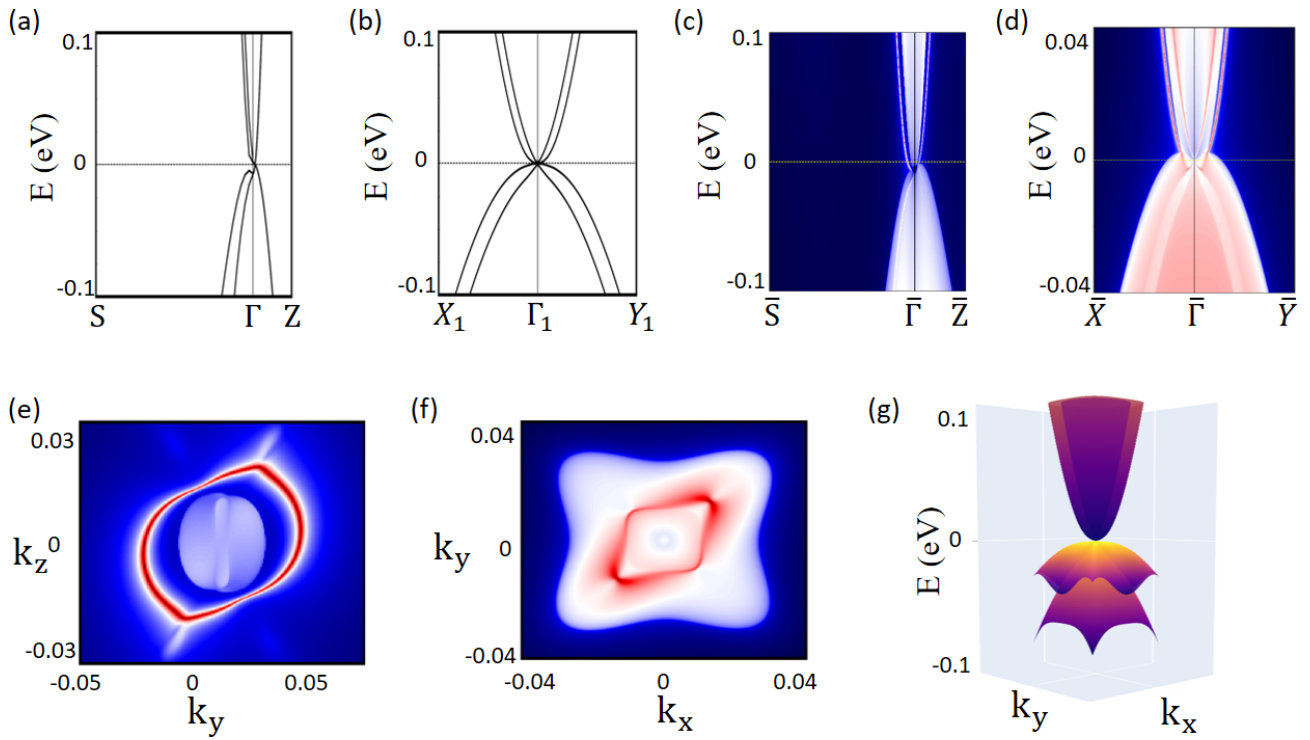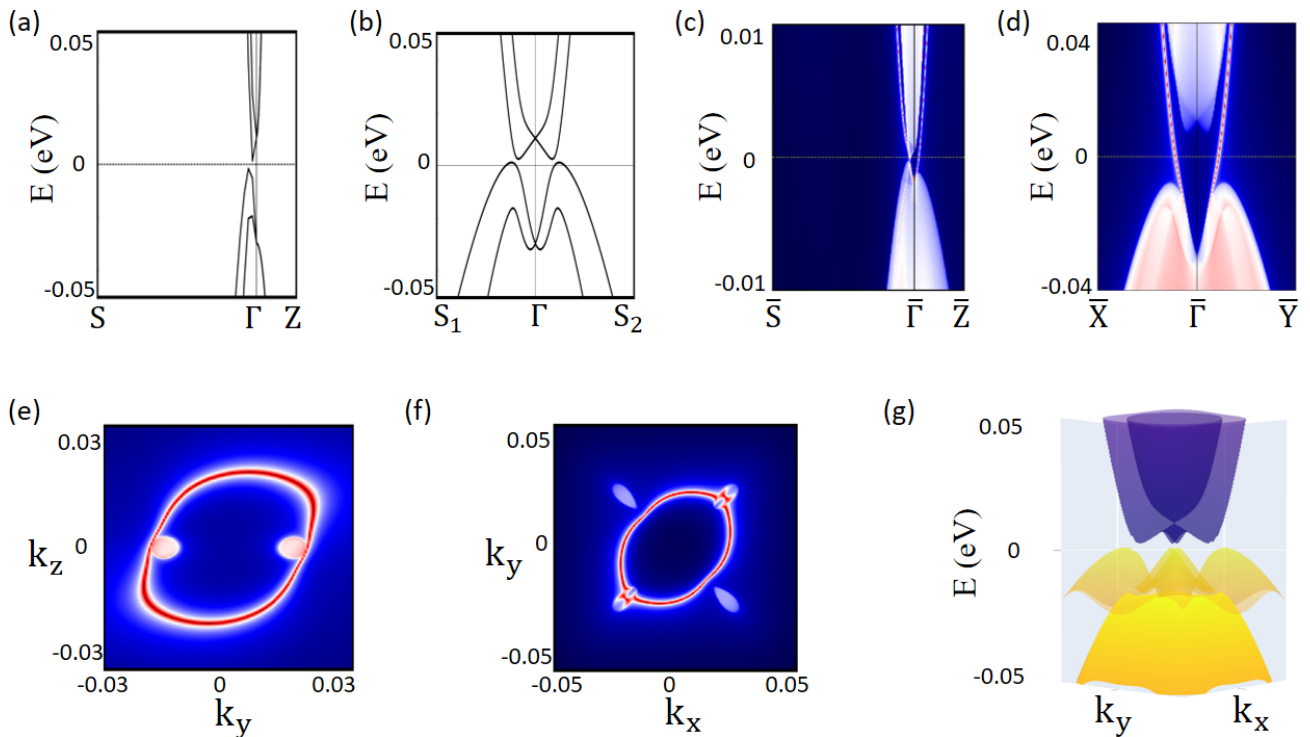

FIG. 17. Band structure of HgTe/HgSe superlattice with 6% compressive strain (a) along the high-symmetry lines S-Γ-Z. (b) Wannier band structure at $k_z = 0$. Projected surface bands onto the (c) (100) surface and (d) (001) surface orientation. Fermi surface of the slab for the (e) (100) surface (f) of the (001) surface orientation. (g) band structure at the $k_z = 0$ plane.

[1] C. L. Kane and E. J. Mele, Quantum Spin Hall Effect in Graphene, Phys. Rev. Lett. **95**, 226801 (2005).

[2] B. A. Bernevig, T. L. Hughes, and Shou-Cheng Zhang, Quantum spin Hall effect and topological phase transition in HgTe quantum wells, Science **314**, 1757 (2006).

[3] M. König, S. N. Wiedmann, C. Brüne, A. Roth, H. Buhmann, L. W. Molenkamp, Xiao-Liang Qi, and Shou-Cheng Zhang, Quantum spin Hall insulator state in HgTe quantum wells, Science **318**, 766 (2007).

[4] Liang Fu, C. L. Kane, and E. J. Mele, Topological Insulators in Three Dimensions, Phys. Rev. Lett. **98**, 106803 (2007).

[5] A. Bansil, Hsin Lin, and Tanmoy Das, Colloquium: Topological band theory, Rev. Mod. Phys. **88**, 021004 (2016).

[6] M. Z. Hasan and C. L. Kane, Topological insulators, Rev. Mod. Phys. **82**, 3045 (2010).

[7] Xiao-Liang Qi and Shou-Cheng Zhang, Topological insulators and superconductors, Rev. Mod. Phys. **83**, 1057 (2011).

[8] Liang Fu, Topological Crystalline Insulators, Phys. Rev. Lett. **106**, 106802 (2011).

[9] T. H. Hsieh, H. Lin, J. Liu, W. Duan, A. Bansil, and L. Fu, Topological crystalline insulators in the SnTe material class, Nat. Commun. **3**, 982 (2012).

[10] P. Dziawa, B. J. Kowalski, K. Dybko, R. Buczko, A. Szczerbakow, M. Szot, E. Łusakowska, T. Balasubramanian, B. M. Wojek, M. H. Berntsen *et al.*, Topological crystalline insulator states in $Pb_{1-x}Sn_x$Se, Nat. Mater. **11**, 1023 (2012).

[11] Y. Tanaka, Z. Ren, T. Sato, K. Nakayama, S. Souma, T. Takahashi, K. Segawa, and Y. Ando, Experimental realization of a topological crystalline insulator in SnTe, Nat. Phys. **8**, 800 (2012).

[12] S. M. Young, S. Zaheer, J. C. Y. Teo, C. L. Kane, E. J. Mele, and A. M. Rappe, Dirac Semimetal in Three Dimensions, Phys. Rev. Lett. **108**, 140405 (2012).

[13] Z. Liu, J. Jiang, B. Zhou, Z. Wang, Y. Zhang, H. Weng, D. Prabhakaran, S.-K. Mo, H. Peng, P. Dudin, T Kim, M. Hoesch, Z. Fang, X. Dai, Z. Shen, D Feng, Z. Hussain, and Y Chen, A stable three-dimensional topological Dirac semimetal Cd_3As_2, Nat. Mater. **13**, 677 (2014).

[14] N.-P. Armitage, E.-J. Mele, and A. Vishwanath, Weyl and Dirac semimetals in three-dimensional solids, Rev. Mod. Phys. **90**, 015001 (2018).

[15] A. S Wadge, G. Grabecki, C. Autieri, B. J Kowalski, P. Iwanowski, G. Cuono, M. F. Islam, C. M. Canali, K. Dybko, A. Hruban, A. Łusakowski, T. Wojciechowski, R. Diduszko, A. Lynnyk, N. Olszowska, M. Rosmus, J. Kołodziej, and A. Wiśniewski, Electronic properties of TaAs2 topological semimetal investigated by transport and ARPES, J. Phys.: Condens. Matter **34**, 125601 (2022).

[16] S.-Y. Xu, I. Belopolski, N. Alidoust, M. Neupane, G. Bian, C. Zhang, R. Sankar, G. Chang, Z. Yuan, C.-C. Lee *et al.*, Discovery of a Weyl fermion semimetal and topological Fermi arcs, Science **349**, 613 (2015).

[17] S.-Y. Xu, N. Alidoust, I. Belopolski, Z. Yuan, G. Bian, T.-R. Chang, H. Zheng, V. Strocov, D. Sanchez, G. Chang, C. Zhang, D. Mou, Y. Wu, L. Huang, C.-C. Lee, S.-M. Huang, B. Wang, A. Bansil, H.-T. Jeng, and M. Z. Hasan, Discovery of a Weyl fermion state with Fermi arcs in niobium arsenide, Nat. Phys. **11**, 748 (2015).

[18] B. Q. Lv, H. M. Weng, B. B. Fu, X. P. Wang, H. Miao, J. Ma, P. Richard, X. C. Huang, L. X. Zhao, G. F. Chen, Z. Fang, X.

Dai, T. Qian, and H. Ding, Experimental Discovery of Weyl Semimetal TaAs, Phys. Rev. X **5**, 031013 (2015).

[19] I. Belopolski, K. Manna, D. S. Sanchez, G. Chang, B. Ernst, J. Yin, S. S. Zhang, T. Cochran, N. Shumiya, H. Zheng, B. Singh, G. Bian, D. Multer, M. Litskevich, X. Zhou, S.-M. Huang, B. Wang, T.-R. Chang, S.-Y. Xu, A. Bansil *et al.*, Discovery of topological Weyl fermion lines and drumhead surface states in a room temperature magnet, Science **365**, 1278 (2019).

[20] C. Fang, Y. Chen, H.-Y. Kee, and L. Fu, Topological nodal line semimetals with and without spin-orbital coupling, Phys. Rev. B **92**, 081201(R) (2015).

[21] C. Fang, H. Weng, X. Dai, and Z. Fang, Topological nodal line semimetals, Chin. Phys. B **25**, 117106 (2016).

[22] T.-R. Chang, I. Pletikosic, T. Kong, G. Bian, A. Huang, J. Denlinger, S. K. Kushwaha, B. Sinkovic, H.-T. Jeng, T. Valla, W. Xie, and R. J. Cava, Realization of a type-II nodal-line semimetal in Mg_3Bi_2, Adv. Sci. **6**, 1800897 (2019).

[23] W. Lei, W. Wang, X. Ming, S. Zhang, G. Tang, X. Zheng, H. Li, and C. Autieri, Structural transition, metallization, and superconductivity in quasi-two-dimensional layered PdS_2 under compression, Phys. Rev. B **101**, 205149 (2020).

[24] B. Singh, X. Zhou, H. Lin, and A. Bansil, Saddle-like topological surface states on the $TT'X$ family of compounds (T, T' = Transition metal, X = Si, Ge), Phys. Rev. B **97**, 075125 (2018).

[25] C.-X. Liu, X.-L. Qi, X. Dai, Z. Fang, and S.-C. Zhang, Quantum anomalous Hall effect in $Hg_{1-y}Mn_y$Te quantum wells, Phys. Rev. Lett. **101**, 146802 (2008).

[26] R. Yu, W. Zhang, H.-J. Zhang, S.-C. Zhang, X. Dai, and Z. Fang, Quantized anomalous Hall effect in magnetic topological insulators, Science **329**, 61 (2010).

[27] C.-Z. Chang, J. Zhang, X. Feng, J. Shen, Z. Zhang, M. Guo, K. Li, Y. Ou, P. Wei, L.-L. Wang, Z.-Q. Ji, Y. Feng, S. Ji, X. Chen, J. Jia, X. Dai, Z. Fang, S.-C. Zhang, K. He, Y. Wang *et al.*, Experimental observation of the quantum anomalous Hall effect in a magnetic topological insulator, Science **340**, 167 (2013).

[28] N. Pournaghavi, M. F. Islam, R. Islam, C. Autieri, T. Dietl, and C. M. Canali, Realization of the Chern-insulator and axion-insulator phases in antiferromagnetic $MnTe/Bi_2(Se,Te)_3$MnTe heterostructures, Phys. Rev. B **103**, 195308 (2021).

[29] M. Mogi, M. Kawamura, R. Yoshimi, A. Tsukazaki, Y. Kozuka, N. Shirakawa, K. Takahashi, M. Kawasaki, and Y. Tokura, A magnetic heterostructure of topological insulators as a candidate for an axion insulator, Nat. Mater. **16**, 516 (2017).

[30] Y. Xu, Z. Song, Z. Wang, H. Weng, and X. Dai, Higher-order topology of the axion insulator $EuIn_2As_2$, Phys. Rev. Lett. **122**, 256402 (2019).

[31] R. Islam, S. Mardanya, A. Lau, G. Cuono, T.-R. Chang, M. S. Bahramy, B. Singh, C. M. Canali, T. Dietl, and C. Autieri, Axion insulating phase in superlattices without inversion symmetry (unpublished).

[32] N. Regnault, Y. Xu, M.-R. Li, D.-S. Ma, M. Jovanovic, A. Yazdani, S. S. P. Parkin, C. Felser, L. M. Schoop, N. P. Ong, R. J. Cava, L. Elcoro, Z.-D. Song, and B. A. Bernevig, Catalogue of flat band stoichiometric materials, Nature (London) **603**, 824 (2022).

[33] Y. Cao, V. Fatemi, S. Fang, K. Watanabe, T. Taniguchi, E. Kaxiras, and P. Jarillo-Herrero, Unconventional superconductivity in magic-angle graphene superlattices, Nature (London) **556**, 43 (2018).

[34] A. Lau, T. Hyart, C. Autieri, A. Chen, and D. I. Pikulin, Designing Three-Dimensional Flat Bands in Nodal-Line Semimetals, Phys. Rev. X **11**, 031017 (2021).

[35] A. A. Burkov and L. Balents, Weyl Semimetal in a Topological Insulator Multilayer, Phys. Rev. Lett. **107**, 127205 (2011).

[36] F. Kirtschig, J. van den Brink, and C. Ortix, Surface-state spin textures in strained bulk HgTe: Strain-induced topological phase transitions, Phys. Rev. B **94**, 235437 (2016).

[37] A. M. Kadykov, S. S. Krishtopenko, B. Jouault, W. Desrat, W. Knap, S. Ruffenach, C. Consejo, J. Torres, S. V. Morozov, N. N. Mikhailov, S. A. Dvoretskii, and F. Teppe, Temperature-Induced Topological Phase Transition in HgTe Quantum Wells, Phys. Rev. Lett. **120**, 086401 (2018).

[38] D. M. Mahler, J.-B. Mayer, P. Leubner, L. Lunczer, D. Di Sante, G. Sangiovanni, R. Thomale, E. M. Hankiewicz, H. Buhmann, C. Gould, and L. W. Molenkamp, Interplay of Dirac Nodes and Volkov-Pankratov Surface States in Compressively Strained HgTe, Phys. Rev. X **9**, 031034 (2019).

[39] D. M. Mahler, V. L. Müller, C. Thienel, J. Wiedenmann, W. Beugeling, H. Buhmann, and L. W. Molenkamp, Massive and topological surface states in tensile-strained HgTe, Nano Lett. **21**, 9869 (2021).

[40] C. Brüne, C.-F. X. Liu, E. G. Novik, E. M. Hankiewicz, H. Buhmann, Y. L. Chen, X. L. Qi, Z. X. Shen, S. C. Zhang, and L. W. Molenkamp, Quantum Hall Effect from the Topological Surface States of Strained Bulk HgTe, Phys. Rev. Lett. **106**, 126803 (2011).

[41] D. A. Kozlov, D. Bauer, J. Ziegler, R. Fischer, M. L. Savchenko, Z. D. Kvon, N. N. Mikhailov, S. A. Dvoretsky, and D. Weiss, Probing Quantum Capacitance in a 3D Topological Insulator, Phys. Rev. Lett. **116**, 166802 (2016).

[42] J. Ruan, S.-K. Jian, H. Yao, H. Zhang, S.-C. Zhang, and D. Xing, Symmetry-protected ideal Weyl semimetal in HgTe-class materials, Nat. Commun. **7**, 11136 (2016).

[43] G. Grabecki, J. Wróbel, M. Czapkiewicz, Ł. Cywiński, S. Gierałtowska, E. Guziewicz, M. Zholudev, V. Gavrilenko, N. N. Mikhailov, S. A. Dvoretsky, F. Teppe, W. Knap, and T. Dietl, Nonlocal resistance and its fluctuations in microstructures of band-inverted HgTe/(Hg,Cd)Te quantum wells, Phys. Rev. B **88**, 165309 (2013).

[44] C. Autieri, C. Śliwa, R. Islam, G. Cuono, and T. Dietl, Momentum-resolved spin splitting in Mn-doped trivial CdTe and topological HgTe semiconductors, Phys. Rev. B **103**, 115209 (2021).

[45] C. Śliwa, C. Autieri, J. A. Majewski, and T. Dietl, Superexchange dominates in magnetic topological insulators, Phys. Rev. B **104**, L220404 (2021).

[46] G. Dresselhaus, Spin-orbit coupling effects in zinc blende structures, Phys. Rev. **100**, 580 (1955).

[47] C.-Y. Moon and S.-H. Wei, Band gap of Hg chalcogenides: Symmetry-reduction-induced band-gap opening of materials with inverted band structures, Phys. Rev. B **74**, 045205 (2006).

[48] A. Svane, N. E. Christensen, M. Cardona, A. N. Chantis, M. van Schilfgaarde, and T. Kotani, Quasiparticle band structures of β-HgS, HgSe, and HgTe, Phys. Rev. B **84**, 205205 (2011).

[49] M. Cardona, A fine point on topological insulators, Phys. Today **63**, 10 (2010).

[50] J. P. Perdew, K. Burke, and M. Ernzerhof, Generalized Gradient Approximation Made Simple, Phys. Rev. Lett. **77**, 3865 (1996).

[51] C. Autieri and B. Sanyal, Unusual ferromagnetic YMnO$_3$ phase in YMnO$_3$/La$_{2/3}$Sr$_{1/3}$MnO$_3$ heterostructures, New J. Phys. **16**, 113031 (2014).

[52] C. Autieri, M. Cuoco, and C. Noce, Collective properties of eutectic ruthenates: Role of nanometric inclusions, Phys. Rev. B **85**, 075126 (2012).

[53] S. Roy, C. Autieri, B. Sanyal, and T. Banerjee, Interface control of electronic transport across the magnetic phase transition in SrRuO$_3$/SrTiO$_3$ heterointerface, Sci. Rep. **5**, 15747 (2015).

[54] A. Paul, C. Reitinger, C. Autieri, B. Sanyal, W. Kreuzpaintner, J. Jutimoosik, R. Yimnirun, F. Bern, P. Esquinazi, P. Korelis, and P. Böni, Exotic exchange bias at epitaxial ferroelectric-ferromagnetic interfaces, Appl. Phys. Lett. **105**, 022409 (2014).

[55] S. Hausmann, J. Ye, T. Aoki, J.-G. Zheng, J. Stahn, F. Bern, B. Chen, C. Autieri, B. Sanyal, P. D. Esquinazi, P. Böni, and A. Paul, Atomic-scale engineering of ferroelectric-ferromagnetic interfaces of epitaxial perovskite films for functional properties, Sci. Rep. **7**, 10734 (2017).

[56] T. C. van Thiel, J. Fowlie, C. Autieri, N. Manca, M. Šiškins, D. Afanasiev, S. Gariglio, and A. D. Caviglia, Coupling lattice instabilities across the interface in ultrathin oxide heterostructures, ACS Materials Lett. **2**, 389 (2020).

[57] T. C. van Thiel, W. Brzezicki, C. Autieri, J. R. Hortensius, D. Afanasiev, N. Gauquelin, D. Jannis, N. Janssen, D. J. Groenendijk, J. Fatermans, S. Van Aert, J. Verbeeck, M. Cuoco, and A. D. Caviglia, Coupling Charge and Topological Reconstructions at Polar Oxide Interfaces, Phys. Rev. Lett. **127**, 127202 (2021).

[58] L. Du, I. Knez, G. Sullivan, and R.-R. Du, Robust helical edge transport in gated InAs/GaSb bilayers, Phys. Rev. Lett. **114**, 096802 (2015).

[59] S. Yang, D. Dardzinski, A. Hwang, D. I. Pikulin, G. W. Winkler, and N. Marom, First-principles feasibility assessment of a topological insulator at the InAs/GaSb interface, Phys. Rev. Materials **5**, 084204 (2021).

[60] J. Ruan, S.-K. Jian, D. Zhang, H. Yao, H. Zhang, S.-C. Zhang, and D. Xing, Ideal Weyl semimetals in the chalcopyrites CuTlSe$_2$, AgTlTe$_2$, AuTlTe$_2$, and ZnPbAs$_2$, Phys. Rev. Lett. **116**, 226801 (2016).

[61] Y. Qian, J. Gao, Z. Song, S. Nie, Z. Wang, H. Weng, and Z. Fang, Weyl semimetals with S_4 symmetry, Phys. Rev. B **101**, 155143 (2020).

[62] J. Gao, Y. Qian, S. Nie, Z. Fang, H. Weng, and Z. Wang, High-throughput screening for Weyl semimetals with S_4 symmetry, Sci. Bull. **66**, 667 (2021).

[63] Y.-M. Xie, X.-J. Gao, X. Y. Xu, C.-P. Zhang, J.-X. Hu, J. Z. Gao, and K. T. Law, Kramers nodal line metals, Nat. Commun. **12** (2021).

[64] G. Cuono, F. Forte, M. Cuoco, R. Islam, J. Luo, C. Noce, and C. Autieri, Multiple band crossings and Fermi surface topology: Role of double nonsymmorphic symmetries in MnP-type crystal structures, Phys. Rev. Materials **3**, 095004 (2019).

[65] See Fig. 1 of Supplemental Material of Ref. [42].

[66] A. Lau, K. Koepernik, J. van den Brink, and C. Ortix, Generic Coexistence of Fermi Arcs and Dirac Cones on the Surface of Time-Reversal Invariant Weyl Semimetals, Phys. Rev. Lett. **119**, 076801 (2017).

[67] H. F. Yang, L. X. Yang, Z. K. Liu, Y. Sun, C. Chen, H. Peng, M. Schmidt, D. Prabhakaran, B. A. Bernevig, C. Felser, B. H.

Yan, and Y. L. Chen, Topological Lifshitz transitions and Fermi arc manipulation in Weyl semimetal NbAs, Nat. Commun. **10**, 3478 (2019).

[68] A. S. Wadge, B. J. Kowalski, C. Autieri, P. Iwanowski, A. Hruban, N. Olszowska, M. Rosmus, J. Kołodziej, and A. Wiśniewski, Topological Lifshitz transition in Weyl semimetal NbP decorated with heavy elements, arXiv:2202.06061 [cond-mat.mtrl-sci].

[69] C.-X. Liu, X.-L. Qi, H. Zhang, X. Dai, Z. Fang, and S.-C. Zhang, Model Hamiltonian for topological insulators, Phys. Rev. B **82**, 045122 (2010).

[70] G. Hussain, G. Cuono, R. Islam, A. Trajnerowicz, J. Jureńczyk, C. Autieri, and T. Dietl, Electronic and optical properties of inas/inas$_{0.625}$sb$_{0.375}$ superlattices and their application to far-infrared detectors, arXiv:2203.06028.

[71] C. Ortix, J. W. F. Venderbos, R. Hayn, and J. van den Brink, Absence of helical surface states in bulk semimetals with broken inversion symmetry, Phys. Rev. B **89**, 121408(R) (2014).

[72] S. Zaheer, S. M. Young, D. Cellucci, J. C. Y. Teo, C. L. Kane, E. J. Mele, and A. M. Rappe, Spin texture on the Fermi surface of tensile-strained HgTe, Phys. Rev. B **87**, 045202 (2013).

[73] R. Ma, D. N. Sheng, and L. Sheng, Three-dimensional quantum Hall effect and magnetothermoelectric properties in Weyl semimetals, Phys. Rev. B **104**, 075425 (2021).

[74] J. Płachta, E. Grodzicka, A. Kaleta, S. Kret, L. T. Baczewski, A. Pietruczik, M. Wiater, M. Goryca, T. Kazimierczuk, P. Kossacki, G. Karczewski, T. Wojtowicz, and P. Wojnar, Magnetic field induced mixing of light hole excitonic states in (Cd,Mn)Te/(Cd,Mg)Te core/shell nanowires, Nanotechnology **29**, 205205 (2018).

[75] J. Hajer, M. Kessel, C. Brüne, M. P. Stehno, H. Buhmann, and L. W. Molenkamp, Proximity-induced superconductivity in CdTe-HgTe core-shell nanowires, Nano Lett. **19**, 4078 (2019).

[76] C. Betthausen, P. Giudici, A. Iankilevitch, C. Preis, V. Kolkovsky, M. Wiater, G. Karczewski, B. A. Piot, J. Kunc, M. Potemski, T. Wojtowicz, and D. Weiss, Fractional quantum Hall effect in a dilute magnetic semiconductor, Phys. Rev. B **90**, 115302 (2014).

[77] S. Shamim, W. Beugeling, J. Böttcher, P. Shekhar, A. Budewitz, P. Leubner, L. Lunczer, E. M. Hankiewicz, H. Buhmann, and L. W. Molenkamp, Emergent quantum Hall effects below 50 mT in a two-dimensional topological insulator, Sci. Adv. **6**, eaba4625 (2020).

[78] M. Kessel, J. Hajer, G. Karczewski, C. Schumacher, C. Brüne, H. Buhmann, and L. W. Molenkamp, CdTe-HgTe core-shell nanowire growth controlled by RHEED, Phys. Rev. Materials **1**, 023401 (2017).

[79] J. Hajer, W. Mantei, M. Kessel, C. Brüne, S. Wenner, A. T. J. van Helvoort, H. Buhmann, and L. W. Molenkamp, Selective area grown ZnTe nanowires as the basis for quasi-one-dimensional CdTe-HgTe multishell heterostructures, Phys. Rev. Materials **4**, 066001 (2020).

[80] R. Islam, B. Ghosh, G. Cuono, A. Lau, W. Brzezicki, A. Bansil, A. Agarwal, B. Singh, T. Dietl, and C. Autieri, Topological states in superlattices of HgTe-class materials, 2022, doi: 10.5281/zenodo.6337978.

[81] G. Kresse and J. Furthmüller, Efficient iterative schemes for ab initio total-energy calculations using a plane-wave basis set, Phys. Rev. B **54**, 11169 (1996).

[82] F. Tran and P. Blaha, Accurate Band Gaps of Semiconductors and Insulators with a Semilocal Exchange-Correlation Potential, Phys. Rev. Lett. **102**, 226401 (2009).

[83] A. A. Mostofi, J. R. Yates, Y.-S. Lee, I. Souza, D. Vanderbilt, and N. Marzari, wannier90: A tool for obtaining maximally-localised Wannier functions, Comput. Phys. Commun. **178**, 685 (2008).

[84] QuanSheng Wu, ShengNan Zhang, H.-F. Song, M. Troyer, and A. A. Soluyanov, Wanniertools: An open-source software package for novel topological materials, Comput. Phys. Commun. **224**, 405 (2018).

[85] M. P. L. Sancho, J. M. L. Sancho, J. M. L. Sancho, and J. Rubio, Highly convergent schemes for the calculation of bulk and surface Green functions, J. Phys. F **15**, 851 (1985).

[86] C. Autieri, P. Barone, J. Sławińska, and S. Picozzi, Persistent spin helix in rashba-dresselhaus ferroelectric CsBiNb$_2$O$_7$, Phys. Rev. Materials **3**, 084416 (2019).

3.3 PAPER II : Tunable spin polarization and electronic structure of bottom-up synthesized MoSi$_2$N$_4$ materials

The exciting topic of 2D materials, with extraordinarily rich physics and unique technology applications, has been made possible by the discovery of graphene and other atomic-thick crystalline materials[101–108]. Recent reports have described the first chemical vapour deposition synthesis of a 2D synthetic vdW material, MoSi2N4 [109–111]. This new way of making thin films from the bottom up is a important step forward in making 2D materials.

In this work, I explore spin-dependent electronic structures of ultra-thin films of recently introduced 2D synthetic materials MSi$_2$Z$_4$ (M = Mo or W and Z = N or As) in 2H phase, first-principles modeling of layer-dependent stability and valleytronic properties of MoSi$_2$N$_4$ 2D materials. The MSi2N4 monolayers are indirect bandgap semiconductors with a large spin-split state at K and K$'$. The monolayer lacks inversion symmetry, so it shows a 100% spin-polarization at K and K$'$ and the bands with opposite spin orientation are locked at K and K$'$ respectively, due to the presence of time reversal symmetry. In contrast of the K-points the bands at Γ & M are double degenerate. Once we consider a bilayer, the inversion symmetry is preserved, and as a consequence, the bands are double degenerate and the net spin polarization of the materials is zero. The applied electric field has the potential to tune the spin polarization; the presence of the electric field creates a charge imbalance that breaks local inversion symmetry, pushing the bands of the second layer downward if the electric field is positive and upward if the electric field is negative. The separation between spin up and spin down of same layer is known as Δ_{intra}, which is almost constant under the influence of external electric field. The Δ_{intra} is the splitting same as the spin-orbit coupling of the materials. Whereas the Δ_{inter}, which represents the separation of spin up and spin down between the layers, increases linearly. Furthermore, I demonstrate that the bulk of 2H-MoSi$_2$N$_4$, like the monolayer and bilayer, is thermodynamically stable. It is possible to grow a 3D counterpart of 2H-MoSi$_2$Z$_4$ compound using bottom-up synthesis methods. The bandgap decreases as the number of layers increases, and they reach the bulk gap after 8 monolayers, but the nature of the bandgap remains the same (i.e., indirect bandgap). Similarly, the spin polarization starts decreasing exponentially with an increasing odd number of layers; it is zero for an even number of layers as it restores the inversion symmetry. Finally, it is noticed that the nature of bandgap changed from indirect to direct, changing Z: N to As. The monolayer, bilayer and bulk of MSi$_2$Z$_4$ materials are thermodynamically stable. We have demonstrated the MSi$_2$Z$_4$ materials are a fantastic materials platform for the valleytronics, optoelectronics, and Qunatum technology.

Tunable spin polarization and electronic structure of bottom-up synthesized MoSi$_2$N$_4$ materials

Rajibul Islam,[1,*] Barun Ghosh,[2,3,*] Carmine Autieri ●,[1] Sugata Chowdhury,[4] Arun Bansil,[3]
Amit Agarwal,[2] and Bahadur Singh ●[5,†]

[1]*International Research Centre MagTop, Institute of Physics, Polish Academy of Sciences,
Aleja Lotnikow 32/46, PL-02668 Warsaw, Poland*
[2]*Department of Physics, Indian Institute of Technology, Kanpur 208016, India*
[3]*Department of Physics, Northeastern University, Boston, Massachusetts 02115, USA*
[4]*Department of Physics and Astronomy and IBM-HBCU Quantum Center, Howard University, Washington, DC 20059, USA*
[5]*Department of Condensed Matter Physics and Materials Science, Tata Institute of Fundamental Research, Mumbai 400005, India*

Manipulation of spin-polarized electronic states of two-dimensional (2D) materials under ambient conditions is necessary for developing new quantum devices with small physical dimensions. Here, we explore spin-dependent electronic structures of ultra-thin films of recently introduced 2D synthetic materials MSi$_2$Z$_4$ (M = Mo or W and Z = N or As) using first-principles modeling. Stacking of MSi$_2$Z$_4$ monolayers is found to generate dynamically stable bilayer and bulk materials with thickness-dependent properties. When spin-orbit coupling (SOC) is included in the computations, MSi$_2$N$_4$ monolayers display indirect band gaps and large spin-split states at the K and K' symmetry points at the corners of the Brillouin zone with nearly 100% spin polarization. The spins are locked in opposite directions along an out-of-the-plane direction at K and K', leading to spin-valley coupling effects. As expected, spin polarization is absent in the pristine bilayers due to the presence of inversion symmetry, but it can be induced via an external out-of-plane electric field much like the case of Mo(W)S$_2$ bilayers. A transition from an indirect to a direct band gap can be driven by replacing N by As in MSi$_2$(N, As)$_4$ monolayers. Our study indicates that the MSi$_2$Z$_4$ materials can provide a viable alternative to the MoS$_2$ class of 2D materials for valleytronics and optoelectronics applications.

DOI: 10.1103/PhysRevB.104.L201112

Introduction. Since the isolation of two-dimensional (2D) graphene from its parent graphite in 2004 [1–3], a variety of atomically thin materials have been exfoliated from bulk layered compounds with electronic states that encompass insulators to semiconductors to semimetals/metals. Prominent examples include hexagonal boron nitride [4], 2D transition-metal dichalcogenides (TMDs) [5–12], phosphorene [13,14], and MXenes [15], among other materials [16]. These 2D materials offer exciting opportunities for exploring novel electronic, excitonic, correlated, and topological states under 2D charge confinement for spintronics, valleytronics, and optoelectronics applications and developing materials platforms for high-density devices with minimal physical dimensions. Stacking, twisting, and straining of such 2D layers to form moiré superlattices and heterostructures brings unprecedented possibilities for tailoring properties [16–23]. A common approach for obtaining 2D materials is exfoliation from appropriate 3D layered materials using a top-to-bottom approach. Finding new 2D materials without parental analogs would provide a new paradigm for engineering states with diverse functionalities and offer new pathways for designing synthetic materials with desirable properties [16–23].

Among the methods of growing materials in a bottom-up approach is the use of a substrate with strong adatom adhesion. This method has shown success in synthesizing atomically thin films such as silicene [24], germanene [25], bismuthene [26], and borophene [27]. The stability and morphology of such materials are, however, strongly dependent on growth conditions due to the presence of dangling bonds of adatoms that either reorganize to generate complicated surface morphologies or get oxidized when exposed to air [28]. An alternate route proposed recently involves passivation of the high-energy surfaces of materials with elements that can generate synthetic layered 2D materials [29,30]. By passivating nonlayered molybdenum nitride with elemental silicon during chemical vapor deposition growth, large area (15 mm × 15 mm) layered 2D MoSi$_2$N$_4$ materials were synthesized. Importantly, MoSi$_2$N$_4$ shows remarkable properties such as stability under ambient conditions, a semiconducting behavior, and high mobility of 270/1200 cm^{2}V^{-1}s^{-1}, which is better than that of the widely used MoS$_2$ class of 2D materials [29–32]. MoSi$_2$N$_4$ and its derivative monolayers host gapped states in a pair of valleys located at the corners of the hexagonal Brillouin zone (BZ) [33–35]. Due to the breaking of the spatial inversion symmetry, the spin states in these monolayers become separated in energy and give rise to unique spin-valley couplings in the vicinity of the Fermi level and valley-contrasting Berry curvatures and orbital magnetic moments, which could potentially enable wide-ranging valleytronics and optoelectronics applications [36–42]. Despite the excellent stability of synthetic MoSi$_2$N$_4$ monolayers under ambient conditions, it is not clear how their properties evolve

in the multilayer and bulk of these bottom-up grown 2D van der Waals (vdW) materials.

Motivated by the new opportunities offered by a bottom-up approach, here we report layer-dependent stability and valleytronic properties of $M\text{Si}_2\text{Z}_4$ (M = Mo or W, and Z = N or As) materials. Using density-functional-theory based first-principles modeling, we show that the MoSi_2N_4 materials are dynamically stable up to the bulk limit. The monolayers are found to exhibit large spin-split states at the BZ corners K and K' with nearly 100% spin polarization, similar to the MoS_2 materials class. As expected, the spin splitting is zero in the bilayer films as the inversion symmetry is restored. However, spin-splitting can be switched on and manipulated in the bilayers via an out-of-plane electric field. An indirect to direct band gap transition in $M\text{Si}_2\text{Z}_4$ is driven by the replacement of N by As. In addition to highlighting the unique thickness-dependent properties of $M\text{Si}_2\text{Z}_4$, our study demonstrates the value of a bottom-up approach for synthesizing viable 3D bulk materials based on synthetic 2D vdW materials.

Methods. Electronic structure calculations were performed within the density functional theory (DFT) framework using the Vienna Ab initio Simulation Package (VASP) [43,44]. The projector augmented wave (PAW) pseudopotentials were used with the generalized-gradient approximation (GGA) [45] for treating exchange-correlation effects. A plane-wave cutoff of 500 eV was used in all calculations. Surface BZ integrations were performed using a $10\times10\times1$ Monkhorst-pack k grid. Effects of spin-orbit coupling (SOC) were included self-consistently. The structural parameters were optimized until the residual forces on each atom became less than 10^{-4} eV/Å, and these optimized parameters were used in the calculations. An energy tolerance of 10^{-8} eV was used. The thin-film calculations were performed using a slab geometry with a vacuum layer of 20 Å to eliminate spurious interactions between the periodically repeated 2D layers. Phonon dispersion curves were obtained within the density functional perturbation theory (DFPT) framework using PHONOPY code [46] with a $4\times4\times1$ supercell. The robustness of our GGA-based results was assessed using the optPBE-vdW correlation functional [47–51] as well as the more advanced HSE hybrid functional [52], see Supplemental Material (SM) [53] for details. PYPROCAR [54] and PYMATGEN [55] packages were used for band structure illustrations.

Crystal structure and dynamical stability of MoSi_2N_4. Monolayer MoSi_2N_4 crystallizes in the hexagonal lattice with space group D_{3h}^1 ($P\bar{6}m2$, No. 187). It involves strongly bonded, seven-layer stacking in the order N-Si-N-Mo-N-Si-N that can be viewed as a sandwich involving an MoN_2 layer and two Si-N bilayers [Figs. 1(a)–1(e)]. This structure preserves trigonal C_{3v} and $M_z(z \to -z)$ mirror-plane symmetries but breaks the inversion symmetry. The monolayers can be stacked in the -A-B-A- order to realize a 2H bilayer structure similar to that of MoS_2. Unlike the monolayer, bilayer MoSi_2N_4 realizes the higher-symmetry group D_{6h}^4 ($P6_3/mmc$, No. 194) [29,56], restoring the spatial center of inversion, which is marked by the red dot in Fig. 1(b). The equilibrium interlayer distance (d_0) between the Mo_1 and Mo_2 sublayers in the bilayer is found to be 10.65 Å. Notably, the 2H-bilayer structure can be repeated to realize the bulk MoSi_2N_4 materials like the
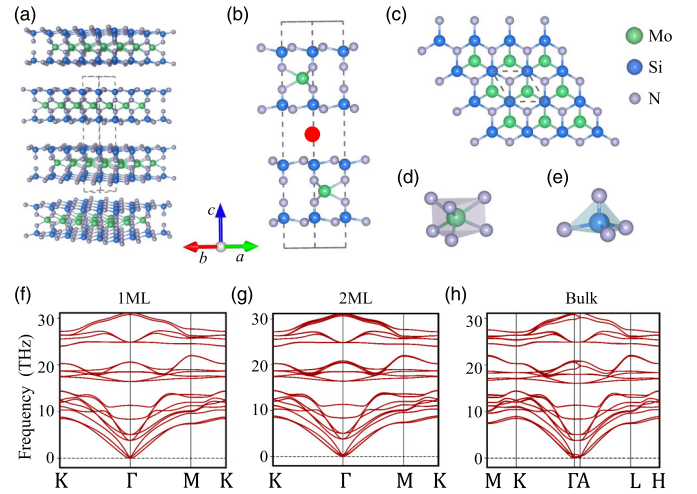

FIG. 1. Atomic arrangement of (a) four and (b) two layers of MoSi_2N_4 with AB stacking. The dashed box identifies the bulk unit cell of 2H-MoSi_2N_4. The red dot in the middle of the van der Waals gap in (b) marks the spatial center of inversion, which is absent in the monolayer. (c) Top view of monolayer MoSi_2N_4. (d) Mo-N trigonal and (e) Si-N tetrahedral local coordination structures in MoSi_2N_4 monolayers. The calculated phonon dispersion of (f) monolayer (1ML), (g) bilayer (2ML), and (h) bulk MoSi_2N_4.

transition metal dichalcogenides. The optimized structural parameters and Wyckoff positions for bulk $M\text{Si}_2\text{Z}_4$ are listed in Table I.

In order to showcase the stability of the monolayer and multilayer MoSi_2N_4 films, we present the associated phonon dispersions in Figs. 1(f)–1(h). The absence of imaginary phonon frequencies in the entire hexagonal BZ confirms the dynamical stability of these structures. Notably, the bulk phonon spectrum also lacks imaginary phonon frequencies. Our computations in which van der Waals interactions beyond the GGA are included yield similar results and affirm the robustness of our conclusions concerning the stability in all cases [53]. We thus infer that stable 3D bulk of MoSi_2N_4 can be realized experimentally [57].

Spin-resolved electronic structure of monolayer MoSi_2N_4. The orbitally resolved band structure of monolayer MoSi_2N_4

TABLE I. Calculated lattice parameters for 2H-bulk MoSi_2N_4, MoSi_2As_4, WSi_2N_4, and WSi_2As_4 using the GGA and optPBE-VDW density functionals. a and c are the hexagonal lattice constants and u_{Si}, $u_{\text{N/As}}$, and $v_{\text{N/As}}$ are the internal parameters associated with Wyckoff positions $4e$ $(0, 0, u_{\text{Si}})$, $4f$ $(\frac{1}{3}, \frac{2}{3}, u_{\text{N/As}})$, and $4e$ $(0, 0, v_{\text{N/As}})$, respectively. The subscripts identify the atoms.

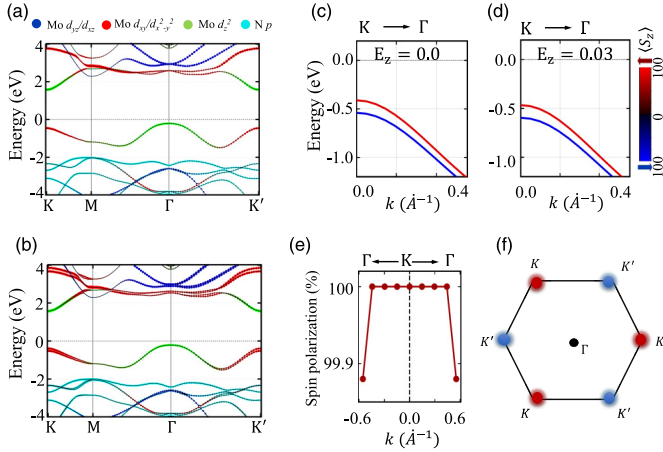|		a (Å)	c (Å)	u_{Si}	$u_{\text{N/As}}$	$v_{\text{N/As}}$	E_g (eV)
MoSi_2N_4	GGA	2.910	21.311	0.1095	0.1915	0.0859	1.655
	vdW	2.932	20.772	0.1045	0.1889	0.0804	1.665
MoSi_2As_4	GGA	3.622	27.617	0.1106	0.1960	0.0703	0.508
	vdW	3.681	27.408	0.1079	0.1950	0.0670	0.447
WSi_2N_4	GGA	2.914	21.439	0.1099	0.1914	0.0865	1.970
	vdW	2.935	20.763	0.1043	0.1888	0.0805	1.985
WSi_2As_4	GGA	3.628	27.940	0.1121	0.1967	0.0723	0.207
	vdW	3.685	27.397	0.1079	0.1952	0.0672	0.208

FIG. 2. Orbitally resolved band structure of monolayer MoSi$_2$N$_4$ (a) without and (b) with spin-orbit coupling (SOC). Spin-resolved bands around K along the Γ-K direction for (c) $E_z = 0$ eV/Å and (d) $E_z = 0.03$ eV/Å with SOC. The color bar in (d) denotes the degree (in percent) of spin polarization. (e) Spin-polarization decay profile of the states at the top of the valence band around the K point. Large spin polarization (>99.9%) persists over a wide momentum range along the Γ-K direction. (f) Schematic representation of spin-valley locking in monolayer MoSi$_2$N$_4$. Red (blue) color represents spin pointing out of (into) the plane.

FIG. 3. (a) Band structure of bilayer MoSi$_2$N$_4$ in the absence of external electric field ($E_z = 0$). (b) Same as (a) but for $E_z = 0.03$ eV/Å. Spin splitting in the band structure is evident. (c) Evolution of the top four valence bands around the K point with varying external electric field strength. The color scale gives the degree (in percent) of spin-polarization of the bands. Markings 1 and 2 identify the doublets associated with the first and second layers of the bilayer. (d) Degree of spin-splitting at the K point as a function of E_z. Blue (red) markers show the intralayer (interlayer) Δ_{intra} (Δ_{inter}) components of the spin splitting. (e) A schematic of the electric-field effect on the bilayer band structure.

without SOC is presented in Fig. 2(a). An indirect band gap of 1.778 eV is obtained between the valence band maximum (VBM) and conduction band minimum (CBM), which are located at the Γ and K/K' points, respectively. The energy difference, $\Delta_{\Gamma K}$, between the top of the valence bands at the Γ and K/K' points is 322 meV, and it can be tuned by strain to realize a direct band gap at the K/K' point [33]. The Bloch wave functions at the VBM and CBM edges are composed of d_{z^2} states of the Mo atoms. All states remain twofold spin degenerate without the SOC as seen in Fig. 2(a). When SOC is included, the top of the valence bands displays a large spin-splitting of 129 meV at K due to the broken spatial inversion symmetry. [Since K is not a time-reversal invariant momentum (TRIM) point, the spin-split states at K are not twofold degenerate.] In contrast, the bands at the Γ and M points remain twofold spin degenerate as they are TRIM points [see Figs. 2(b) and 2(c)]. The indirect nature of the monolayer band gap, however, remains preserved with a value of 1.775 eV (2.342 eV) with GGA (HSE).

Our analysis reveals that the two spin-split states at K have nearly 100% out-of-plane (S_z) spin polarization. This can be attributed to the presence of the horizontal mirror plane M_z in monolayer MoSi$_2$N$_4$ that ensures that the S_x and S_y components of spin are zero. The spin-split states at K and K' are oppositely polarized since they form a Kramers pair obeying the time-reversal symmetry constraint $E(\vec{k}, \uparrow) = E(-\vec{k}, \downarrow)$. Figure 2(d) shows the evolution of the degree of spin-polarization of states at the top of the valence band as we go away from the K point. Spin polarization decreases slightly to 99.9% for the change a momentum $\Delta k = 0.553$ Å^{-1} (~38% of the Γ-K distance), demonstrating its robustness. The spin texture of the state at the top of the valence band in the hexagonal BZ is shown schematically in Fig. 2(f). The preceding
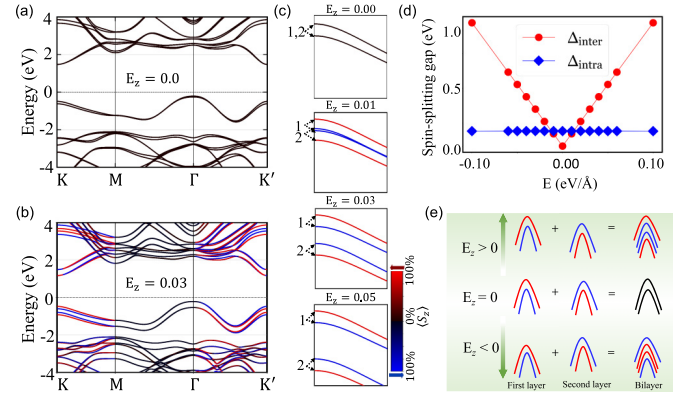
spin behavior is indicative of spin-valley locking in MoSi$_2$N$_4$ monolayers, which is similar to that observed previously in the TMDs [11].

We emphasize that the Zeeman-type out-of-plane spin polarization in the vicinity of K points in the MoSi$_2$N$_4$ monolayer is tied to the crystal structure of the film, and therefore it cannot be destroyed or manipulated with an out-of-plane electric field E_z. We have verified this property by calculating the spin-resolved band structure in the presence of an external electric field applied perpendicular to the monolayer. Figure 2(d) shows the results for $E_z = 0.03$ eV/Å. Both the spin-splitting and spin-polarization features are seen to be retained.

Tuning spin-structure of bilayer MoSi$_2$N$_4$ *via an external electric field.* Figure 3(a) shows the band structure of bilayer MoSi$_2$N$_4$. Similar to the monolayer case, the bilayer is an indirect band gap semiconductor with the VBM and CBM edges located at the Γ and K/K' points, respectively. However, in contrast to the monolayer, the inversion symmetry is now restored and, as a result, all bands become twofold spin degenerate. A small splitting at the Γ point is driven by the interlayer interactions between the two MoSi$_2$N$_4$ layers, whereas the splitting at the K/K' points is due to the SOC. The inversion symmetry of the bilayer, however, can be broken by an out-of-plane external electric field E_z, which lifts the spin degeneracy at the non-TRIM K/K' points, allowing the manipulation of spin-split states at the top of the valence bands.

Figure 3(b) shows the spin-resolved bilayer band structure for $E_z = 0.03$ eV/Å. The spin-split states are now seen to be resolved at the K and K' points with opposite spin polarizations for the top bands. There are four spin-polarized valence bands near the Fermi level, two of which originate from the first layer whereas the other two come from the

second layer of the bilayer. Evolution of these four bands with E_z is shown in Fig. 3(c). To quantify the spin split-ting, we introduce the quantities Δ_{intra} and Δ_{inter}. Here, Δ_{intra} is defined as the energy difference between first (second) layer spin-up and first (second) layer spin-down states, while Δ_{inter} is the energy difference between the first-layer spin-up and second-layer spin-down states. Δ_{intra} thus captures the effect of the SOC on spin splitting, whereas Δ_{inter} codes the effect of the potential difference between the two lay-ers caused by the external field. When $E_z = 0.01$ eV/Å, the spin-split doublet from the second layer lies at an energy that is slightly lower than that for the first-layer doublet, so that Δ_{inter} is smaller than Δ_{intra}. The two topmost valence states are thus composed of states belonging to two differ-ent layers of the bilayer. When E_z exceeds a critical value, Δ_{inter} becomes larger than Δ_{intra} and the two topmost va-lence states arise from the same layer. Δ_{intra} and Δ_{inter} are shown as a function of E_z in Fig. 3(d). Δ_{inter} varies linearly with E_z while Δ_{intra} shows negligible field dependence. A crossover between Δ_{intra} and Δ_{inter} is observed around $E_z = 0.012$ eV/Å. Notably, the spin polarization of the topmost valence states at the K/K' points remains nearly 100% in the presence E_z.

We find that the applied electric field changes the splitting (Δ_{inter}) between the states coming from different layers in the bilayer. In contrast, as we would expect, the effect of the field on the spin-splitting as well as the degree of spin-polarization of the states coming from the same layer is negligible. Sign of the spin-polarization of states at K/K' points is electric-field-direction dependent. Evolution of the states at the K point under positive and negative field directions is shown schematically in Fig. 3(e). These results provide a clear path-way for manipulating the spin states in bilayer $MoSi_2N_4$. Electric-field-dependent evolution of the bilayer states for all the MSi_2Z_4 materials we investigated falls along the preced-ing lines. Notably, the values of the electric field required to manipulate the states here are much lower than in MoS_2 [11].

Layer-dependent states and spin polarization. We now turn to discuss the evolution of the band gap and spin-polarization of multilayer $MoSi_2N_4$. Figure 4(a) shows the calculated bulk band structure using our optimized lattice parameters (Table I). It has an indirect bandgap of 1.655 eV (2.221 eV) within the GGA (HSE). The wave functions at the CBM edge at K and the VBM edge at Γ consist of Mo d_{z^2} states similar to the monolayer and bilayer cases. The bands along the Γ-A direction remain weakly dispersive as a result of weak interlayer coupling. However, the SOC-split states can be seen at the K and H points. Evolution of the band gap as a function of the layer thickness is shown in Fig. 4(b). The band gap decreases slightly with increasing number of $MoSi_2N_4$ layers and converges to the bulk value for the eight-layer film. This insensitivity of the bandgap to layer thickness indicates that the weak van der Waal's coupling dominates the interlayer interactions in $MoSi_2N_4$.

Figure 4(c) shows the evolution of spin-polarization of valence state as a function of the number of layers. Since the films with an even number of $MoSi_2N_4$ layers are inversion symmetric, these films display zero spin-polarization. Spin-polarization in films with an odd number of layers varies as $1/N$, where N is the number of layers.
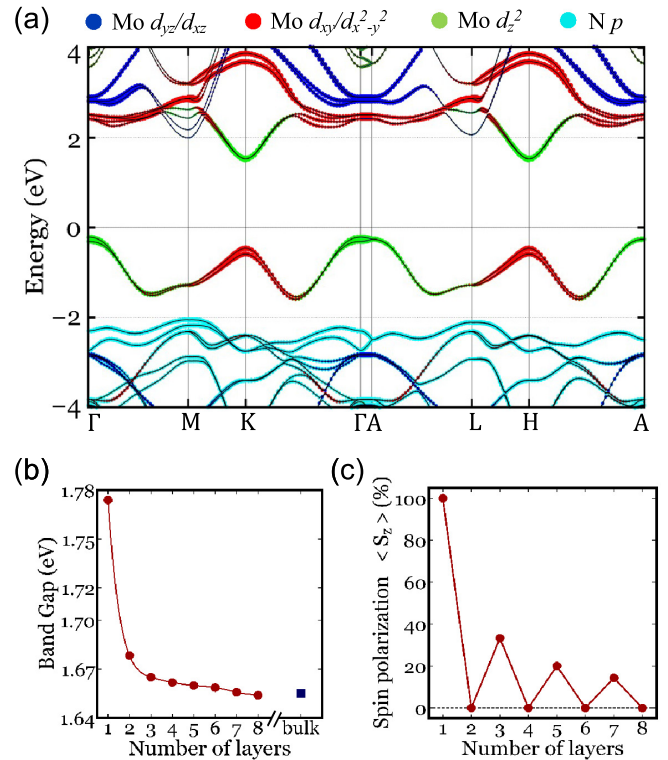

FIG. 4. (a) Orbitally resolved band structure of bulk $MoSi_2N_4$ in the bulk hexagonal Brillouin zone. (b) Band gap and (c) average spin-polarization of the top layer as a function of the number of layers.

Band structure of MSi_2Z_4 materials. We now discuss the dynamical stabilities and band structures of other MSi_2Z_4 thin films. Figures 5(a)–5(c) show the phonon spectra of mono-layer, bilayer, and bulk $MoSi_2As_4$. No imaginary branches in the BZ are found, indicating stability of these films. Band structures of $MoSi_2As_4$ films and bulk are presented in Figs. 5(d)–5(f). In contrast to $MoSi_2N_4$, the monolayer $MoSi_2As_4$ is a direct band gap semiconductor with a band gap of 0.508 eV (0.707 eV) within the GGA (HSE) at the K/K' point. The band gap is found to remain direct as the thick-ness increases from monolayer to bulk [58]. The interlayer
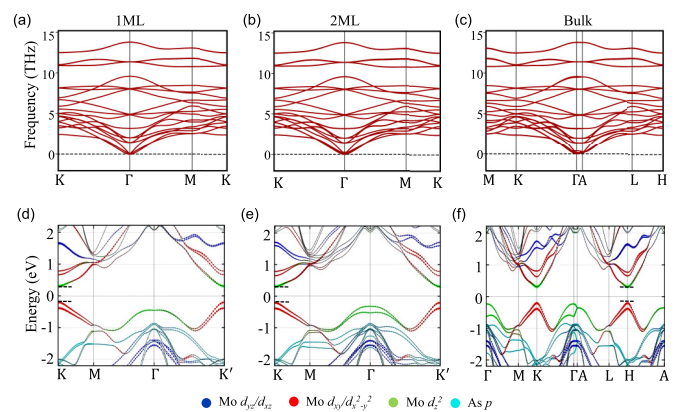

FIG. 5. Calculated phonon spectrum of (a) monolayer (1ML), (b) bilayer (2ML), and (c) bulk $MoSi_2As_4$. Orbitally decomposed band structure of (d) monolayer, (e) bilayer, and (f) bulk $MoSi_2As_4$.

coupling strength in $MoSi_2As_4$ is larger than in $MoSi_2N_4$, and the location of the direct band gap changes from the K to the H point in going to the bulk limit [Fig. 5(f)]. $MoSi_2As_4$ monolayers also host nearly 100% spin-polarized states.

The phonon spectra and orbitally resolved band structures of WSi_2N_4 and WSi_2As_4 are presented in the SM [53]. These systems are also stable up to the bulk limit and support highly spin-polarized states similar to the cases of $MoSi_2N_4$ and $MoSi_2As_4$. However, the W atoms with their stronger SOC yield increased spin splittings at the K/K' points in these materials.

Conclusion. Using first-principles modeling, we have carried out a systematic thickness-dependent investigation of the dynamical stabilities and electronic and spin-polarization properties of the MSi_2Z_4 ($M =$ Mo or W and $Z =$ N or As) compounds. These materials are found to be dynamically stable from the monolayer to the bulk limit, indicating that multilayer films and bulk of such bottom-up synthesized 2D vdW materials should be possible to realize experimentally. Our analysis reveals that the monolayers host two nearly 100% out-of-the-plane spin-polarized states at the K points in the BZ with Zeeman-type spin splittings. The spin polarization is reversed at the K' points while the high degree of spin polarization remains preserved. The spin polarization of the states in the bilayers, which is zero due to the restoration of the inversion symmetry in the pristine bilayers, can be switched on and manipulated using an external electric field. $MoSi_2N_4$ and WSi_2N_4 exhibit a robust indirect bandgap from the monolayer to the bulk limit. In contrast, $MoSi_2As_4$ and WSi_2As_4 monolayers display a direct band gap at the K/K' point, which is preserved from the monolayer to the bulk. Our study provides insight into the band gap, spin-polarization, and spin-valley locking of electronic states in MSi_2Z_4 materials class, and indicates that these materials could provide a viable materials platform as an alternative to the MoS_2 materials that are currently in common use for spintronics, valleytronics, and optoelectronics applications.

[1] K. S. Novoselov, A. K. Geim, S. V. Morozov, D. Jiang, Y. Zhang, S. V. Dubonos, I. V. Grigorieva, and A. A. Firsov, Science **306**, 666 (2004).

[2] K. S. Novoselov, A. K. Geim, S. V. Morozov, D. Jiang, M. I. Katsnelson, I. Grigorieva, S. Dubonos, and A. A. Firsov, Nature (London) **438**, 197 (2005).

[3] Y. Zhang, Y.-W. Tan, H. L. Stormer, and P. Kim, Nature (London) **438**, 201 (2005).

[4] Y. Lin, T. V. Williams, and J. W. Connell, J. Phys. Chem. Lett. **1**, 277 (2010).

[5] K. F. Mak, C. Lee, J. Hone, J. Shan, and T. F. Heinz, Phys. Rev. Lett. **105**, 136805 (2010).

[6] Q. H. Wang, K. Kalantar-Zadeh, A. Kis, J. N. Coleman, and M. S. Strano, Nat. Nanotechnol. **7**, 699 (2012).

[7] M. Chhowalla, H. S. Shin, G. Eda, L.-J. Li, K. P. Loh, and H. Zhang, Nat. Chem. **5**, 263 (2013).

[8] X. Huang, Z. Zeng, and H. Zhang, Chem. Soc. Rev. **42**, 1934 (2013).

[9] C. Tan and H. Zhang, Chem. Soc. Rev. **44**, 2713 (2015).

[10] H. Yuan, M. S. Bahramy, K. Morimoto, S. Wu, K. Nomura, B.-J. Yang, H. Shimotani, R. Suzuki, M. Toh, C. Kloc, X. Xu, R. Arita, N. Nagaosa, and Y. Iwasa, Nat. Phys. **9**, 563 (2013).

[11] T.-R. Chang, H. Lin, H.-T. Jeng, and A. Bansil, Sci. Rep. **4**, 6270 (2014).

[12] N. Morell, S. Tepsic, A. Reserbat-Plantey, A. Cepellotti, M. Manca, I. Epstein, A. Isacsson, X. Marie, F. Mauri, and A. Bachtold, Nano Lett. **19**, 3143 (2019).

[13] L. Li, Y. Yu, G. J. Ye, Q. Ge, X. Ou, H. Wu, D. Feng, X. H. Chen, and Y. Zhang, Nat. Nanotechnol. **9**, 372 (2014).

[14] H. Liu, Y. Du, Y. Deng, and D. Y. Peide, Chem. Soc. Rev. **44**, 2732 (2015).

[15] M. Naguib, V. N. Mochalin, M. W. Barsoum, and Y. Gogotsi, Adv. Mater. **26**, 992 (2014).

[16] K. Novoselov, O. A. Mishchenko, O. A. Carvalho, and A. C. Neto, Science **353** (2016).

[17] K. S. Novoselov and A. H. C. Neto, Phys. Scr. **2012**, 014006 (2012).

[18] T. Heine, Acc. Chem. Res. **48**, 65 (2015).

[19] Y. Gong, J. Lin, X. Wang, G. Shi, S. Lei, Z. Lin, X. Zou, G. Ye, R. Vajtai, B. I. Yakobson *et al.*, Nat. Mater. **13**, 1135 (2014).

[20] J. Wang, F. Ma, and M. Sun, RSC Adv. **7**, 16801 (2017).

[21] Y. Cao, V. Fatemi, S. Fang, K. Watanabe, T. Taniguchi, E. Kaxiras, and P. Jarillo-Herrero, Nature (London) **556**, 43 (2018).

[22] C. Chen, B. Singh, H. Lin, and V. M. Pereira, Phys. Rev. Lett. **121**, 226602 (2018).

[23] A. Vargas, F. Liu, C. Lane, D. Rubin, I. Bilgin, Z. Hennighausen, M. DeCapua, A. Bansil, and S. Kar, Sci. Adv. **3**, e1601741 (2017).

[24] A. Fleurence, R. Friedlein, T. Ozaki, H. Kawai, Y. Wang, and Y. Yamada-Takamura, Phys. Rev. Lett. **108**, 245501 (2012).

[25] M. E. Dávila, L. Xian, S. Cahangirov, A. Rubio, and G. L. Lay, New J. Phys. **16**, 095002 (2014).

[26] L. Cheng, H. Liu, X. Tan, J. Zhang, J. Wei, H. Lv, J. Shi, and X. Tang, J. Phys. Chem. C **118**, 904 (2014).

[27] B. Feng, O. Sugino, R.-Y. Liu, J. Zhang, R. Yukawa, M. Kawamura, T. Iimori, H. Kim, Y. Hasegawa, H. Li, L. Chen, K. Wu, H. Kumigashira, F. Komori, T.-C. Chiang, S. Meng, and I. Matsuda, Phys. Rev. Lett. **118**, 096401 (2017).

[28] C. Grazianetti, D. Chiappe, E. Cinquanta, M. Fanciulli, and A. Molle, J. Condens. Matter Phys. **27**, 255005 (2015).

[29] Y.-L. Hong, Z. Liu, L. Wang, T. Zhou, W. Ma, C. Xu, S. Feng, L. Chen, M.-L. Chen, D.-M. Sun *et al.*, Science **369**, 670 (2020).

[30] K. S. Novoselov, Natl. Sci. Rev. **7**, 1842 (2020).

[31] S. Bertolazzi, J. Brivio, and A. Kis, ACS Nano **5**, 9703 (2011).

[32] Y. Cai, G. Zhang, and Y.-W. Zhang, J. Am. Chem. Soc. **136**, 6269 (2014).

[33] S. Li, W. Wu, X. Feng, S. Guan, W. Feng, Y. Yao, and S. A. Yang, Phys. Rev. B **102**, 235435 (2020).

[34] H. Ai, D. Liu, J. Geng, S. Wang, K. H. Lo, and H. Pan, Phys. Chem. Chem. Phys. **23**, 3144 (2021).

[35] C. Yang, Z. Song, X. Sun, and J. Lu, Phys. Rev. B **103**, 035308 (2021).

[36] O. Gunawan, Y. P. Shkolnikov, K. Vakili, T. Gokmen, E. P. De Poortere, and M. Shayegan, Phys. Rev. Lett. **97**, 186404 (2006).

[37] D. Xiao, W. Yao, and Q. Niu, Phys. Rev. Lett. **99**, 236809 (2007).

[38] D. Gunlycke and C. T. White, Phys. Rev. Lett. **106**, 136806 (2011).

[39] D. Xiao, G.-B. Liu, W. Feng, X. Xu, and W. Yao, Phys. Rev. Lett. **108**, 196802 (2012).

[40] T. Cai, S. A. Yang, X. Li, F. Zhang, J. Shi, W. Yao, and Q. Niu, Phys. Rev. B **88**, 115140 (2013).

[41] X. Xu, W. Yao, D. Xiao, and T. F. Heinz, Nat. Phys. **10**, 343 (2014).

[42] C. Autieri, A. Bouhon, and B. Sanyal, Philos. Mag. **97**, 3381 (2017).

[43] G. Kresse and J. Furthmüller, Phys. Rev. B **54**, 11169 (1996).

[44] G. Kresse and D. Joubert, Phys. Rev. B **59**, 1758 (1999).

[45] J. P. Perdew, K. Burke, and M. Ernzerhof, Phys. Rev. Lett. **77**, 3865 (1996).

[46] A. Togo and I. Tanaka, Scr. Mater. **108**, 1 (2015).

[47] J. C. V. Klimeš, D. R. Bowler, and A. Michaelides, Phys. Rev. B **83**, 195131 (2011).

[48] J. Klimeš, D. R. Bowler, and A. Michaelides, J. Phys.: Condens. Matter **22**, 022201 (2009).

[49] I. Mosyagin, D. Gambino, D. G. Sangiovanni, I. A. Abrikosov, and N. M. Caffrey, Phys. Rev. B **98**, 174103 (2018).

[50] F. Conte, D. Ninno, and G. Cantele, Phys. Rev. Research **2**, 033001 (2020).

[51] D. Chakraborty, K. Berland, and T. Thonhauser, J. Chem. Theory Comput. **16**, 5893 (2020).

[52] J. Heyd, G. E. Scuseria, and M. Ernzerhof, J. Chem. Phys. **118**, 8207 (2003).

[53] See Supplemental Material at http://link.aps.org/supplemental/10.1103/PhysRevB.104.L201112 for exchange-correlation functional dependent properties of $M\mathrm{Si}_2Z_4$, layer dependent stability and band structure of WSi_2Z_4, and adhesion energy of all the studied materials.

[54] U. Herath, P. Tavadze, X. He, E. Bousquet, S. Singh, F. Munoz, and A. H. Romero, Comput. Phys. Commun. **251**, 107080 (2020).

[55] S. P. Ong, W. D. Richards, A. Jain, G. Hautier, M. Kocher, S. Cholia, D. Gunter, V. L. Chevrier, K. A. Persson, and G. Ceder, Comput. Mater. Sci. **68**, 314 (2013).

[56] H. Zhong, W. Xiong, P. Lv, J. Yu, and S. Yuan, Phys. Rev. B **103**, 085124 (2021).

[57] Notably, the thickness-dependent stability of 2D MoSi_2Z_4 materials indicates that multilayers and bulk of these materials should be possible to realize experimentally. Our results here should be contrasted with the thickness-dependent stability studies in the literature on various 2D materials synthesized using a top-to-bottom approach from a stable bulk. It is not clear *a priori* that stability in top-to-bottom synthesis ensures a similar stability in the bottom-up synthesis.

[58] The calculated HSE band structure with the optimized geometry obtained using the GGA and optPBE-vdW functional remains direct from monolayer to bulk $\mathrm{MoSi}_2\mathrm{As}_4$.

3.4 PAPER III : Switchable large-gap quantum spin Hall state in two-dimensional MSi$_2$Z$_4$ materials class

With the discovery of graphene, the field of condensed matter physics has entered the era of 2D materials. Since then, 2D materials have received considerable research interest due to the exotic and versatile electronic characteristics and rich physics they exhibit. The quantum spin Hall (QSH) phase is one such example; it appears in topologically non-trivial 2D insulators and protects helical edge states from counter-propagation due to time reversal symmetry. Spintronic devices and other energy-conserving transport applications can be improved using this electronic property of QSH insulators.

I predicted 1T$'$-MSi$_2$Z$_4$, a new thermodynamically stable phase of MSiZ$_4$ (M = Mo, W, and Z = P, and As) materials, in this work. In contrast to the trigonal prism of the 2H phase, the M atoms in 1T$'$-MSi$_2$Z$_4$ materials form an octahedron with six Z atoms. This disordered phase leads to a different M-M length, which forms the zigzag along the y-axis if periodic doubling of the cell is along the x-axis. Absence of the negative phonon mode in the phononic-bandstructure indicates it is thermodynamically stable phase,furthermore, the molecular-dynamics calculation at 300K shows an insignificant change in the free energy, which also confirms no spontaneous bond breaking of the system. The electronic bandstructure of the monolayer 1T$'$-MSi$_2$Z$_4$ phase reveals that it is a large-gap quantum spin Hall insulator; band inversion occurs near the *Gamma* point between M d-orbitals and Z p-orbitals; and the topological invariant is $\mathbb{Z}_2 = 1$. One of the important signatures of the QSH insulator is the topologically protected helical edge states, which connect the conduction and the valence bands. Using green function method implemented in wanniertools[112] code, we have calculated the edge state, and the surface projected on (010) surface shows a symmetry protected Dirac cone at the Γ point. Also, since the spin Berry curvature is mostly localized near the spin-orbit induced hybridization gap, the spin-hall conductivity of the material is high near the gap. The spin-Hall conductivity is not perfectly quantized due to the conservation of the z component of the spin (s$_z$) .Finally, we show how the electric field influences the topological phase transition: the bandgap start decreases with increasing electric field, becomes zero at a critical electric field, and increases with further electric field increases. This is a key aspect of the quantum spin Hall transistor. The synthetic MSi$_2$Z$_4$ can reduce the exfoliation related defected of other materials also it has large gap then other TMDs, Therefore, the monolayer of 1T$'$-MSi$_2$Z$_4$ could be a viable material platform for quantum information and quantum technologies.

Switchable large-gap quantum spin Hall state in the two-dimensional MSi$_2$Z$_4$ class of materials

Rajibul Islam,[1,2,*] Rahul Verma,[2] Barun Ghosh,[3] Zahir Muhammad [●],[1,4] Arun Bansil,[3]
Carmine Autieri [●],[1,5,†] and Bahadur Singh [●][2,‡]

[1]*International Research Centre MagTop, Institute of Physics, Polish Academy of Sciences, Aleja Lotników 32/46, PL-02668 Warsaw, Poland*
[2]*Department of Condensed Matter Physics and Materials Science, Tata Institute of Fundamental Research, Colaba, Mumbai 400005, India*
[3]*Department of Physics, Northeastern University, Boston, Massachusetts 02115, USA*
[4]*Hefei Innovation Research Institute, School of Microelectronics, Beihang University, Hefei 230013, People's Republic of China*
[5]*Consiglio Nazionale delle Ricerche CNR-SPIN, UOS Salerno, I-84084 Fisciano (Salerno), Italy*

Quantum spin Hall (QSH) insulators exhibit spin-polarized conducting edge states that are topologically protected from backscattering and offer unique opportunities to address fundamental science questions and device applications. Finding viable materials that host such topological states, however, remains a continuing challenge. Here, by using in-depth first-principles theoretical modeling, we predict large band gap QSH insulators in the recently synthesized bottom-up two-dimensional MSi$_2$Z$_4$ (M = Mo or W and Z = P or As) material family with $1T'$ structure. A structural distortion in the $2H$ phase drives a band inversion between the metal (Mo/W) d and p states of P/As to realize spinless Dirac states without spin-orbit coupling. When spin-orbit coupling is included, a hybridization gap as large as ∼204 meV opens up at the band-crossing points, realizing spin-polarized conducting edge states with nearly quantized spin Hall conductivity. We also show that the inverted band gap can be tuned with a vertical electric field, which drives a topological phase transition from the QSH to a trivial insulator with Rashba-like edge states. Our study identifies the two-dimensional MSi$_2$Z$_4$ material family in the $1T'$ structure as large band gap, tunable QSH insulators with protected spin-polarized edge states and large spin Hall conductivity.

I. INTRODUCTION

Following the early studies of two-dimensional (2D) materials [1–4], Kane and Mele demonstrated the existence of a quantum spin Hall (QSH) state in graphene in the presence of symmetry-allowed spin-orbit coupling (SOC) [5,6]. The QSH state features one-dimensional (1D) conducting helical edge modes in insulating bulk due to the nontrivial winding of their electronic states [5–13]. The helical edge modes carry symmetry-protected spin-polarized electronic states that hold immense potential for designing high-efficiency quantum electronic devices with low dissipation [14–16]. The QSH state has been theoretically predicted in a variety of 2D materials and quantum well structures. However, its experimental realization has so far been demonstrated only in HgTe/CdTe and InAs/GaSb quantum wells and thin films of $1T'$-WTe$_2$, HgPt$_2$Se$_3$, and Bi$_4$Br$_4$ at ultralow temperatures [17–23]. A common approach to realize the QSH state is to reduce the thickness of three-dimensional (3D) Z_2 topological insulators to drive a 3D to 2D crossover and a band inversion in the surface states. This method has successfully predicted the QSH state in thin films of Z_2 topological insulators [12,13,24–27]. The process of fine tuning quantum well structures or

manipulating film thickness to generate an inverted hybridization gap in the surface spectrum [12,13,24–31], however, can modify material properties, leading to complicated electronic structures and quenching of the quantized spin Hall conductance. It is important, therefore, to look for new strategies for designing 2D materials with large inverted band gaps in which the QSH state can survive at room temperature.

Here, we present an in-depth first-principles analysis with optimized crystal structures to demonstrate the presence of the QSH state in recently introduced 2D materials that can be realized via a bottom-up approach without parental analogs [32–34]. These synthetic 2D materials provide an emerging paradigm for engineering designer states with diverse functionalities. Specifically, 2D MoSi$_2$N$_4$ materials were synthesized by passivating high-energy surfaces of nonlayered nitrides with Si with remarkable stability under ambient conditions [34]. They show semiconducting behavior with high carrier mobility and feature spin-valley locking, gating and thickness-tunable spin polarization, and 2D magnetism and a correlation-driven quantum anomalous Hall state, among other properties depending on their compositions [35–38]. Theoretically predicted properties of these materials are reported to be superior to those of the widely used 2D transition metal dichalcogenides (TMDs) [34,35,39,40]. It is not clear, however, if these materials can form polytypic structures and realize a QSH state similar to the 2D TMDs. Here, based on our molecular dynamics simulations and phonon calculations, we predict that the $1T'$ phase of MSi$_2$Z$_4$ (M = Mo or W

_____

*rislam@magtop.ifpan.edu.pl
†autieri@magtop.ifpan.edu.pl
‡bahadur.singh@tifr.res.in

and $Z =$ P or As) is stable and realizes a QSH state via a structural distortion from the $2H$ to $1T'$ phase. Our calculated inverted band gap ($\sim$204 meV) and spin Hall conductivity (SHC; $\sim 1.3 e^2/h$) are higher than the top-to-bottom grown 2D TMDs. We also show that the QSH state of $M\mathrm{Si}_2Z_4$ can be switched off by driving a topological phase transition via an applied (vertical) electric field. Our study indicates the robust presence of a switchable QSH state in a polytypic structure of bottom-up grown 2D materials with excellent topological and spintronics properties.

II. METHODOLOGY

Electronic structure calculations were performed within the framework of the density functional theory based on the projector augmented wave method using the VASP [41,42] code. The self-consistent relativistic calculations were performed with a plane wave cutoff energy of 500 eV and a Γ-centered $6 \times 12 \times 1$ k mesh for Brillouin zone (BZ) sampling. We used the generalized gradient approximation (GGA) to include exchange-correlation effects [43]. The structural parameters were fully optimized until the residual forces on each atom were less than 0.001 eV/Å and the total energy was converged to 10^{-8} eV. For a more accurate treatment of electronic correlations, we also employed the Heyd-Scuseria-Ernzerhof (HSE) hybrid functional with 25% exact Hartree-Fock exchange [44]. Phonon dispersions were calculated with the density functional perturbation theory using the PHONOPY code [45] with a $2 \times 4 \times 1$ supercell. The *ab initio* molecular dynamics simulations were performed with a Nosé-Hoover thermostat at a constant temperature of 300 K with a time step of 2 fs [46]. We generated material-specific tight-binding Hamiltonians with M d, Si s and p, and Z p orbitals using the VASP2WANNIER interface [47], which was also used to elucidate topological properties using the WANNIERTOOLS package [48,49].

III. RESULTS AND DISCUSSION

A. Structural properties

The pristine phase of monolayer $M\mathrm{Si}_2Z_4$ belongs to the $1H$ crystal structure family of 2D materials with space group D_{3h}^1 ($P\bar{6}m2$, No. 187) [34,35]. Figure 1(a) shows the crystal lattice of $\mathrm{MoSi}_2\mathrm{P}_4$ as an exemplar system. The structure is layered along the hexagonal c axis and consists of MoP_2 layers sandwiched between two SiP layers. The Mo atoms are located at the center of the trigonal prismatic building block with six P atoms and the MoP_2 layer bonded vertically with the SiP layer [34]. In the $1T'$ phase of $\mathrm{MoSi}_2\mathrm{P}_4$ [Fig. 1(b)], the three atomic layers are locked in such a way that the position of Mo atoms is at the center of a 60° twisted trigonal prismatic building block with six P atoms. This creates the octahedral local coordination of Mo atoms with the six P atoms in the MoP_2 layer but with different Mo-Mo bond lengths to form zigzag atomic chains along the y axis and period doubling along the x axis. This structural distortion lowers the hexagonal $1H$ symmetry to $1T'$ monoclinic symmetry with space group $P2_1/m$ (No. 11) and forms a rectangular primitive unit cell, as shown in Fig. 1(b). Importantly, the $1T'$ structure possesses the inversion symmetry I, in contrast to the $1H$
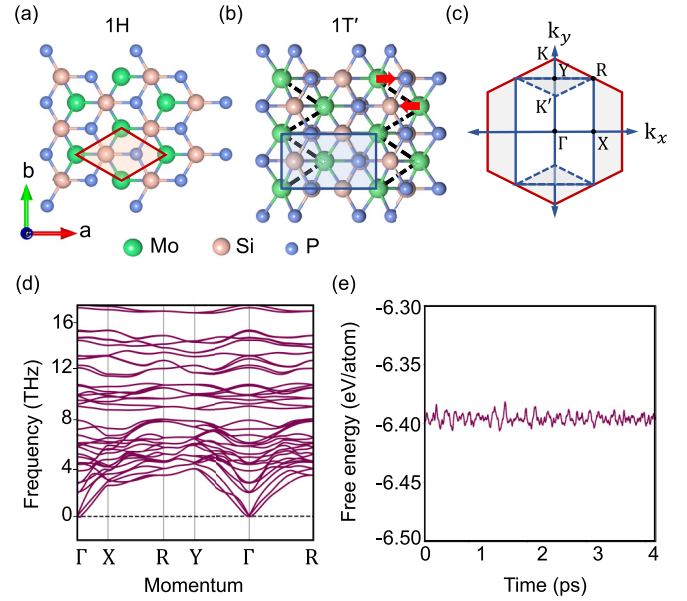

FIG. 1. Crystal structure of a $\mathrm{MoSi}_2\mathrm{P}_4$ monolayer in the (a) $1H$ and (b) $1T'$ phases. The unit cell of the $1H$ phase is indicated by the red rhombus in (a), and that of the $1T'$ phase is shown as a blue rectangle in (b). The Mo atoms are distorted from their original hexagonal positions to form 1D zigzag chains along the y axis in the $1T'$ phase, shown by dashed black lines in (b). (c) The associated 2D Brillouin zones (BZs) with high-symmetry points marked. The K points of the hexagonal BZ (red) fold onto the Γ-Y line of the $1T'$ rectangular BZ (blue). (d) Phonon dispersion in $1T'$-$\mathrm{MoSi}_2\mathrm{P}_4$. (e) Total free energy of monolayer $1T'$-$\mathrm{MoSi}_2\mathrm{P}_4$ as a function of time step during the molecular dynamics simulation at $T = 300$ K.

phase. Figure 1(c) illustrates the BZs associated with both the $1H$ and $1T'$ phases, where high-symmetry points are marked in both the pristine hexagonal and reduced rectangular BZs.

To determine the stability of polytypic structures, we present the calculated phonon dispersion of monolayer $1T'$-$\mathrm{MoSi}_2\mathrm{P}_4$ in Fig. 1(d). The absence of imaginary frequency modes throughout the BZ indicates the dynamical stability of the $1T'$ phase. The structural stability is further substantiated by performing *ab initio* molecular dynamics simulations at 300 K. Variation of the free energy as a function of the simulation time is presented in Fig. 1(e). The energy oscillates near a mean value of 6.40 eV/atom. However, the monolayer structure remains intact at the end of the simulations without any new reconstruction of the lattice, indicating thermal stability of the monolayer. We have also checked the thermodynamic stability of other members of the $1T'$-$M\mathrm{Si}_2Z_4$ family and found them to be stable (see the Supplemental Material [50]). Like the experimentally realized $1T'$ TMDs, these results indicate that $1T'$-$M\mathrm{Si}_2Z_4$ is stable and it should be possible to synthesize it experimentally under appropriate chemical, thermal, or mechanical conditions [51,52]. On comparing the total energies of the $1T'$, $1H$, and $1T$ phases of $M\mathrm{Si}_2Z_4$, we find that the $1H$ phase is the most stable, followed by the $1T'$ phase. The $1T$ phase is unstable and relaxes to the $1T'$ phase. The calculated energy difference between the $1H$ and $1T'$ phases is 55, 24, 47, and 11 meV/atom for $\mathrm{MoSi}_2\mathrm{P}_4$, $\mathrm{MoSi}_2\mathrm{As}_4$, $\mathrm{WSi}_2\mathrm{P}_4$, and $\mathrm{WSi}_2\mathrm{As}_4$, respectively. These results
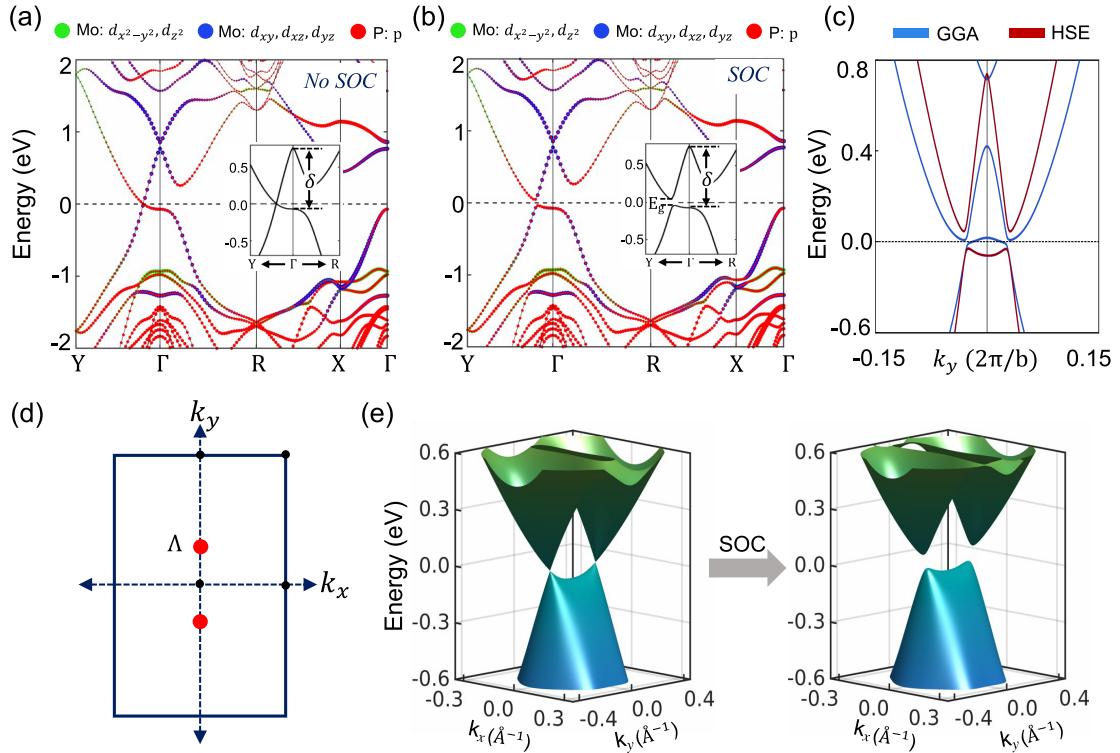
FIG. 2. Band structure of $1T'$-MoSi$_2$P$_4$ (a) without and (b) with spin-orbit coupling using the HSE hybrid functional. The horizontal dashed line marks the Fermi level. Orbital compositions of bands are shown using different colors. Insets show close-ups of bands near the Γ point at the Fermi level. The inverted band gap δ and global band gap E_g are marked. (c) Close-ups of bands obtained with HSE and GGA functionals along the Y-Γ-Y line. (d) Location of valence and conduction band crossings at the Fermi level without spin-orbit coupling in the 2D Brillouin zone. (e) E-k_x-k_y space rendition of spin-orbit-coupling-driven electronic structure crossover in monolayer $1T'$-MoSi$_2$P$_4$ with the HSE functional.

indicate that the $1T'$ phase can be realized under selective growth conditions, as has been done, for example, for the realization of the $1T'$ phase of MoS$_2$ [51,52].

B. Bulk electronic structure and band inversion

We now discuss the orbital-resolved electronic structures computed with GGA and HSE functionals to delineate the topological states of various $1T'$-MSi$_2Z_4$ compounds. Figures 2(a) and 2(b) show representative HSE band structures of $1T'$-MSi$_2Z_4$, taking MoSi$_2$P$_4$ as an example. The band structure is semimetallic with isolated spinless Dirac-type crossings in the Γ-Y directions without SOC [Fig. 2(a)]. Adding relativistic effects opens a hybridization gap at these band crossings, thereby realizing a semiconducting state with a global band gap E_g^{HSE} of 86 meV. The valence and conduction band extrema are located away from time-reversal-invariant momentum (TRIM) points at $\Lambda = \pm 0.103$ Å^{-1} [red dots in Fig. 2(d)] on the Γ-Y line, forming a camelback-like band structure near the Γ point [53,54]. Such a band structure generally points to a nontrivial topology. We find that the p states of P lie below the Mo d states with a clear band inversion at the Γ point, strong hybridization between the P and Mo states notwithstanding. This unusual orbital ordering is driven by a structural transition from $1H$ to $1T'$, which lowers the energy of the transition metal states and results in a large inverted band gap δ^{HSE} of 842 meV at the Γ point that is larger than the existing $1T'$ QSH materials.

(The inverted band gap δ refers to the energy gap between the highest occupied P p and the lowest unoccupied Mo d states at the Γ point; see Fig. 2.) The calculated electronic and structural parameters for our investigated $1T'$-MSi$_2Z_4$ materials are listed in Table I, with band structures shown in the Supplemental Material. Since monolayer $1T'$-MSi$_2Z_4$ respects inversion symmetry, we calculated the Z_2 invariant from the parity eigenvalues of the occupied states at the TRIM points and found $Z_2 = 1$ (nontrivial) in all investigated materials. We thus predict the 2D $1T'$-MSi$_2Z_4$ monolayers are QSH insulators.

We present the band structures obtained using HSE06 (red curves) and GGA (blue curves) along the Y-Γ-Y directions in Fig. 2(c) to estimate the band gap corrections in $1T'$-MSi$_2Z_4$ monolayers. The hybrid functionals are generally considered to be more accurate in estimating band bending, band order, and band gap in comparison to the GGA. While the HSE06 is seen to correct the inverted band gap at the Γ point in comparison to the GGA, the overall band structures obtained with the two functionals are topologically equivalent to a band inversion at the Γ point. Figure 2(e) considers the formation of the QSH state in $1T'$-MSi$_2Z_4$ monolayers by switching off the SOC. Specifically, the gapless band crossings are found at finite momenta along the Y-Γ-Y line at the Λ points. Switching on the SOC hybridizes these band crossings to generate the QSH state. These results imply that the band inversion in 2D $1T'$-MSi$_2Z_4$ emerges via the structural transition, while the SOC is responsible for forming the QSH state.

TABLE I. Calculated structural and electronic parameters of 2D $1T'$-MSi$_2$Z$_4$ (M = Mo or W and Z = P or As). The structural parameters include in-plane lattice constants a and b and the interatomic separations d_1 and d_2 in the transition-metal zigzag chain. The electronic parameters presented are the global band gaps obtained with GGA (E_g^{GGA}) and HSE (E_g^{HSE}) and the inverted band gaps at the Γ point calculated with GGA (δ^{GGA}) and HSE (δ^{HSE}). The topological state is indicated: QSH denotes the quantum spin Hall state. See text for details.

Material	a (Å)	b (Å)	d_1 (Å)	d_2 (Å)	Band gap (meV)		Inverted gap (meV)		Topological invariant Z_2	Topological state
					E_g^{GGA}	E_g^{HSE}	δ^{GGA}	δ^{HSE}		
MoSi$_2$P$_4$	6.141	3.430	2.945	4.194	−10.4	86.2	398	842	1	QSH
MoSi$_2$As$_4$	6.388	3.579	3.012	4.362	−39.5	109.2	391	800	1	QSH
WSi$_2$P$_4$	6.129	3.441	2.939	4.133	−23.2	198.5	712	1079	1	QSH
WSi$_2$As$_4$	6.364	3.589	2.993	4.368	−0.07	204.3	675	1058	1	QSH

C. Edge states and spin Hall conductivity

The appearance of spin-polarized edge states protected by the time-reversal symmetry is the hallmark of the QSH state. To highlight these states, we plot the calculated edge-state spectrum and the associated spin texture of MoSi$_2$P$_4$ in Fig. 3. Figure 3(a) depicts the terminated left and right edges along the y axis with schematics of the nontrivial states of our xy monolayer (x remains the periodic direction). Since the two
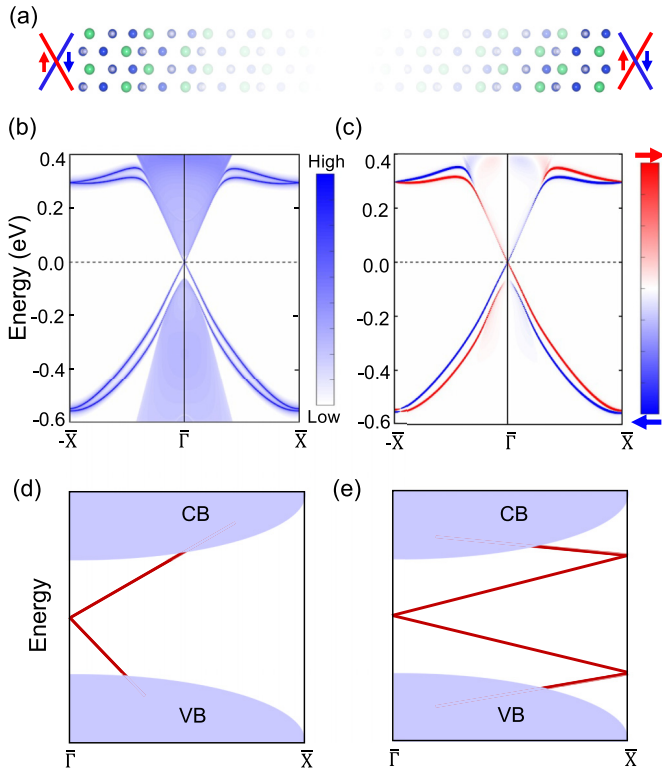

FIG. 3. (a) Lattice structure of semi-infinite one-dimensional edges of $1T'$-MoSi$_2$P$_4$. Spin-polarized edge states are shown schematically on the left and right edges. (b) Electronic spectrum of the (010) edge. Nontrivial edge states can be seen in the 2D bulk band gap. (c) Calculated left edge state's spin texture in 2D $1T'$-MoSi$_2$P$_4$. Red (blue) indicates up (down) spin polarization. (d) and (e) Schematic representations of the various nontrivial edge states (red lines) connecting the bulk valence and conduction bands (light blue shading) between the two time-reversal-invariant points $\overline{\Gamma}$ and $\overline{X}$.

edges are related by inversion symmetry, we display states for the left edge in Figs. 3(b) and 3(c). A pair of counterpropagating states with opposite spin polarization are seen in the band gap with a Dirac point at $\overline{\Gamma}$. The nontrivial edge states span the whole $\overline{\Gamma}$-$\overline{X}$ line to connect the bulk valence and conduction bands, as shown schematically in Fig. 3(e). Similar results are found for other $1T'$-MSi$_2$Z$_4$ materials.

Having established the QSH state in $1T'$-MSi$_2$Z$_4$ monolayers, we turn to discuss their intrinsic SHCs. We obtain the SHC σ_{xy}^z using the Kubo formula [55–59]:

$$\sigma_{xy}^z = \frac{-e^2}{\hbar} \frac{1}{A} \sum_k \Omega_{xy}^z(\boldsymbol{k}), \tag{1}$$

where

$$\Omega_{xy}^z(\boldsymbol{k}) = \sum_n f_n(\boldsymbol{k}) \Omega_{n,xy}^z(\boldsymbol{k}) \tag{2}$$

is the k-resolved spin Berry curvature and

$$\Omega_{n,xy}^z(\boldsymbol{k}) = \hbar^2 \sum_{m \neq n} \frac{-2\text{Im}\langle n\boldsymbol{k}|\hat{J}_x^z|m\boldsymbol{k}\rangle \langle m\boldsymbol{k}|\hat{v}_y|n\boldsymbol{k}\rangle}{(E_{n\boldsymbol{k}} - E_{m\boldsymbol{k}})^2} \tag{3}$$

is the band-resolved spin Berry curvature.

In Eqs. (1)–(3), A is the area of the 2D unit cell, and $|n\boldsymbol{k}\rangle$ denotes the Bloch state with energy $E_{n\boldsymbol{k}}$ and occupation $f_n(\boldsymbol{k})$. The spin current operator $\hat{J}_x^z = \frac{1}{2}\{\hat{\sigma}_z, \hat{v}_x\}$, with $\hat{\sigma}_z$ being the spin operator and $\hat{v}_x$ being the velocity operator. The SHC $\sigma_{x,y}^z$ represents the spin current along the x direction generated by the electric field along the y direction, where the spin current is polarized along the z direction. We used a dense grid of 10^6 k points in conjunction with maximally localized Wannier functions to evaluate the spin Berry curvature and SHC. Figure 4(a) presents the calculated SHC as a function of the Fermi energy. The SHC is maximum near the band-crossing points (marked by the dashed line), reaching a value of $\sim 1.3 \frac{e^2}{h}$, which is much larger than the $1T'$ TMDs with the QSH state. The amplitude of the SHC decreases quickly away from the band-crossing points. This can be further seen from our band- and k-resolved spin Berry curvature in Fig. 4(b). The spin Berry curvature is largely concentrated near the valence and conduction band-crossing points along the Γ-Y direction, which have a SOC-driven hybridization gap. Notably, the perfect quantization of the SHC requires an S_z-conserved Hamiltonian. However, realistic material parameters depend on the constraints of point-group symmetries, coupling of
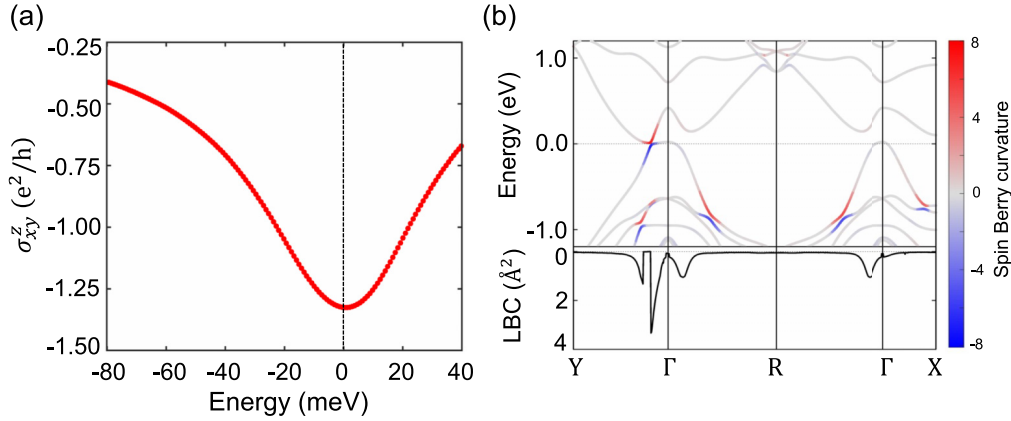
FIG. 4. (a) Intrinsic spin Hall conductivity (SHC) σ_{xy}^z as a function of Fermi energy in monolayer $1T'$-MoSi$_2$P$_4$. SHC is given in units of $\frac{e^2}{h}$. The value of the SHC is maximum at the Fermi level. (b) Band-resolved (top) and k-resolved (bottom) spin Berry curvature of monolayer MoSi$_2$P$_4$ along the high-symmetry directions in the 2D Brillouin zone. LBC stands for the logarithm of $\Omega_{xy}^z(\boldsymbol{k})$ [Eq. (2)], and the color bar refers to the logarithm of $\Omega_{n,xy}^z(\boldsymbol{k})$ [Eq. (3)].

various bands, and the local atomic geometries, among other factors, which lead to nonconserved-S_z Hamiltonians [60]. As the local atomic geometry and spin-orbit interactions in MSi$_2$Z$_4$ are different from the $1T'$ TMDs, differences in their SHC values are naturally expected [61]. An optimal setup to exploit the large SHC in MoSi$_2$P$_4$ would be in the clean limit with the Fermi level lying between the band-crossing points.

D. Electric field switching of the quantum spin Hall state

We now demonstrate the tunability of the QSH state and the switching of the topological state under a vertical electric field. Topologically inverted bands between the transition metal d and pnictogen's p orbitals lie in well-separated 2D planes in the $1T'$ monolayer. This distinct spatial location of bands provides a natural basis for their tunability via an out-of-plane (vertical) electric field E_z. Figure 5 shows the HSE band structure for various electric field values. The electric field induces Rashba spin splittings in the states by breaking the inversion equivalence on the top and bottom sides of the monolayers. This is evident from spin-split states shown with distinct colors in the top panels of Figs. 5(b) and 5(c). As the electric field increases, the band gap decreases to zero at the critical electric field value of $E_c = 0.187$ eV/Å, where the spin-up and spin-down bands cross at opposite Λ points. With a further increase in the electric field, the band gap reopens. An analysis based on the Z_2 invariants and edge-state dispersions (Fig. 5) shows that this band gap closing drives a change in the topology to a trivial state with $Z_2 = 0$. This topological phase transition destroys the topological edge states, thereby switching off the QSH state in $1T'$-MoSi$_2$P$_4$. A change in the polarity of the electric field shows a similar topological phase transition to a trivial state. The evolution of the QSH and trivial insulator states as a function of the applied electric field is displayed in Fig. 6.

The preceding results indicate an electric field on-off control of the spin-polarized edge currents in $1T'$-MSi$_2$Z$_4$ similar to the case of $1T'$ TMDs [14]. Since the crystal symmetries of both these material families are the same, various device ideas conceived for $1T'$ TMDs can be applied to the MSi$_2$Z$_4$ family with the added advantage of a large, inverted band gap and large SHC. For example, monolayer MSi$_2$Z$_4$ could be interfaced with a large band gap 2D insulator to protect the helical edge channels from being gapped by interlayer hybridization to realize a topological transistor [14]. When the Fermi level is placed in the nontrivial band gap, a nearly quantized SHC would be realized in this device under zero or small electric fields. An electric field beyond the critical value of ±0.187 eV/Å can switch off the quantized spin Hall conductance, driving it into a trivial insulating state.
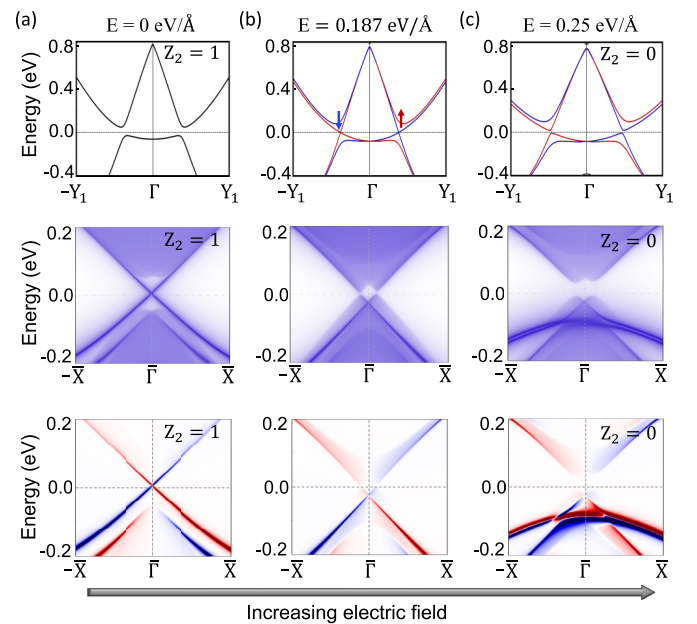

FIG. 5. Band structure of the $1T'$-MoSi$_2$P$_4$ monolayer for various values of the vertical electric field E_z: (a) 0, (b) 0.187, and (c) 0.250 eV/Å. The top, middle, and bottom rows show the 2D band structure, the (010) edge spectrum, and the edge-state spin texture, respectively. Red (blue) identifies the up (down) spin state.
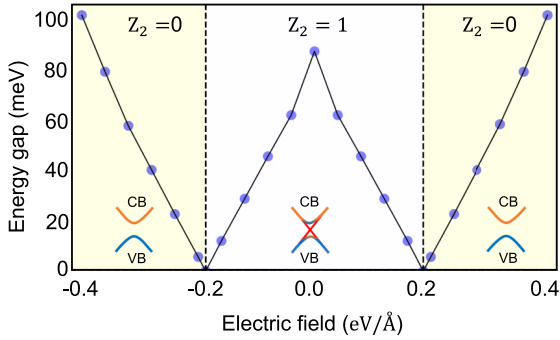
FIG. 6. Topological phase diagram of $1T'$-MoSi$_2$P$_4$ as a function of the vertical electric field E_z. Critical electric field strengths for the topological phase transition from the $Z_2 = 1$ to $Z_2 = 0$ state are marked by vertical dashed lines.

IV. SUMMARY

We have demonstrated the existence of a tunable QSH state with a large band gap in a polytypic structure of the recently introduced bottom-up synthesized MSi$_2$Z$_4$ family of 2D materials. Our analysis based on phonon spectra and molecular dynamics simulations showed that these materials realize a thermodynamically stable $1T'$ phase in addition to the putative $1H$ phase. Our in-depth electronic structure modeling revealed that a structural distortion in the $1H$ phase leads to the $1T'$ structure and induces a topological band inversion. A hybridization gap as large as 204 meV was found for the MSi$_2$Z$_4$ family that is even larger than the one in the existing $1T'$ TMDs that host a QSH ground state. Our calculated SHC shows a large value of $\sim 1.3 \frac{e^2}{h}$ in MoSi$_2$P$_4$ that arises from the large spin Berry curvature induced by spin-orbit-split bands at the band inversion points. We also showed that the QSH state is tunable with a vertical electric field, which provides an external control for switching or turning on and off the QSH state. Our study thus not only introduces a polytypic structure of the recently introduced 2D MSi$_2$Z$_4$ materials, which support a large band gap QSH state, but also suggests that this material family will potentially provide a promising platform for realizing nontrivial states with large spin Hall conductance.

[1] K. S. Novoselov, Nobel lecture: Graphene: Materials in the flatland, Rev. Mod. Phys. **83**, 837 (2011).

[2] A. H. Castro Neto, F. Guinea, N. M. R. Peres, K. S. Novoselov, and A. K. Geim, The electronic properties of graphene, Rev. Mod. Phys. **81**, 109 (2009).

[3] K. S. Novoselov, D. Jiang, F. Schedin, T. J. Booth, V. V. Khotkevich, S. V. Morozov, and A. K. Geim, Two-dimensional atomic crystals, Proc. Natl. Acad. Sci. USA **102**, 10451 (2005).

[4] S. Manzeli, D. Ovchinnikov, D. Pasquier, O. V. Yazyev, and A. Kis, 2D transition metal dichalcogenides, Nat. Rev. Mater. **2**, 17033 (2017).

[5] C. L. Kane and E. J. Mele, Quantum Spin Hall Effect in Graphene, Phys. Rev. Lett. **95**, 226801 (2005).

[6] C. L. Kane and E. J. Mele, Z_2 Topological Order and the Quantum Spin Hall Effect, Phys. Rev. Lett. **95**, 146802 (2005).

[7] A. Bansil, H. Lin, and T. Das, Colloquium: Topological band theory, Rev. Mod. Phys. **88**, 021004 (2016).

[8] M. Z. Hasan and C. L. Kane, Colloquium: Topological insulators, Rev. Mod. Phys. **82**, 3045 (2010).

[9] B. Singh, H. Lin, and A. Bansil, Topology and symmetry in quantum materials, Adv. Mater., 2201058 (2022).

[10] B. A. Bernevig and S.-C. Zhang, Quantum Spin Hall Effect, Phys. Rev. Lett. **96**, 106802 (2006).

[11] B. A. Bernevig, T. L. Hughes, and S.-C. Zhang, Quantum spin Hall effect and topological phase transition in HgTe quantum wells, Science **314**, 1757 (2006).

[12] B. Singh, H. Lin, R. Prasad, and A. Bansil, Topological phase transition and two-dimensional topological insulators in Ge-based thin films, Phys. Rev. B **88**, 195147 (2013).

[13] A. Marrazzo, M. Gibertini, D. Campi, N. Mounet, and N. Marzari, Prediction of a Large-Gap and Switchable Kane-Mele Quantum Spin Hall Insulator, Phys. Rev. Lett. **120**, 117701 (2018).

[14] X. Qian, J. Liu, L. Fu, and J. Li, Quantum spin Hall effect in two-dimensional transition metal dichalcogenides, Science **346**, 1344 (2014).

[15] Y. Xu, B. Yan, H.-J. Zhang, J. Wang, G. Xu, P. Tang, W. Duan, and S.-C. Zhang, Large-Gap Quantum Spin Hall Insulators in Tin Films, Phys. Rev. Lett. **111**, 136804 (2013).

[16] C. Liu, T. L. Hughes, X.-L. Qi, K. Wang, and S.-C. Zhang, Quantum Spin Hall Effect in Inverted Type-II Semiconductors, Phys. Rev. Lett. **100**, 236601 (2008).

[17] M. König, S. Wiedmann, C. Brüne, A. Roth, H. Buhmann, L. W. Molenkamp, X.-L. Qi, and S.-C. Zhang, Quantum spin Hall insulator state in HgTe quantum wells, Science **318**, 766 (2007).

[18] I. Knez, R.-R. Du, and G. Sullivan, Evidence for Helical Edge Modes in Inverted InAs/GaSb Quantum Wells, Phys. Rev. Lett. **107**, 136603 (2011).

[19] S. Tang, C. Zhang, D. Wong, Z. Pedramrazi, H.-Z. Tsai, C. Jia, B. Moritz, M. Claassen, H. Ryu, S. Kahn *et al.*, Quantum spin Hall state in monolayer $1T'$-WTe$_2$, Nat. Phys. **13**, 683 (2017).

[20] K. Kandrai, P. Vancsó, G. Kukucska, J. Koltai, G. Baranka, Á. Hoffmann, Á. Pekker, K. Kamarás, Z. E. Horváth, A. Vymazalová, L. Tapasztó, and P. Nemes-Incze, Signature of large-gap quantum spin Hall state in the layered mineral jacutingaite, Nano Lett. **20**, 5207 (2020).

[21] N. Shumiya *et al.*, Evidence of a room-temperature quantum spin Hall edge state in a higher-order topological insulator, Nat. Mater. **21**, 1111 (2022).

[22] Z. Fei, T. Palomaki, S. Wu, W. Zhao, X. Cai, B. Sun, P. Nguyen, J. Finney, X. Xu, and D. H. Cobden, Edge conduction in monolayer WTe$_2$, Nat. Phys. **13**, 677 (2017).

[23] S. Wu, V. Fatemi, Q. D. Gibson, K. Watanabe, T. Taniguchi, R. J. Cava, and P. Jarillo-Herrero, Observation of the quantum spin Hall effect up to 100 kelvin in a monolayer crystal, Science **359**, 76 (2018).

[24] H. Lin, R. S. Markiewicz, L. A. Wray, L. Fu, M. Z. Hasan, and A. Bansil, Single-Dirac-Cone Topological Surface States in the TLBiSe$_2$ Class of Topological Semiconductors, Phys. Rev. Lett. **105**, 036404 (2010).

[25] Y.-F. Zhang, J. Pan, H. Banjade, J. Yu, H. Lin, A. Bansil, S. Du, and Q. Yan, Two-dimensional MX Dirac materials and quantum spin Hall insulators with tunable electronic and topological properties, Nano Res. **14**, 584 (2021).

[26] Z.-Y. Jia, Y.-H. Song, X.-B. Li, K. Ran, P. Lu, H.-J. Zheng, X.-Y. Zhu, Z.-Q. Shi, J. Sun, J. Wen, D. Xing, and S.-C. Li, Direct visualization of a two-dimensional topological insulator in the single-layer $1T'$-WTe$_2$, Phys. Rev. B **96**, 041108(R) (2017).

[27] Z. Li, Y. Song, and S. Tang, Quantum spin Hall state in monolayer 1T'-TMDCs, J. Phys.: Condens. Matter **32**, 333001 (2020).

[28] Y. Cao *et al.*, Quality heterostructures from two-dimensional crystals unstable in air by their assembly in inert atmosphere, Nano Lett. **15**, 4914 (2015).

[29] Y. Zhang, K. He, C.-Z. Chang, C.-L. Song, L.-L. Wang, X. Chen, J.-F. Jia, Z. Fang, X. Dai, W.-Y. Shan, S.-Q. Shen, Q. Niu, X.-L. Qi, S.-C. Zhang, X.-C. Ma, and Q.-K. Xue, Crossover of the three-dimensional topological insulator Bi$_2$Se$_3$ to the two-dimensional limit, Nat. Phys. **6**, 584 (2010).

[30] F. Ye, J. Lee, J. Hu, Z. Mao, J. Wei, and P. X.-L. Feng, Environmental instability and degradation of single- and few-layer WTe$_2$ nanosheets in ambient conditions, Small **12**, 5802 (2016).

[31] J.-J. Zhang, D. Zhu, and B. I. Yakobson, Heterobilayer with ferroelectric switching of topological state, Nano Lett. **21**, 785 (2021).

[32] K. S. Novoselov, A. Mishchenko, A. Carvalho, and A. H. C. Neto, 2D materials and van der Waals heterostructures, Science **353**, aac9439 (2016).

[33] K. S. Novoselov, Discovery of 2D van der Waals layered MoSi$_2$N$_4$ family, Natl. Sci. Rev. **7**, 1842 (2020).

[34] Y.-L. Hong, Z. Liu, L. Wang, T. Zhou, W. Ma, C. Xu, S. Feng, L. Chen, M.-L. Chen, D.-M. Sun *et al.*, Chemical vapor deposition of layered two-dimensional MoSi$_2$N$_4$ materials, Science **369**, 670 (2020).

[35] R. Islam, B. Ghosh, C. Autieri, S. Chowdhury, A. Bansil, A. Agarwal, and B. Singh, Tunable spin polarization and electronic structure of bottom-up synthesized MoSi$_2$N$_4$ materials, Phys. Rev. B **104**, L201112 (2021).

[36] C. Yang, Z. Song, X. Sun, and J. Lu, Valley pseudospin in monolayer MoSi$_2$N$_4$ and MoSi$_2$As$_4$, Phys. Rev. B **103**, 035308 (2021).

[37] S. Li, W. Wu, X. Feng, S. Guan, W. Feng, Y. Yao, and S. A. Yang, Valley-dependent properties of monolayer MoSi$_2$N$_4$, WSi$_2$N$_4$, and MoSi$_2$As$_4$, Phys. Rev. B **102**, 235435 (2020).

[38] X. Feng, X. Xu, Z. He, R. Peng, Y. Dai, B. Huang, and Y. Ma, Valley-related multiple Hall effect in monolayer VSi$_2$P$_4$, Phys. Rev. B **104**, 075421 (2021).

[39] S. Bertolazzi, J. Brivio, and A. Kis, Stretching and breaking of ultrathin MoS$_2$, ACS Nano **5**, 9703 (2011).

[40] Y. Cai, G. Zhang, and Y.-W. Zhang, Polarity-reversed robust carrier mobility in monolayer MoS$_2$ nanoribbons, J. Am. Chem. Soc. **136**, 6269 (2014).

[41] P. Hohenberg and W. Kohn, Inhomogeneous electron gas, Phys. Rev. **136**, B864 (1964).

[42] G. Kresse and J. Furthmüller, Efficient iterative schemes for *ab initio* total-energy calculations using a plane-wave basis set, Phys. Rev. B **54**, 11169 (1996).

[43] J. P. Perdew, K. Burke, and M. Ernzerhof, Generalized Gradient Approximation Made Simple, Phys. Rev. Lett. **77**, 3865 (1996).

[44] J. Heyd, G. E. Scuseria, and M. Ernzerhof, Hybrid functionals based on a screened Coulomb potential, J. Chem. Phys. **118**, 8207 (2003).

[45] A. Togo and I. Tanaka, First principles phonon calculations in materials science, Scr. Mater. **108**, 1 (2015).

[46] R. N. Barnett and U. Landman, Born-Oppenheimer molecular-dynamics simulations of finite systems: Structure and dynamics of (H$_2$O)$_2$, Phys. Rev. B **48**, 2081 (1993).

[47] A. A. Mostofi, J. R. Yates, Y.-S. Lee, I. Souza, D. Vanderbilt, and N. Marzari, WANNIER90: A tool for obtaining maximally-localised Wannier functions, Comput. Phys. Commun. **178**, 685 (2008).

[48] Q. Wu, S. Zhang, H.-F. Song, M. Troyer, and A. A. Soluyanov, WannierTools: An open-source software package for novel topological materials, Comput. Phys. Commun. **224**, 405 (2018).

[49] M. P. L. Sancho, J. M. L. Sancho, J. M. L. Sancho, and J. Rubio, Highly convergent schemes for the calculation of bulk and surface Green functions, J. Phys. F **15**, 851 (1985).

[50] See Supplemental Material at http://link.aps.org/supplemental/10.1103/PhysRevB.106.245149 for the stability of $1T'$-MSi$_2$Z$_4$ and bulk and edge-state properties for all the studied materials (see also Refs. [62–66] therein).

[51] M. Calandra, Chemically exfoliated single-layer MoS$_2$: Stability, lattice dynamics, and catalytic adsorption from first principles, Phys. Rev. B **88**, 245428 (2013).

[52] L. Liu, J. Wu, L. Wu, M. Ye, X. Liu, Q. Wang, S. Hou, P. Lu, L. Sun, J. Zheng, L. Xing, L. Gu, X. Jiang, L. Xie, and L. Jiao, Phase-selective synthesis of $1T'$MoS$_2$ monolayers and heterophase bilayers, Nat. Mater. **17**, 1108 (2018).

[53] R. Islam, B. Ghosh, G. Cuono, A. Lau, W. Brzezicki, A. Bansil, A. Agarwal, B. Singh, T. Dietl, and C. Autieri, Topological states in superlattices of HgTe class of materials for engineering three-dimensional flat bands, Phys. Rev. Res. **4**, 023114 (2022).

[54] G. Hussain, A. Samad, M. Ur Rehman, G. Cuono, and C. Autieri, Emergence of Rashba splitting and spin-valley properties in Janus MoGeSiP$_2$As$_2$ and WGeSiP$_2$As$_2$ monolayers, J. Magn. Magn. Mater. **563**, 169897 (2022).

[55] L. Matthes, S. Küfner, J. Furthmüller, and F. Bechstedt, Intrinsic spin Hall conductivity in one-, two-, and three-dimensional trivial and topological systems, Phys. Rev. B **94**, 085410 (2016).

[56] Y. Sun, Y. Zhang, C. Felser, and B. Yan, Strong Intrinsic Spin Hall Effect in the TaAs Family of Weyl Semimetals, Phys. Rev. Lett. **117**, 146403 (2016).

[57] R. Zhang, C.-Y. Huang, J. Kidd, R. S. Markiewicz, H. Lin, A. Bansil, B. Singh, and J. Sun, Weyl semimetal in the rare-earth hexaboride family supporting a pseudonodal surface and a giant anomalous Hall effect, Phys. Rev. B **105**, 165140 (2022).

[58] J. Zhou, J. Qiao, A. Bournel, and W. Zhao, Intrinsic spin Hall conductivity of the semimetals MoTe$_2$ and WTe$_2$, Phys. Rev. B **99**, 060408(R) (2019).

[59] J. Qiao, J. Zhou, Z. Yuan, and W. Zhao, Calculation of intrinsic spin Hall conductivity by Wannier interpolation, Phys. Rev. B **98**, 214402 (2018).

[60] F. Matusalem, M. Marques, L. K. Teles, L. Matthes, J. Furthmüller, and F. Bechstedt, Quantization of spin Hall conductivity in two-dimensional topological insulators versus

[61] Understanding the mechanisms responsible for large SHCs in MSi$_2$Z$_4$ compared to TMDs would be interesting, but that requires an in-depth comparison of their geometric and electronic properties, which is outside the scope of this study.

[62] A. A. Soluyanov and D. Vanderbilt, Computing topological invariants without inversion symmetry, Phys. Rev. B **83**, 235401 (2011).

[63] A. Alexandradinata, X. Dai, and B. A. Bernevig, Wilson-loop characterization of inversion-symmetric topological insulators, Phys. Rev. B **89**, 155114 (2014).

[64] R. Yu, X. L. Qi, A. Bernevig, Z. Fang, and X. Dai, Equivalent expression of $\mathbb{z}_2$ topological invariant for band insulators using the non-Abelian Berry connection, Phys. Rev. B **84**, 075119 (2011).

[65] A. Bouhon and A. M. Black-Schaffer, Global band topology of simple and double Dirac-point semimetals, Phys. Rev. B **95**, 241101(R) (2017).

[66] C. Autieri, A. Bouhon, and B. Sanyal, Gap opening and large spin-orbit splitting in MX$_2$ (M = Mo, W; X = S, Se, Te) from the interplay between crystal field and hybridisations insights from *ab-initio* theory, Philos. Mag. **97**, 3381 (2017).

symmetry and spin-orbit interaction, Phys. Rev. B **100**, 245430 (2019).

OUTLOOK

Researchers have been captivated by quantum materials over the past ten years because of a variety of fascinating physical phenomena, including, quantized Hall conductivity in QH insulators, counter propagation of dissipationless current in QSH insulators, chiral edge current in QAH insulators, and Axion electrodynamics in Axion insulators. Semimetallic quantum materials exhibit interesting high energy phenomena in the area of condensed matter physics in addition to the insulating phase. The Dirac and Weyl quasiparticles exhibit special transport features in the materials, including the inherent anomalous Hall effect, chiral anomaly, and negative magnetoresistance. Because of its wide array of applications in quantum information and quantum electronics, the prediction of new material candidates and engineering materials that exhibit exotic physical phenomena has attracted research in the field of condensed matter physics.

The promising candidate for the realization and study of three-dimensional flat bands, which could give rise to exotic, strongly correlated phases as a result of an enhancement of electronic interactions, are the isoenergetic nodal-line phases in HgTe/CdTe superlattices and the uniaxially strained HgTe/HgSe superlattices. A possible method to create the necessary bend to obtain the flat bands is the synthesis of core-shell nanowires of the HgTe-based superlattices, which has been prompted by recent experimental progress in the growth of II-VI strained nanostructures by molecular beam epitaxy and high electron mobility systems [66, 113–115] .The II-IV semiconductor nanowires have been recently produced [116, 117]. Additionally, the flat band superconductivity in a band-inverted nanowire may provide a framework for hosting topological superconductivity and Majorana zero modes. Another potential area of study is the possibility of creating a topological insulator with multiple band inversions and hosting new exotic phases beyond the quantum spin Hall effect in 2D quantum wells of HgTe/HgSe with a thickness greater than the critical thickness and sandwiched between CdTe. The system has a

tendency to generate a digital alloy, therefore it will be difficult to fabricate a perfect interface between HgTe and HgSe in an experiment. Even in the case of a digital alloy, we anticipate the realization of a nearly ideal Weyl semimetal phase, which is topologically protected and arises at zero strain.

The axion insulators are promising material candidates to host the dark axion-like weakly interacting quasiparticles. It is a promising material candidate for the long-sought detection of dark matter. In the 3D SLs of the HgTe/MnTe could host Axion insulator phase evolve in the presence antiferromagnetic ordering. Recent experimental studies indicate that the axion insulator phase only evolves in three dimensions, it disappears in two dimensions by reducing the dimensionality(d)[118]. The topological states in Axion Insulator Phase are d-2 states in 3D, which are similar to Higher Order Topological Insulators (HOTI). The possibility of 2D HgTe/MnTe quantum wells preserving the Axion insulator phase or magnetic topological insulator with a (d-2) zero mode topological state is an interesting area for future research. Furthermore, by reducing the dimension to 2D, the HgTe/MnTe with ferromagnetism could leads to the Chern insulator phase with quantized anomalous Hall conductivity.

The successful experimental realization of the predicted bilayer-2H MSi_2Z_4 and 1T$'$-phase of MSi_2Z_4 is expected to be a tremendous success for applications in the real world. In addition to the experimental realization of the QSH effect in the 1T$'$ MSi_2Z_4 materials class, the magnetism in this 2D QSHI material could show an interesting magnetoelectric response. It is possible to observe a large-gap quantum anomalous Hall (QAH) insulating phase by constructing a heterostructure with a 2D vdW magnetic insulator. In contrast to the lattice mismatch, we anticipate that a heterostructure of $\sqrt{3}\times1$) $CoBr_2$ and (1x1) $MoSi_2As_4$ will be suitable as the QAH Insulator. Another direction will be the sandwich of $CoBr_2/MSi_2Z_4/CoBr_2$, which will create the possibility of understanding the interplay between different magnetisms (such as ferromagnetic or antiferromagnetic) and different interfacial phenomena. This will be an exciting new direction. These materials could be used to study a wide range of interesting physical phenomena and applications, from spintronics and quantum communication to dark matter detection.

Finally, we believe the investigation of quantum materials to be fascinating, finding a new material candidate is essential for the development of devices that operate at room temperature.

[1] Lev Davidovich Landau. On the theory of phase transitions. i. *Zh. Eksp. Teor. Fiz.*, 11:19, 1937.

[2] Lev Davidovich Landau. On the theory of phase transitions. ii. *Zh. Eksp. Teor. Fiz.*, 11:627, 1937.

[3] Aron J. Beekman, Louk Rademaker, and Jasper van Wezel. An introduction to spontaneous symmetry breaking. *SciPost Phys. Lect. Notes*, page 11, 2019.

[4] Marvin E Cage, Kv Klitzing, AM Chang, F Duncan, M Haldane, Robert B Laughlin, AMM Pruisken, and DJ Thouless. *The quantum Hall effect*. Springer Science & Business Media, 2012.

[5] K v Klitzing, Gerhard Dorda, and Michael Pepper. New method for high-accuracy determination of the fine-structure constant based on quantized hall resistance. *Physical review letters*, 45(6):494, 1980.

[6] David J Thouless, Mahito Kohmoto, M Peter Nightingale, and Marcel den Nijs. Quantized hall conductance in a two-dimensional periodic potential. *Physical review letters*, 49(6):405, 1982.

[7] F Duncan M Haldane. Model for a quantum hall effect without landau levels: Condensed-matter realization of the" parity anomaly". *Physical review letters*, 61(18):2015, 1988.

[8] Charles L Kane and Eugene J Mele. Quantum spin hall effect in graphene. *Physical review letters*, 95(22):226801, 2005.

[9] Charles L Kane and Eugene J Mele. Z 2 topological order and the quantum spin hall effect. *Physical review letters*, 95(14):146802, 2005.

[10] Markus Konig, Steffen Wiedmann, Christoph Brune, Andreas Roth, Hartmut Buhmann, Laurens W Molenkamp, Xiao-Liang Qi, and Shou-Cheng Zhang. Quantum spin hall insulator state in hgte quantum wells. *Science*, 318(5851):766–770, 2007.

[11]   B Andrei Bernevig, Taylor L Hughes, and Shou-Cheng Zhang. Quantum spin hall effect and topological phase transition in hgte quantum wells. *science*, 314(5806):1757–1761, 2006.

[12]   Liang Fu, Charles L Kane, and Eugene J Mele. Topological insulators in three dimensions. *Physical review letters*, 98(10):106803, 2007.

[13]   David Hsieh, Dong Qian, Lewis Wray, Yiman Xia, Yew San Hor, Robert Joseph Cava, and M Zahid Hasan. A topological dirac insulator in a quantum spin hall phase. *Nature*, 452(7190):970–974, 2008.

[14]   David Hsieh, Yuqi Xia, L Wray, Dong Qian, Arijeet Pal, JH Dil, J Osterwalder, F Meier, G Bihlmayer, CL Kane, et al. Observation of unconventional quantum spin textures in topological insulators. *Science*, 323(5916):919–922, 2009.

[15]   Timothy H Hsieh, Hsin Lin, Junwei Liu, Wenhui Duan, Arun Bansil, and Liang Fu. Topological crystalline insulators in the snte material class. *Nature communications*, 3(1):1–7, 2012.

[16]   NP Armitage, EJ Mele, and Ashvin Vishwanath. Weyl and dirac semimetals in three-dimensional solids. *Reviews of Modern Physics*, 90(1):015001, 2018.

[17]   Chen Fang, Hongming Weng, Xi Dai, and Zhong Fang. Topological nodal line semimetals. *Chinese Physics B*, 25(11):117106, 2016.

[18]   Cui-Zu Chang, Jinsong Zhang, Xiao Feng, Jie Shen, Zuocheng Zhang, Minghua Guo, Kang Li, Yunbo Ou, Pang Wei, Li-Li Wang, et al. Experimental observation of the quantum anomalous hall effect in a magnetic topological insulator. *Science*, 340(6129):167–170, 2013.

[19]   Yujun Deng, Yijun Yu, Meng Zhu Shi, Zhongxun Guo, Zihan Xu, Jing Wang, Xian Hui Chen, and Yuanbo Zhang. Quantum anomalous hall effect in intrinsic magnetic topological insulator mnbi2te4. *Science*, 367(6480):895–900, 2020.

[20]   Jiaheng Li, Yang Li, Shiqiao Du, Zun Wang, Bing-Lin Gu, Shou-Cheng Zhang, Ke He, Wenhui Duan, and Yong Xu. Intrinsic magnetic topological insulators in van der waals layered mnbi2te4-family materials. *Science Advances*, 5(6):eaaw5685, 2019.

[21]   Ilya Belopolski, Kaustuv Manna, Daniel S Sanchez, Guoqing Chang, Benedikt Ernst, Jiaxin Yin, Songtian S Zhang, Tyler Cochran, Nana Shumiya, Hao Zheng, et al. Discovery of topological weyl fermion lines and drumhead surface states in a room temperature magnet. *Science*, 365(6459):1278–1281, 2019.

[22] M Mogi, M Kawamura, R Yoshimi, A Tsukazaki, Y Kozuka, N Shirakawa, KS Takahashi, M Kawasaki, and Y Tokura. A magnetic heterostructure of topological insulators as a candidate for an axion insulator. *Nature materials*, 16(5):516–521, 2017.

[23] Chang Liu, Yongchao Wang, Hao Li, Yang Wu, Yaoxin Li, Jiaheng Li, Ke He, Yong Xu, Jinsong Zhang, and Yayu Wang. Robust axion insulator and chern insulator phases in a two-dimensional antiferromagnetic topological insulator. *Nature materials*, 19(5):522–527, 2020.

[24] Arun Bansil, Hsin Lin, and Tanmoy Das. Colloquium: Topological band theory. *Reviews of Modern Physics*, 88(2):021004, 2016.

[25] M Zahid Hasan and Charles L Kane. Colloquium: topological insulators. *Reviews of modern physics*, 82(4):3045, 2010.

[26] Xiao-Liang Qi and Shou-Cheng Zhang. Topological insulators and superconductors. *Reviews of Modern Physics*, 83(4):1057, 2011.

[27] Liang Fu. Topological crystalline insulators. *Physical Review Letters*, 106(10):106802, 2011.

[28] Alexey A Soluyanov and David Vanderbilt. Wannier representation of z 2 topological insulators. *Physical Review B*, 83(3):035108, 2011.

[29] Junwei Liu, Wenhui Duan, and Liang Fu. Two types of surface states in topological crystalline insulators. *Physical Review B*, 88(24):241303, 2013.

[30] Eslam Khalaf, Hoi Chun Po, Ashvin Vishwanath, and Haruki Watanabe. Symmetry indicators and anomalous surface states of topological crystalline insulators. *Physical Review X*, 8(3):031070, 2018.

[31] Chuang-Han Hsu, Xiaoting Zhou, Qiong Ma, Nuh Gedik, Arun Bansil, Vitor M Pereira, Hsin Lin, Liang Fu, Su-Yang Xu, and Tay-Rong Chang. Purely rotational symmetry-protected topological crystalline insulator-bi4br4. *2D Materials*, 6(3):031004, 2019.

[32] Haijun Zhang, Chao-Xing Liu, Xiao-Liang Qi, Xi Dai, Zhong Fang, and Shou-Cheng Zhang. Topological insulators in bi2se3, bi2te3 and sb2te3 with a single dirac cone on the surface. *Nature physics*, 5(6):438–442, 2009.

[33] Chao-Xing Liu, Xiao-Liang Qi, HaiJun Zhang, Xi Dai, Zhong Fang, and Shou-Cheng Zhang. Model hamiltonian for topological insulators. *Physical Review B*, 82(4):045122, 2010.

[34] Binghai Yan and Claudia Felser. Topological materials: Weyl semimetals. *Annual Review of Condensed Matter Physics*, 8:337–354, 2017.

[35] Bohm-Jung Yang and Naoto Nagaosa. Classification of stable three-dimensional dirac semimetals with nontrivial topology. *Nature communications*, 5(1):1–10, 2014.

[36] Zhijun Wang, Yan Sun, Xing-Qiu Chen, Cesare Franchini, Gang Xu, Hongming Weng, Xi Dai, and Zhong Fang. Dirac semimetal and topological phase transitions in a 3 bi (a= na, k, rb). *Physical Review B*, 85(19):195320, 2012.

[37] Zhijun Wang, Hongming Weng, Quansheng Wu, Xi Dai, and Zhong Fang. Three-dimensional dirac semimetal and quantum transport in cd 3 as 2. *Physical Review B*, 88(12):125427, 2013.

[38] ZK Liu, Bo Zhou, Yong Zhang, ZJ Wang, HM Weng, Dharmalingam Prabhakaran, S-K Mo, ZX Shen, Zhong Fang, Xi Dai, et al. Discovery of a three-dimensional topological dirac semimetal, na3bi. *Science*, 343(6173):864–867, 2014.

[39] Madhab Neupane, Su-Yang Xu, Raman Sankar, Nasser Alidoust, Guang Bian, Chang Liu, Ilya Belopolski, Tay-Rong Chang, Horng-Tay Jeng, Hsin Lin, et al. Observation of a three-dimensional topological dirac semimetal phase in high-mobility cd3as2. *Nature communications*, 5(1):1–8, 2014.

[40] ZK Liu, Jianzhong Jiang, Bo Zhou, ZJ Wang, Yi Zhang, HM Weng, Dharmalingam Prabhakaran, Sung Kwan Mo, Han Peng, Pavel Dudin, et al. A stable three-dimensional topological dirac semimetal cd3as2. *Nature materials*, 13(7):677–681, 2014.

[41] Steve M Young, Saad Zaheer, Jeffrey CY Teo, Charles L Kane, Eugene J Mele, and Andrew M Rappe. Dirac semimetal in three dimensions. *Physical review letters*, 108(14):140405, 2012.

[42] Steve M Young and Charles L Kane. Dirac semimetals in two dimensions. *Physical review letters*, 115(12):126803, 2015.

[43] Holger Bech Nielsen and Masao Ninomiya. The adler-bell-jackiw anomaly and weyl fermions in a crystal. *Physics Letters B*, 130(6):389–396, 1983.

[44] Su-Yang Xu, Ilya Belopolski, Nasser Alidoust, Madhab Neupane, Guang Bian, Chenglong Zhang, Raman Sankar, Guoqing Chang, Zhujun Yuan, Chi-Cheng Lee, et al. Discovery of a weyl fermion semimetal and topological fermi arcs. *Science*, 349(6248):613–617, 2015.

[45] BQ Lv, HM Weng, BB Fu, X Ps Wang, Hu Miao, Junzhang Ma, P Richard, XC Huang, LX Zhao, GF Chen, et al. Experimental discovery of weyl semimetal taas. *Physical Review X*, 5(3):031013, 2015.

[46] Yan Sun, Shu-Chun Wu, Mazhar N Ali, Claudia Felser, and Binghai Yan. Prediction of weyl semimetal in orthorhombic mote$_2$. *Physical Review B*, 92(16):161107, 2015.

[47] Chenlu Wang, Yan Zhang, Jianwei Huang, Simin Nie, Guodong Liu, Aiji Liang, Yuxiao Zhang, Bing Shen, Jing Liu, Cheng Hu, et al. Observation of fermi arc and its connection with bulk states in the candidate type-ii weyl semimetal wte 2. *Physical Review B*, 94(24):241119, 2016.

[48] Su-Yang Xu, Nasser Alidoust, Guoqing Chang, Hong Lu, Bahadur Singh, Ilya Belopolski, Daniel S Sanchez, Xiao Zhang, Guang Bian, Hao Zheng, et al. Discovery of lorentz-violating type ii weyl fermions in laalge. *Science advances*, 3(6):e1603266, 2017.

[49] Shuo Wang, Ben-Chuan Lin, An-Qi Wang, Da-Peng Yu, and Zhi-Min Liao. Quantum transport in dirac and weyl semimetals: a review. *Advances in Physics: X*, 2(3):518–544, 2017.

[50] AA Burkov, MD Hook, and Leon Balents. Topological nodal semimetals. *Physical Review B*, 84(23):235126, 2011.

[51] BQ Lv, Z-L Feng, Q-N Xu, X Gao, J-Z Ma, L-Y Kong, P Richard, Y-B Huang, VN Strocov, C Fang, et al. Observation of three-component fermions in the topological semimetal molybdenum phosphide. *Nature*, 546(7660):627–631, 2017.

[52] Leslie M Schoop, Mazhar N Ali, Carola Straßer, Andreas Topp, Andrei Varykhalov, Dmitry Marchenko, Viola Duppel, Stuart SP Parkin, Bettina V Lotsch, and Christian R Ast. Dirac cone protected by non-symmorphic symmetry and three-dimensional dirac line node in zrsis. *Nature communications*, 7(1):1–7, 2016.

[53] Jin Hu, Zhijie Tang, Jinyu Liu, Xue Liu, Yanglin Zhu, David Graf, Kevin Myhro, Son Tran, Chun Ning Lau, Jiang Wei, et al. Evidence of topological nodal-line fermions in zrsise and zrsite. *Physical review letters*, 117(1):016602, 2016.

[54] C-J Yi, BQ Lv, QS Wu, B-B Fu, X Gao, M Yang, X-L Peng, M Li, Y-B Huang, P Richard, et al. Observation of a nodal chain with dirac surface states in ti b 2. *Physical Review B*, 97(20):201107, 2018.

[55] Xiaoming Zhang, Zhi-Ming Yu, Xian-Lei Sheng, Hui Ying Yang, and Shengyuan A Yang. Coexistence of four-band nodal rings and triply degenerate nodal points in centrosymmetric metal diborides. *Physical Review B*, 95(23):235116, 2017.

[56] Tay-Rong Chang, Ivo Pletikosic, Tai Kong, Guang Bian, Angus Huang, Jonathan Denlinger, Satya K Kushwaha, Boris Sinkovic, Horny-Tay Jeng, Tonica Valla, et al. Realization of a type-ii nodal-line semimetal in mg3bi2. *Advanced Science*, 6(4):1800897, 2019.

[57] Kangkang Li, Chenyuan Li, Jiangping Hu, Yuan Li, and Chen Fang. Dirac and nodal line magnons in three-dimensional antiferromagnets. *Physical review letters*, 119(24):247202, 2017.

[58] Zhida Song, Tiantian Zhang, and Chen Fang. Diagnosis for nonmagnetic topological semimetals in the absence of spin-orbital coupling. *Physical Review X*, 8(3):031069, 2018.

[59] Junyeong Ahn, Dongwook Kim, Youngkuk Kim, and Bohm-Jung Yang. Band topology and linking structure of nodal line semimetals with z 2 monopole charges. *Physical review letters*, 121(10):106403, 2018.

[60] Takafumi Nomura, Tetsuro Habe, Ryota Sakamoto, and Mikito Koshino. Three-dimensional graphdiyne as a topological nodal-line semimetal. *Physical Review Materials*, 2(5):054204, 2018.

[61] Ai Yamakage, Youichi Yamakawa, Yukio Tanaka, and Yoshihiko Okamoto. Line-node dirac semimetal and topological insulating phase in noncentrosymmetric pnictides caag x (x= p, as). *Journal of the Physical Society of Japan*, 85(1):013708, 2016.

[62] Jayita Nayak, Nitesh Kumar, Shu-Chun Wu, Chandra Shekhar, Jrg Fink, Emile DL Rienks, Gerhard H Fecher, Yan Sun, and Claudia Felser. Electronic properties of topological insulator candidate caagas. *Journal of Physics: Condensed Matter*, 30(4):045501, 2018.

[63] C. Q. Xu, R. Sankar, W. Zhou, Bin Li, Z. D. Han, B. Qian, J. H. Dai, Hengbo Cui, A. F. Bangura, F. C. Chou, and Xiaofeng Xu. Topological phase transition under pressure in the topological nodal-line superconductor pbtase$_2$. *Phys. Rev. B*, 96:064528, Aug 2017.

[64] Yoshinori Tokura, Kenji Yasuda, and Atsushi Tsukazaki. Magnetic topological insulators. *Nature Reviews Physics*, 1(2):126–143, 2019.

[65] Chao-Xing Liu, Xiao-Liang Qi, Xi Dai, Zhong Fang, and Shou-Cheng Zhang. Quantum anomalous hall effect in hg 1- y mn y te quantum wells. *Physical review letters*, 101(14):146802, 2008.

[66] Saquib Shamim, Wouter Beugeling, Jan Böttcher, Pragya Shekhar, Andreas Budewitz, Philipp Leubner, Lukas Lunczer, Ewelina M Hankiewicz, Hartmut Buhmann, and Laurens W Molenkamp. Emergent quantum hall effects below 50 mt in a two-dimensional topological insulator. *Science Advances*, 6(26):eaba4625, 2020.

[67] Nicodemos Varnava and David Vanderbilt. Surfaces of axion insulators. *Physical Review B*, 98(24):245117, 2018.

[68] Yuanfeng Xu, Zhida Song, Zhijun Wang, Hongming Weng, and Xi Dai. Higher-order topology of the axion insulator euin 2 as 2. *Physical review letters*, 122(25):256402, 2019.

[69] Libor Šmejkal, Yuriy Mokrousov, Binghai Yan, and Allan H MacDonald. Topological antiferromagnetic spintronics. *Nature physics*, 14(3):242–251, 2018.

[70] T Jungwirth, J Sinova, Aurelien Manchon, X Marti, J Wunderlich, and C Felser. The multiple directions of antiferromagnetic spintronics. *Nature Physics*, 14(3):200–203, 2018.

[71] G. Kresse and J. Furthmüller. Efficient iterative schemes for ab initio total-energy calculations using a plane-wave basis set. *Phys. Rev. B*, 54:11169–11186, Oct 1996.

[72] A. A. Mostofi, J. R. Yates, Young-Su Lee, I. Souza, D. Vanderbilt, and N. Marzari. wannier90: A tool for obtaining maximally-localised wannier functions. *Computer Physics Communications*, 178(9):685–699, May 2008.

[73] Nicola Marzari, Arash A. Mostofi, Jonathan R. Yates, Ivo Souza, and David Vanderbilt. Maximally localized wannier functions: Theory and applications. *Rev. Mod. Phys.*, 84:1419–1475, Oct 2012.

[74] QuanSheng Wu, ShengNan Zhang, Hai-Feng Song, M. Troyer, and A. A. Soluyanov. Wanniertools: An open-source software package for novel topological materials. *Comp. Phys. Commun.*, 224:405–416, Mar 2018.

[75] M. Z. Hasan and C. L. Kane. Colloquium: Topological insulators. *Rev. Mod. Phys.*, 82:3045–3067, Nov 2010.

[76] A. Bansil, Hsin Lin, and Tanmoy Das. Colloquium: Topological band theory. *Rev. Mod. Phys.*, 88:021004, Jun 2016.

[77] David Vanderbilt. *Berry Phases in Electronic Structure Theory: Electric Polarization, Orbital Magnetization and Topological Insulators*. Cambridge University Press, 2018.

[78] M. Born and R. Oppenheimer. Zur quantentheorie der molekeln. *Annalen der Physik*, 389(20):457–484, 1927.

[79] D. R. Hartree. The wave mechanics of an atom with a non-coulomb central field. part i. theory and methods. *Mathematical Proceedings of the Cambridge Philosophical Society*, 24(1):89–110, 1928.

[80] P. Hohenberg and W. Kohn. Inhomogeneous electron gas. *Phys. Rev.*, 136:B864–B871, Nov 1964.

[81] W. Kohn and L. J. Sham. Self-consistent equations including exchange and correlation effects. *Phys. Rev.*, 140:A1133–A1138, Nov 1965.

[82] O. Gunnarsson and B. I. Lundqvist. Exchange and correlation in atoms, molecules, and solids by the spin-density-functional formalism. *Phys. Rev. B*, 13:4274–4298, May 1976.

[83] D. M. Ceperley and B. J. Alder. Ground state of the electron gas by a stochastic method. *Phys. Rev. Lett.*, 45:566–569, Aug 1980.

[84] John P. Perdew, Kieron Burke, and Matthias Ernzerhof. Generalized gradient approximation made simple. *Phys. Rev. Lett.*, 77:3865–3868, Oct 1996.

[85] John P. Perdew and Yue Wang. Accurate and simple analytic representation of the electron-gas correlation energy. *Phys. Rev. B*, 45:13244–13249, Jun 1992.

[86] John P. Perdew, Adrienn Ruzsinszky, Gábor I. Csonka, Oleg A. Vydrov, Gustavo E. Scuseria, Lucian A. Constantin, Xiaolan Zhou, and Kieron Burke. Restoring the density-gradient expansion for exchange in solids and surfaces. *Phys. Rev. Lett.*, 100:136406, Apr 2008.

[87] Electronic structure of materials rajendra prasad: Taylor francis/crc press, 2013, 447 pages, 89.95, isbn 978-1-4665-0468-4. *MRS Bulletin*, 39(8):748–748, 2014.

[88] Burak Himmetoglu, Andrea Floris, Stefano de Gironcoli, and Matteo Cococcioni. Hubbard-corrected dft energy functionals: The lda+u description of correlated systems. *International Journal of Quantum Chemistry*, 114(1):14–49, 2014.

[89] Jochen Heyd, Gustavo E. Scuseria, and Matthias Ernzerhof. Hybrid functionals based on a screened coulomb potential. *The Journal of Chemical Physics*, 118(18):8207–8215, 2003.

[90] F Aryasetiawan and O Gunnarsson. TheGWmethod. *Reports on Progress in Physics*, 61(3):237–312, mar 1998.

[91] Dr Matt Probert. Electronic structure: Basic theory and practical methods, by richard m. martin. *Contemporary Physics*, 52(1):77–77, 2011.

[92] Paolo Giannozzi, Stefano Baroni, Nicola Bonini, Matteo Calandra, Roberto Car, Carlo Cavazzoni, Davide Ceresoli, Guido L Chiarotti, Matteo Cococcioni, Ismaila Dabo, Andrea Dal Corso, Stefano de Gironcoli, Stefano Fabris, Guido Fratesi, Ralph Gebauer, Uwe Gerstmann, Christos Gougoussis, Anton Kokalj, Michele Lazzeri, Layla Martin-Samos, Nicola Marzari, Francesco Mauri, Riccardo Mazzarello, Stefano Paolini, Alfredo Pasquarello, Lorenzo Paulatto, Carlo Sbraccia, Sandro Scandolo, Gabriele Sclauzero, Ari P Seitsonen, Alexander Smogunov, Paolo Umari, and Renata M Wentzcovitch. QUANTUM ESPRESSO: a modular and open-source software project for quantum simulations of materials. *Journal of Physics: Condensed Matter*, 21(39):395502, sep 2009.

[93] Solid state physics. von n. w. ashcroft und n. d. mermin; holt, rinehart and winston, new york 1976, xxii, 826 seiten, $19,95. *Physik in unserer Zeit*, 9(1):33–33, 1978.

[94] Nicola Marzari and David Vanderbilt. Maximally localized generalized wannier functions for composite energy bands. *Phys. Rev. B*, 56:12847–12865, Nov 1997.

[95] Gregory H. Wannier. The structure of electronic excitation levels in insulating crystals. *Phys. Rev.*, 52:191–197, Aug 1937.

[96] Alexander Lau, Rajyavardhan Ray, Dániel Varjas, and Anton R. Akhmerov. Influence of lattice termination on the edge states of the quantum spin hall insulator monolayer $1T^{'}-$wte$_2$. *Phys. Rev. Materials*, 3:054206, May 2019.

[97] Xiaofeng Qian, Junwei Liu, Liang Fu, and Ju Li. Quantum spin hall effect in two-dimensional transition metal dichalcogenides. *Science*, 346(6215):1344–1347, 2014.

[98] M. König, S.N Wiedmann, C. Brüne, A. Roth, H. Buhmann, L. W. Molenkamp, Xiao-Liang Qi, and Shou-Cheng Zhang. Quantum spin Hall insulator state in HgTe quantum wells. *Science*, 318(5851):766–770, 2007.

[99] F. Kirtschig, J. van den Brink, and C. Ortix. Surface-state spin textures in strained bulk HgTe: Strain-induced topological phase transitions. *Phys. Rev. B*, 94:235437, Dec 2016.

[100] A. M. Kadykov, S. S. Krishtopenko, B. Jouault, W. Desrat, W. Knap, S. Ruffenach, C. Consejo, J. Torres, S. V. Morozov, N. N. Mikhailov, S. A. Dvoretskii, and F. Teppe. Temperature-induced topological phase transition in HgTe quantum wells. *Phys. Rev. Lett.*, 120:086401, Feb 2018.

[101] K. S. Novoselov, A. K. Geim, S. V. Morozov, D. Jiang, Y. Zhang, S. V. Dubonos, I. V. Grigorieva, and A. A. Firsov. Electric field effect in atomically thin carbon films. *Science*, 306(5696):666–669, 2004.

[102] Kostya S Novoselov, Andre K Geim, Sergei Vladimirovich Morozov, Da Jiang, Michail I Katsnelson, IVa Grigorieva, SVb Dubonos, Firsov, and AA. Two-dimensional gas of massless dirac fermions in graphene. *nature*, 438(7065):197–200, 2005.

[103] Yuanbo Zhang, Yan-Wen Tan, Horst L Stormer, and Philip Kim. Experimental observation of the quantum hall effect and berry's phase in graphene. *nature*, 438(7065):201–204, 2005.

[104] Xu Du, Ivan Skachko, Fabian Duerr, Adina Luican, and Eva Y Andrei. Fractional quantum hall effect and insulating phase of dirac electrons in graphene. *Nature*, 462(7270):192–195, 2009.

[105] Kostya S Novoselov, D Jiang, F Schedin, TJ Booth, VV Khotkevich, SV Morozov, and Andre K Geim. Two-dimensional atomic crystals. *Proceedings of the National Academy of Sciences*, 102(30):10451–10453, 2005.

[106] Ganesh R Bhimanapati, Zhong Lin, Vincent Meunier, Yeonwoong Jung, Judy Cha, Saptarshi Das, Di Xiao, Youngwoo Son, Michael S Strano, Valentino R Cooper, et al. Recent advances in two-dimensional materials beyond graphene. *ACS nano*, 9(12):11509–11539, 2015.

[107] Saptarshi Das, Joshua A Robinson, Madan Dubey, Humberto Terrones, and Mauricio Terrones. Beyond graphene: progress in novel two-dimensional materials and van der waals solids. *Annual Review of Materials Research*, 45:1–27, 2015.

[108] Chaoliang Tan, Xiehong Cao, Xue-Jun Wu, Qiyuan He, Jian Yang, Xiao Zhang, Junze Chen, Wei Zhao, Shikui Han, Gwang-Hyeon Nam, et al. Recent advances in ultrathin two-dimensional nanomaterials. *Chemical reviews*, 117(9):6225–6331, 2017.

[109] Yi-Lun Hong, Zhibo Liu, Lei Wang, Tianya Zhou, Wei Ma, Chuan Xu, Shun Feng, Long Chen, Mao-Lin Chen, Dong-Ming Sun, et al. Chemical vapor deposition of layered two-dimensional mosi2n4 materials. *Science*, 369(6504):670–674, 2020.

[110] Simone Bertolazzi, Jacopo Brivio, and Andras Kis. Stretching and breaking of ultrathin mos2. *ACS nano*, 5(12):9703–9709, 2011.

[111] Yongqing Cai, Gang Zhang, and Yong-Wei Zhang. Polarity-reversed robust carrier mobility in monolayer mos2 nanoribbons. *Journal of the American Chemical Society*, 136(17):6269–6275, 2014.

[112] M. P. L. Sancho, J.M. Lopez. Sancho, J. M. L. Sancho, and J. Rubio. Highly convergent schemes for the calculation of bulk and surface green functions. *J. Phys. F: Metal Physics*, 15(4):851–858, apr 1985.

[113] Jakub Płachta, Emma Grodzicka, Anna Kaleta, Sławomir Kret, Lech T. Baczewski, Aleksiej Pietruczik, Maciej Wiater, Mateusz Goryca, Tomasz Kazimierczuk, Piotr Kossacki, Grzegorz Karczewski, Tomasz Wojtowicz, and Piotr Wojnar. Magnetic field induced mixing of light hole excitonic states in (Cd,Mn)Te/(Cd,Mg)Te core/shell nanowires. *Nanotechnology*, 29(20):205205, mar 2018.

[114] Jan Hajer, Maximilian Kessel, Christoph Brüne, Martin P. Stehno, Hartmut Buhmann, and Laurens W. Molenkamp. Proximity-induced superconductivity in CdTe-HgTe core-shell nanowires. *Nano Lett.*, 19:4078–4082, 2019.

[115] C. Betthausen, P. Giudici, A. Iankilevitch, C. Preis, V. Kolkovsky, M. Wiater, G. Karczewski, B. A. Piot, J. Kunc, M. Potemski, T. Wojtowicz, and D. Weiss. Fractional quantum hall effect in a dilute magnetic semiconductor. *Phys. Rev. B*, 90:115302, Sep 2014.

[116] M. Kessel, J. Hajer, G. Karczewski, C. Schumacher, C. Brüne, H. Buhmann, and L. W. Molenkamp. Cdte-hgte core-shell nanowire growth controlled by rheed. *Phys. Rev. Materials*, 1:023401, Jul 2017.

[117] J. Hajer, W. Mantei, M. Kessel, C. Brüne, S. Wenner, A. T. J. van Helvoort, H. Buhmann, and L. W. Molenkamp. Selective area grown znte nanowires as the basis for quasi-one-

dimensional cdte-hgte multishell heterostructures. *Phys. Rev. Materials*, 4:066001, Jun 2020.

[118] K. M. Fijalkowski, N. Liu, M. Hartl, M. Winnerlein, P. Mandal, A. Coschizza, A. Fothergill, S. Grauer, S. Schreyeck, K. Brunner, M. Greiter, R. Thomale, C. Gould, and L. W. Molenkamp. Any axion insulator must be a bulk three-dimensional topological insulator. *Phys. Rev. B*, 103:235111, Jun 2021.